

Electronic Thesis and Dissertation Repository

12-13-2017 2:30 PM

Three Experiments on Complex Fluids

Yang Liu

The University of Western Ontario

Supervisor

John R de Bruyn

The University of Western Ontario

Graduate Program in Physics

A thesis submitted in partial fulfillment of the requirements for the degree in Doctor of Philosophy

© Yang Liu 2017

Follow this and additional works at: <https://ir.lib.uwo.ca/etd>



Part of the [Fluid Dynamics Commons](#)

Recommended Citation

Liu, Yang, "Three Experiments on Complex Fluids" (2017). *Electronic Thesis and Dissertation Repository*. 5118.

<https://ir.lib.uwo.ca/etd/5118>

This Dissertation/Thesis is brought to you for free and open access by Scholarship@Western. It has been accepted for inclusion in Electronic Thesis and Dissertation Repository by an authorized administrator of Scholarship@Western. For more information, please contact wlsadmin@uwo.ca.

Abstract

The behaviour of complex fluids is fundamentally interesting and important in many applications. This thesis reports on three experiments on the thermal and rheological behaviour of complex fluids. The first is a study of the rheological properties of and heat transport in a saline solution of hydroxyethyl cellulose. This material has been used as a tissue phantom in testing the behavior of medical devices in MRI scanners. We find it behaves as a typical entangled polymer, and flows in response to local heating, such as could occur due to eddy-current heating of metallic devices in an MR scanner. We use laboratory experiments and numerical simulations to determine the convective and conductive contributions to the heat transport in a simple model of this system. Our results indicate that convective heat transport is of the same order of magnitude as conductive transport under conditions typical of MRI device tests. The second project is an investigation of the start-up flow and yielding of a simple yield-stress fluid (Carbopol 940) in a vertical pipe. The Carbopol was displaced from below by an immiscible Newtonian liquid (Fluorinert FC-40) injected at a constant, controlled rate. Rough and smooth-walled pipes were used to study the effects of wall boundary conditions. In the rough-walled pipe, the yielding involved a long transient with several steps: elastic deformation, the onset of wall slip, yielding at the wall, and finally a steady-state plug flow that is well-described by the predictions of the Herschel-Bulkley model. In contrast, in the smooth-walled pipe, the wall shear stress never exceeded the yield stress. In the third project, we study the flow of Carbopol solutions confined to square microchannels with sides ranging from 500 down to 50 μm . In the larger channels, the measured velocity profiles agreed well with simulations based on the bulks-scale rheology of the Carbopol and the Herschel-Bulkley model. In contrast, in microchannels with sides less than 150 μm the velocity profiles could not be fitted by a model with a finite yield stress, but instead were described by a power-law model with zero yield stress. We explain the vanishing of the yield stress in terms of the confinement of the Car-

bopol's microstructure by the microchannels.

Keywords: Rheology, complex fluids, yielding, yield stress, confinement

Co-Authorship Statement

The work in chapter 3 has been published as: Yang Liu, Cameron C. Hopkins, William B. Handler, Blaine A. Chronik, John R. de Bruyn, Rheology and heat transport properties of a hydroxyethyl cellulose-based MRI tissue phantom, *Biomedical Physics & Engineering Express*, 3:045008, 2016. I did all the experiments and data analysis and wrote early drafts of this paper. Cameron C. Hopkins performed the numerical simulations. William B. Handler and Blaine A. Chronik provided the HEC solutions and the expertise on MRI applications. All the authors provided editorial comments on this paper. John R. de Bruyn supervised the project.

The work in chapter 4 has been submitted for publication: Yang Liu, John R. de Bruyn, Start-up flow of a yield-stress fluid in a vertical pipe, *Journal of Non-Newtonian Fluid Mechanics*. I did all the experiments, simulations, and data analysis and was the primary author of the paper. John R. de Bruyn supervised the project and provided editorial comments on the paper.

The work in chapter 5 will be submitted for publication to *Journal of Non-Newtonian Fluid Mechanics*. The authors include Yang Liu, Daniel Lorusso, David Holdworth, Tamie L. Poepping, John R. de Bruyn. I designed the experiment, made the microchannels, and did all the experiments, simulations, and data analysis, and was the primary author of the paper. Daniel Lorusso and David Holdworth provided instruction and assistance in fabricating the channels. Tamie L. Poepping provided equipment and expertise in the use of the channels and micro PIV. John R. de Bruyn supervised the project and provided editorial comments on the paper.

Acknowledgments

I am highly indebted to my supervisor, Dr. John R. de Bruyn, for advising me with much patience over the last five years. I learned how to do research the right way from John. None of my work would have been possible without his support.

Special thanks go to Dr. Blaine A. Chronik and Dr. Tamie L. Poepping for cooperation and collaboration in my research. Without their participation, I would not have finished this big work.

Thanks also go to the Natural Sciences and Engineering Research Council of Canada and the University of Western Ontario for funding this research. We are grateful to P. de Souza Mendes for helpful conversations and to Ranjith Divigalpitiya of 3M Canada for providing the Fluorinert.

My advisory committee, Dr. Richard A. Holt and Dr. Michael G. Cottam, provided helpful advice at regular intervals throughout the project, and for this I'm grateful.

Here at the Department of Physics I worked with a number of fellow graduate students. I wish to thank Cameron C. Hopkins who did some Comsol simulations for me and reviewed the first draft of the introductory chapter of this thesis, and Nirosh Getangama and Nayeob Gi who helped me to format this thesis using LATEX. Thanks also to former colleagues Grace Ge, Maryam Mozaffari, and Masha Goiko who all contributed in many ways.

Brian Dalrymple and Frank Van Sas manufactured parts of the apparatus used in my experiments. Tim Goldhawk and Todd Simpson assisted me in Nanofabrication Lab. Thanks also to Henry Leparskas for computer support.

I especially want to thank Clara Buma, Jodi Guthrie, Brian Davis, Shailesh Nene and Phin Perquin who always treated me with kindness.

Finally, I must give thanks to my family members, including my parents and other relatives, who contributed so much to my education, career, and growth. Without their efforts and support, I would not have reached this far.

Contents

Abstract	i
Co-Authorship Statement	iii
Acknowledgements	iv
List of Figures	ix
List of Tables	xvii
List of Symbols	xviii
List of Abbreviations	xix
1 Introduction	1
1.1 Complex Fluids	1
1.1.1 Viscoelasticity	3
1.2 Rheology of complex fluids	6
1.2.1 Shear thinning and shear thickening	7
1.2.2 Yield-stress fluids	8
1.2.3 Thixotropy	10
1.2.4 Yielding	14
1.2.5 Confinement effects	15
1.3 Summary of Present Work	16
1.3.1 Overview	16

1.3.2	Rheology and heat transport properties of a hydroxyethyl cellulose– based MRI tissue phantom	17
1.3.3	Start-up flow of a yield-stress fluid in a vertical pipe	17
1.3.4	Confinement effects on the rheology of Carbopol in microchannels	18
	Bibliography	19
2	Materials and methods	25
2.1	Introduction	25
2.2	Materials	25
2.2.1	Hydroxyethyl cellulose	25
2.2.2	Carbopol	27
2.3	Techniques	28
2.3.1	Shear Rheometry	28
2.3.2	Particle Image Velocimetry (PIV)	31
2.4	Apparatus	33
2.4.1	Apparatus for yielding experiments	34
2.4.2	NI LabVIEW	34
2.4.3	Fabrication of microfluidic devices	36
2.5	Ansys Fluent	37
	Bibliography	43
3	Rheology and heat transport properties of a HEC-based MRI tissue phantom	45
3.1	Introduction	45
3.2	Methods	47
3.2.1	Sample Preparation	47
3.2.2	Rheological Measurements	48
3.2.3	Heat transport and flow measurements	48
3.2.4	Numerical simulations	50

3.3	Results	51
3.3.1	Rheology	51
3.3.2	Thermal convection	55
3.4	Discussion and Conclusion	61
	Bibliography	64
4	Start-up flow of a yield-stress fluid in a vertical pipe	67
4.1	Introduction	67
4.2	Experiment	69
4.2.1	Fluid preparation	69
4.2.2	Rheological characterization	70
4.2.3	Experimental setup	71
4.3	Results	73
4.4	Numerical simulation	81
4.5	Discussion	84
4.6	Conclusion	87
4.7	Appendix	87
	Bibliography	90
5	Confinement effects on the rheology of Carbopol	96
5.1	Introduction	96
5.2	Experiment	98
5.2.1	Fabrication of microchannels	98
5.2.2	Fluid preparation and bulk rheology	100
5.2.3	Micro-particle image velocimetry	103
5.2.4	Computational fluid dynamics	104
5.3	Results	105
5.3.1	Water	105

5.3.2	HEC	107
5.3.3	Carbopol	108
5.4	Discussion and conclusion	111
	Bibliography	115
6	General Discussion and Conclusions	118
	Bibliography	123
	Curriculum Vitae	126

List of Figures

1.1	Diagram showing shear stress, strain, and shear rate in a layer of fluid between two horizontal plates. The upper plate moves with a velocity v , while the lower plate is fixed.	2
1.2	Left: Diagram of the Maxwell Model. The right graphs show the stress relaxation behaviour obtained by solving the model for $\dot{\gamma}(t > 0 \text{ s}) = 0 \text{ s}^{-1}$ and $\tau(t = 0 \text{ s}) = \tau_0 \text{ Pa}$. . .	4
1.3	Left: Diagram of the Kelvin–Voigt Model. The right graph shows the strain creeping behaviour obtained by solving the model for $\tau(t < 0 \text{ s}) = 0 \text{ Pa}$, $\tau(t \geq 0 \text{ s}) = \tau_0 \text{ Pa}$, and $\gamma(t = 0 \text{ s}) = 0$	5
1.4	Flow curves of different types of fluids.	6
1.5	Flow curves of a thixotropic fluid measured with increasing steps in the shear rate and then decreasing steps.	11
1.6	The flow curve solved for $m > 1$ using Eq. (1.8).	13
2.1	The chemical formula of Hydroxyethyl cellulose (HEC).	26
2.2	The chemical formula of polyacrylic acid.	28
2.3	The microstructure of Carbopol. The dashed circles represent the swollen polymer blobs.	29
2.4	A schematic diagram of the cone-and-plate measuring tool of the shear rheometer. Ω is the angular velocity of the rotating cone. θ_0 is the cone angle.	30
2.5	Two successive video frames used for PIV analysis. The bright points are small particles suspended in the experimental fluid and illuminated by a light source. The squares in the frames are interrogation windows.	32

2.6	The overall set-up of the experiments in Chap. 4.	35
2.7	Some components of the overall apparatus shown in Fig. 2.6.	35
2.8	Left: GPIB-USB-HS (IEEE 488) used to connect voltmeters to the computer. Right: PCI-1407 (IMAQ) hardware used to connect the camera to the computer.	37
2.9	The LabVIEW block diagram code controlling the camera in the experiments de- scribed in Chaps. 3 and 4.	38
2.10	The computational domain used to simulate a channel in Chap. 5.	40
2.11	The results of a simulation for water flowing in the channel shown in Fig. 2.10. Top: the computational mesh used in the simulations. Middle: the simulated velocity map at the outlet of the channel. Bottom: the simulated velocity profile on the mid-height line at the outlet of the channel.	41
2.12	The results of a simulation for Carbopol in the channel shown in Fig. 2.10. Top: the computational mesh used in the simulations. Middle: the simulated velocity map at the outlet of the channel. Bottom: the simulated velocity profile on the mid-height line at the outlet of the channel.	42
3.1	The experimental set-up used to measure convective heat transport in fluids. A tank contains the fluid of interest, which is seeded with small flow visual- ization particles. The tank is 30.5 ± 0.1 cm in length, 21.2 ± 0.1 cm in height, and 15.5 ± 0.1 cm in width into the page. A heater is mounted at the left-hand edge of the tank, and the temperature measured at four locations with optical temperature probes. The visualization particles are illuminated by a laser sheet coming in from the right-hand side of the diagram, and their motion is recorded by a video camera looking into the page. The dotted rectangle indicates the re- gion imaged by the camera. The origin of the x - y coordinate system shown is at the bottom left corner of the tank.	49

3.2	<p>(a) The shear stress σ as a function of shear rate $\dot{\gamma}$ of the HEC-saline solution at 25°C. The waiting time at each value of $\dot{\gamma}$ was 1 min. (b) Viscosity η obtained from the data plotted in (a). The dashed lines are fits to the Cross model, Eq. (3.2). The open circles are for fresh HEC, while the filled circles are for the aged solution. The inset shows the viscosity at a $\dot{\gamma} = 1 \text{ s}^{-1}$ measured with different values of the waiting time.</p>	52
3.3	<p>The zero-shear-rate viscosity η_0 for both fresh and aged HEC solutions plotted as a function of temperature. The open and filled circles are data for the fresh and aged HEC solutions, respectively. The dashed lines are fits to Eq. (3.3), as discussed in the text.</p>	52
3.4	<p>Elastic and viscous moduli of the fresh HEC-saline solution, scaled to a temperature of 25°C using time-temperature superposition. The different symbols indicate data recorded at different temperatures: \circ: 20°C, \square: 25°C, ∇: 30°C, \triangle: 40°C, \diamond: 60°C. Solid symbols are G'' and open symbols are G'. The dashed lines are power-law fits to the lowest-frequency data. The inset shows the frequency scaling factor α for fresh (open symbols) and aged (solid symbols) HEC-saline solution.</p>	54
3.5	<p>The velocity field measured in an experiment using water. The field of view is at the top left of the fluid, in a vertical plane through the center of the tank, as discussed in the text. The edge of the heater is at $x = 0$; the bottom of the tank is at $y = 0$, and the free surface of the fluid is at the top of the image. The tip of temperature probe 1 is close to the heater, and the dotted line shows the approximate position of temperature probe 2. The temperature difference between these two probes was 4.2 K. The length of the scale bar at the top left corresponds to a velocity of 0.05 cm/s.</p>	55

3.6	<p>The velocity field in experiments on the HEC solution. (a) shows the velocity field when the temperature difference between probes 1 and 2 was 10.8 K; (b) is for a temperature difference of 49 K. The field of view is at the top left of the fluid, in a vertical plane through the center of the tank, as discussed in the text. The edge of the heater is at $x = 0$; the bottom of the tank is at $y = 0$, and the free surface of the fluid is at the top of the image. The tip of temperature probe 1 is close to the heater, and the dotted line shows the approximate position of temperature probe 2. The length of the scale bar at the top right of (a) corresponds to a velocity of 3×10^{-3} cm/s.</p>	58
3.7	<p>Simulations of the flow and temperature fields for the three experiments described in the text. (a)-(c): Water, $T_1 = 295.9$ K; (d)-(f): HEC solution, $T_1 = 304.7$ K, (g)-(i): HEC solution, $T_1 = 352.8$ K. The left-hand column shows the velocity field in the entire simulated domain, which models the tank used in the experiments. The center column shows the velocity field in the upper left corner of the domain. This corresponds to the region in which the velocity was measured experimentally, as shown in Figs. 3.5 and 3.6. The right-hand column shows the temperatures measured at the four probes as solid circles, and the simulated temperature at approximately the same depth as a dashed line.</p>	59
4.1	<p>The shear stress τ as a function of shear rate $\dot{\gamma}$ of 0.13 wt% Carbopol containing 0.6 vol% glass beads. Symbols are the measured data, and the dashed line is a fit to the Herschel-Bulkley model, as described in the text.</p>	70
4.2	<p>A schematic diagram of the experimental apparatus. P_1 and P_2 are pressure gauges. The solid horizontal line near the bottom of the pipe is the interface between the Carbopol and Fluorinert. The area between the dotted lines is the region used for flow visualization.</p>	72

4.3	Data from an experiment using 0.18 wt% Carbopol in the rough-walled pipe with a very slow displacement rate, $Q_l = 5.02 \times 10^{-8} \text{ m}^3/\text{s}$. (a) P_1 , the pressure in the Carbopol. The dashed lines are linear fits to $P_1(t)$ at early (160-200 s) and late times (300-400 s). The time at which the two fits intersect is t^* . (b) τ_w , the wall shear stress, calculated from Eq. (4.1). The black circle is τ_w^* , the wall shear stress at t^* . The dashed line is the yield stress measured with the rheometer. The three time intervals discussed in the text and in Fig. 4.4 are shown by the grey rectangles. The uncertainty of τ_w is approximately the size of the symbols.	74
4.4	The flow velocity $v(r)$ corrected for the slip velocity v_s for the same experiment as in Fig. 4.3. The r axis spans the full diameter of the pipe. The dashed line is the steady-state velocity profile predicted by the HB model.	75
4.5	Additional results for the experiment shown in Fig. 4.3. (a) Q , the volumetric flow rate. (b) $ \dot{\gamma}_w $, the absolute value of the wall shear rate. (c) v_s , the slip velocity.	75
4.6	Data from an experiment using 0.18 wt% Carbopol in the rough-walled pipe with a displacement rate of $Q_l = 3.41 \times 10^{-7} \text{ m}^3/\text{s}$. (a) τ_w , the wall shear stress. The dark circle is τ_w^* , and the dashed line is the yield stress. The rectangles indicate the three time intervals referred to in Fig. 4.7. The uncertainty of τ_w is approximately the size of the symbols. (b) v_s , the slip velocity. (c) $ \dot{\gamma}_w $, the absolute value of the wall shear rate.	76
4.7	Velocity profiles for the same experiment as in Fig. 4.6. The dashed line is the velocity profile predicted by the HB model.	77
4.8	Results of two experiments with 0.18 wt% Carbopol in the smooth-walled pipe. (a), (b), and (c) are from an experiment with a low displacement rate, $Q_l = 5.02 \times 10^{-8} \text{ m}^3/\text{s}$. (a) τ_w , the wall shear stress. The black circle is τ_w^* . The two time intervals discussed in the text are shown by rectangles. (b) v_s , the slip velocity. (c) $ \dot{\gamma}_w $, the absolute value of the wall shear rate. (d), (e), and (f) are the corresponding plots for an experiment with $Q_l = 5.49 \times 10^{-7} \text{ m}^3/\text{s}$	78

4.9	Velocity profiles, corrected for slip, for the two experiments shown in Fig. 4.8. (a) $Q_l = 5.02 \times 10^{-8} \text{ m}^3/\text{s}$. (b) $Q_l = 5.49 \times 10^{-7} \text{ m}^3/\text{s}$	79
4.10	τ_w^* as a function of the displacement rate Q_l for three concentrations of Carbopol in both rough and smooth pipes. Solid diamonds: rough-walled pipe. Open circles: smooth-walled pipe. The horizontal dashed lines are the yield stress measured with the rheometer. When error bars are not shown, the uncertainties are approximately the size of the symbols.	80
4.11	Wall shear stress τ_w (black dots and line) and slip velocity v_s (grey dots and line) as a function of time for (a) 0.13 wt% Carbopol in the rough-walled pipe and (b) 0.18 wt% Carbopol in the smooth-walled pipe.	81
4.12	Results from a simulation of a slow displacement. (a) The imposed wall shear stress τ_w (black dots) and its time derivative $\dot{\tau}_w$ (grey dots) as a function of time. The dashed line is the yield stress. (b) $\lambda_w(t)$, the structure parameter at the wall of the pipe. (c) $ \dot{\gamma}_w (t)$, the absolute value of the wall shear rate. The symbols indicate the times corresponding to the velocity profiles plotted in Fig. 4.13	82
4.13	Simulated velocity profiles for a slow displacement. The symbols correspond to the times indicated in Fig. 4.12.	83
4.14	Results from a simulation of a fast displacement. (a) The imposed wall shear stress τ_w (black dots) and its time derivative $\dot{\tau}_w$ (grey dots) as a function of time. The dashed line is the yield stress. (b) $\lambda_w(t)$, the structure parameter at the wall of the pipe. (c) $ \dot{\gamma}_w (t)$, the absolute value of the wall shear rate. The symbols indicate the times corresponding to the velocity profiles plotted in Fig. 4.15.	83
4.15	Simulated velocity profiles for a fast displacement. The symbols correspond to the times indicated in Fig. 4.14.	84

5.1	(a) The Plexiglas mold used to form the microchannels. The diameter of the mold is 1.7 cm. (b) The PDMS cast using the mold shown in (a) is bonded to the bottom plate, and polyethylene tubes are inserted into the inlet and outlet reservoirs to form the full microchannel assembly.	99
5.2	A micrograph of the cross-section of the top PDMS piece of Channel 4. The scale bar is 10 μm in length.	101
5.3	The viscosity as a function of shear rate for a 3.4 wt% HEC solution seeded with tracer particles. The dashed line is a fit of the Cross model to the data.	102
5.4	The shear stress as a function of shear rate for a 0.14 wt% Carbopol 940 solution seeded with tracer particles. The dashed line is a fit of the Herschel-Bulkley model to the data.	103
5.5	A schematic diagram of the experimental setup. The fluid was pumped into the microchannel at a constant rate from a syringe driven by a syringe pump. A camera connected to the microscope imaged the motion of fluorescent tracer particles suspended in the fluid.	104
5.6	The velocity profiles in water at the mid-plane of Channels 1 and 5. The velocities have been corrected for the slip velocity measured at the channel walls. x is the horizontal position along the width of the channel. Circles: experimental measurements. Lines: simulations. (a) Channel 1, $Q_{in} = 23 \mu\text{l/hr}$. (b) Channel 5, $Q_{in} = 0.4 \mu\text{l/hr}$	106
5.7	The velocity profiles in the HEC solution at the mid-plane of Channels 1 and 5. The velocities have been corrected for the slip velocity measured at the channel walls. Circles: experimental measurements. Lines: simulations. (a) Channel 1, $Q_{in} = 42 \mu\text{l/hr}$. (b) Channel 5, $Q_{in} = 0.4 \mu\text{l/hr}$	107

5.8 The velocity profiles in Carbopol at the mid-plane of Channels 1, 3, 5. The velocities have been corrected for the slip velocity measured at the channel walls. Symbols: experimental measurements. Solid lines: simulations using the HB model with the measured yield stress. Dashed lines: fits of the data to a power-law model, with zero yield stress. (a) Channel 1. Circles: $Q_{in} = 55 \mu\text{l/hr}$. Squares: $Q_{in} = 70 \mu\text{l/hr}$. (b) Channel 3. Circles: $Q_{in} = 6 \mu\text{l/hr}$. Squares: $Q_{in} = 10 \mu\text{l/hr}$. (c) Channel 5. Circles: $Q_{in} = 0.3 \mu\text{l/hr}$; for this data set the uncertainty in $v - v_s$ is approximately the size of the symbols. Squares: $Q_{in} = 1.4 \mu\text{l/hr}$ 109

5.9 v_s/v_{max} , the ratio of the slip velocity to the maximum velocity at the mid-plane of the channel plotted as a function of the width of the channel. Filled circles: Carbopol. Unfilled circles: water. Unfilled squares: HEC. The uncertainties for the data without errorbars shown are approximately the size of the symbols. 110

List of Tables

3.1	Comparison of simulated and experimentally determined heat transport.	61
4.1	Yield stress and Herschel-Bulkley model parameters for the Carbopol gels containing glass beads used in this work.	71
5.1	Dimensions of the microchannels	100
5.2	Parameters of the power-law model used to fit velocity profiles in the smaller channels.	110

List of Symbols

τ	shear stress
G	elastic constant
γ	strain
$\dot{\gamma}$	shear rate
η	viscosity
t	time
τ_y	yield stress
M	torque
Ω	angular velocity
ω	angular frequency
G''	viscous modulus
G'	elastic modulus
D	thermal conductivity
T	temperature
ρ	density
C	heat capacity
j	heat flux
c	concentration
g	gravitational acceleration
Q	flow rate
P	pressure

List of Abbreviations

HB	Herschel-Bulkley
HEC	Hydroxyethyl cellulose
MRI	Magnetic resonance imaging
PDMS	Polydimethylsiloxane

Chapter 1

Introduction

1.1 Complex Fluids

Imagine a layer of fluid contained between two plates, as shown in Fig. 1.1. The top plate moves to the right with velocity v , while the bottom plate is stationary. The fluid adheres to both plates so that it moves at the same velocity as the boundaries, known as the no-slip boundary condition. The shear stress is the resulting drag force imposed by the fluid on the plate per unit area. The strain, the deformation of the fluid, is the ratio of the displacement of the fluid to the height of the layer. The strain rate, also called the shear rate, is the first derivative of the strain with respect to time. The viscosity is the ratio of the shear stress to the shear rate.

Simple liquids, like water and alcohol, flow in response to any applied stress, and are Newtonian, meaning that at a fixed temperature, their viscosities are independent of shear stress, shear rate, or flow history. Solids, like copper, respond elastically to a small applied force and fracture for a large force. Complex fluids have both fluid-like and solid-like features to their behaviour, and so are viscoelastic [1]. They are non-Newtonian, meaning that the viscosity depends on the shear stress or the shear rate. For example, concentrated emulsions, which consist of small droplets of one phase dispersed in the other, show solid behaviour at small stresses but flow like a liquid at higher stresses. An everyday-life example of an

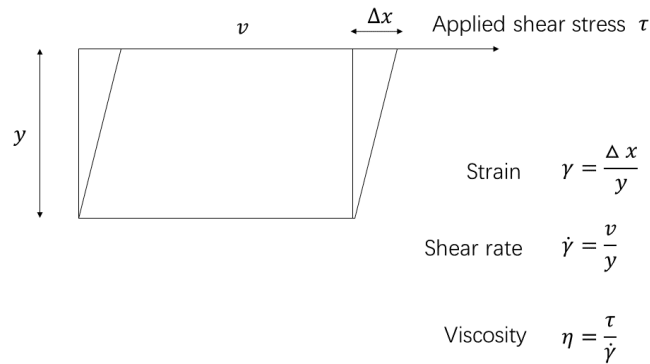


Figure 1.1: Diagram showing shear stress, strain, and shear rate in a layer of fluid between two horizontal plates. The upper plate moves with a velocity v , while the lower plate is fixed.

emulsion is mayonnaise. The microstructure of the material that results from the presence of the droplets, the interactions between the droplets, and the interfacial tension between the two phases give emulsions their interesting properties. In general, the viscoelastic behavior of complex fluids arises because the molecules making up the material assemble into larger structures with length scales that are dramatically bigger than the individual molecules [2]. In most cases, the structure is on the micron-scale. Many materials encountered in day-to-day life and in industry are complex fluids, including shaving cream, chocolate paste, molten polymers, battery slurry, hair gel, and biological fluids including mucus and blood. The dynamics of complex fluids can be highly nonlinear. When a strain or a stress is imposed on a complex fluid, the microstructure evolves over time, leading to complex dynamics on many time scales [3]. These are caused by the rearrangement of the microstructure in response to the imposed shear.

Complex fluids can have a range of complex rheological behaviour, depending on the details of the material. They can be shear-thinning, for which the viscosity decreases when the shear rate increases. For example, blood is a shear-thinning fluid. They can be shear-thickening, for which the viscosity increases when the shear rate increases. A well-known

shear-thickening fluid is a suspension of corn starch in water. Some materials undergo a transition from solid-like to fluid-like behaviour as the applied stress is increased. An example in everyday life is hair gel. Many complex fluids have properties that depend on time and on shear history, like waxy crude oil. Many of these properties are discussed in more detail in the following sections.

1.1.1 Viscoelasticity

As mentioned above, complex fluids exhibit characteristics of both elastic solids and viscous liquids. This is called viscoelasticity. The elasticity alone describes the ability of the material to deform reversibly in response to an applied force. For small forces or strains, Hooke's Law applies, and the shear stress is linearly proportional to strain:

$$\tau = G\gamma. \quad (1.1)$$

Here τ is the shear stress, G is the elastic constant, and γ is the strain. Viscous liquids flow irreversibly in response to a shearing force, and Newton's law of viscosity relates the shear stress to the shear rate:

$$\tau = \eta\dot{\gamma}. \quad (1.2)$$

Here η is the viscosity, which describes the resistance to flow. Molecules in the liquid carry momentum, and the viscosity characterizes the diffusion of this momentum [4].

The elastic and viscous behaviour of a fluid can be represented by an elastic spring and a viscous dashpot, respectively. Analogous to electric circuits, the spring and the dashpot can be connected in two ways: in series, which is known as the Maxwell model and is shown in Fig. 1.2, or in parallel, known as the Kelvin-Voigt model, shown in Fig. 1.3. When the spring and dashpot are connected in series, the stress on both elements is the same, while the strain is the sum of the strains across each of the two components, so the strain rate in this configuration is

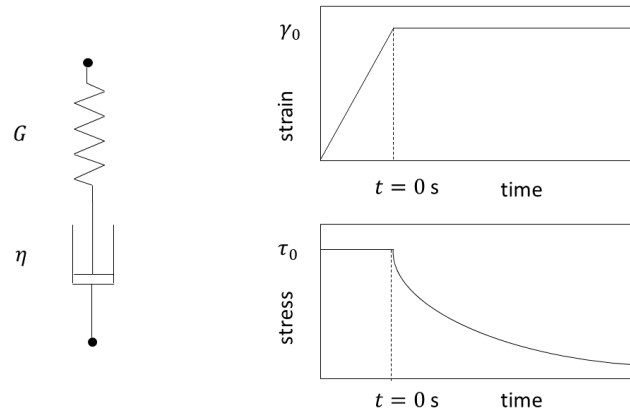


Figure 1.2: Left: Diagram of the Maxwell Model. The right graphs show the stress relaxation behaviour obtained by solving the model for $\dot{\gamma}(t > 0 \text{ s}) = 0 \text{ s}^{-1}$ and $\tau(t = 0 \text{ s}) = \tau_0 \text{ Pa}$.

given by $\dot{\gamma} = \dot{\gamma}_{dashpot} + \dot{\gamma}_{spring}$. Using Eqs. (1.1) and (1.2), we find for this model that

$$\dot{\gamma} = \frac{\tau}{\eta} + \frac{1}{G} \frac{d\tau}{dt}. \quad (1.3)$$

This is a first order differential equation for τ , and solving it gives a stress that is a function of time. The right-hand side of Fig. 1.2 illustrates schematically the behaviour of the stress that results from applying a certain strain rate for a long time for $t < 0 \text{ s}$, so that the material is in a steady state with some non-zero stress τ_0 , then suddenly changing the strain rate to zero at $t = 0 \text{ s}$, leading to a constant value of the strain γ_0 for $t \geq 0 \text{ s}$. The solution of Eq. (1.3) for the shear stress is

$$\tau = \tau_0 e^{-\frac{t}{\lambda}}. \quad (1.4)$$

Here, $\lambda = \frac{\eta}{G}$ is the relaxation time. The Maxwell model says when a constant strain is imposed on the material, the stress relaxes experimentally to zero, as shown in the right-hand side graph in Fig. 1.2. Experimentally, this is called a stress relaxation test. The physical picture corresponding to this process is as follows: initially both the spring and the dashpot are stretched. When the strain is fixed, the dashpot dissipates the energy stored in the spring, transferring

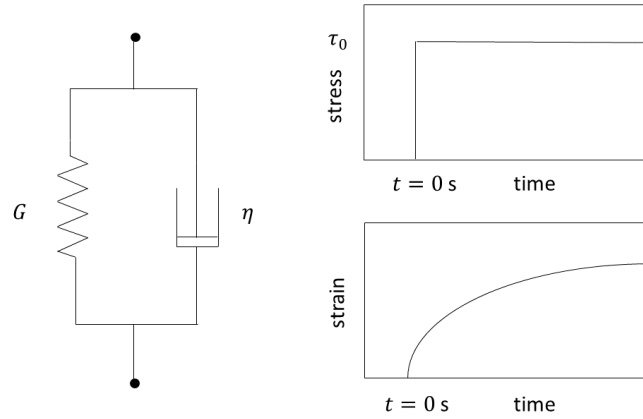


Figure 1.3: Left: Diagram of the Kelvin–Voigt Model. The right graph shows the strain creeping behaviour obtained by solving the model for $\tau(t < 0 \text{ s}) = 0 \text{ Pa}$, $\tau(t \geq 0 \text{ s}) = \tau_0 \text{ Pa}$, and $\gamma(t = 0 \text{ s}) = 0$.

deformation from the spring to the dashpot, and leading to the stress exponentially decaying to zero. In this process, the total strain is held constant. As the spring relaxes, the strain in the spring decreases, but the strain in the dashpot increases.

In the Kelvin-Voigt model, the strain on both components is the same and the total stress in the system is the sum of the stress on the two components:

$$\tau = G\gamma + \eta \frac{d\gamma}{dt}. \quad (1.5)$$

Solving this equation for $\gamma(t)$ for a constant stress τ_0 applied suddenly at $t = 0 \text{ s}$, and assuming $\gamma(t = 0 \text{ s}) = 0$, the solution for the strain is

$$\gamma = \frac{\tau_0}{G}(1 - e^{-\frac{t}{\lambda}}). \quad (1.6)$$

We find that the strain in the material increases over time, exponentially approaching a limiting value, as shown in the right-hand side graph in Fig. 1.3. Experimentally, this is called a creep test. During this test, initially the stress on the spring is zero since the deformation is zero. All of the stress is initially on the dashpot, which causes the dashpot to deform. Since the strains on

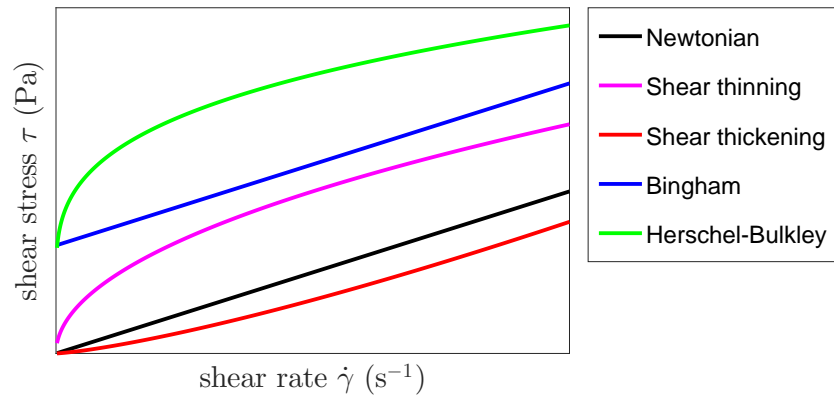


Figure 1.4: Flow curves of different types of fluids.

both components are the same, the spring has to deform as well. Thus the stress on the spring, and the strain, build up over time. Since the total stress is being held fixed in this process, the stress on the dashpot decreases.

Many more complex models involving additional components have been developed to describe more complex behaviour. These include the standard linear solid model [5] and the generalized Maxwell model that consists of many Maxwell components connected in series [6].

1.2 Rheology of complex fluids

Rheology is the study of the flow or deformation of materials. A common rheological experiment involves measuring the a material's flow curve, i.e., the shear stress as a function of shear rate. Fig. 1.4 shows schematically the shear stress as a function of the shear rate for different types of fluids. The flow curve of a Newtonian fluid is the black straight line passing through the origin. The viscosity of Newtonian fluids is independent of shear rate or

shear stress at a fixed temperature and pressure. Molecular liquids and dilute solutions of low molecular weight polymers are typically Newtonian. Perhaps the most common deviation from Newtonian behaviour is shear-thinning behaviour, by which the viscosity of the fluid decreases with increasing shear rate. Many polymer solutions or melts exhibit shear-thinning behaviour. This is depicted in Fig. 1.4 by the purple curve with decreasing slope. Shear-thickening, by which the viscosity of the fluid increases with increasing shear rate, is depicted in Fig. 1.4 by the red curve with increasing slope. Concentrated particle suspensions, such as corn starch in water, show shear-thickening [7]. The blue straight line with a non-zero intercept on the stress axis represents what is known as a Bingham fluid. The intercept means that the material does not flow for applied stresses below this threshold, which is called the yield stress. The green curve with an intercept and with a changing slope is a Herschel-Bulkley fluid. It also has a yield-stress, but with a slope which is dependent on shear rate.

1.2.1 Shear thinning and shear thickening

The basic mechanism behind shear-thinning is that the shear changes the structure of the material to allow it to flow more easily. It can often be explained by changes of the microstructure in response to shear. In shear-thinning polymer solutions, the microstructure consists of entanglements of the polymer chains. In blood, it is due to aggregates of red blood cells. When there is no shear, the polymer molecules in a polymer solution are entangled coils. When the shear rate increases, the polymer molecules become stretched out by the shear. It is easier for the stretched out molecules to slide past each other than it is for the coils, so the entanglements are more easily released under shear [8]. In blood, the aggregates break down to single cells under shear, causing shear thinning [9]. Suspensions of rod-like particles are also shear thinning [10]. At rest, the rods are randomly oriented and have a large resistance to flow and thus a high viscosity. Under high shear, the rods tend to align along the flow direction, making flow easier and decreasing the viscosity.

Shear-thickening behavior is observed in concentrated colloidal suspensions or systems

with rough particles [11]. It only happens when the volume fraction is high enough that the particles jam [12]. The earliest observation of shear-thickening came from the paper industry. It was found that the viscosity of paper coatings increased when the paper moved at high speed [13]. In suspensions of uncharged particles such as corn starch in water, shear-thickening occurs when the particles jam together. As a consequence, particle motion becomes arrested and the particles interact through friction forces, increasing the flow resistance of the fluid. Shear thickening can also arise due to other causes. In some concentrated colloidal suspensions, strong hydrodynamic interactions between particles at high shear rates can induce fluctuations in particle density, leading to the formation of chains of particles known as hydroclusters [13] that preferentially align at 45° and 135° relative to the shear direction [14, 15]. This shear-induced structure makes it more difficult for particles to pass each other, leading to higher energy dissipation and an increased viscosity.

1.2.2 Yield-stress fluids

Two of the fluid models shown in Fig. 1.4 have non-zero intercepts on the shear stress axis. For these types of fluids, if the applied stress is smaller than a threshold yield stress, they do not flow and instead exhibit elastic-solid behaviour. When the applied stress is above the yield stress they flow like a liquid. These fluids are referred to as yield-stress fluids. The blue flow curve displaying a constant slope represents the Bingham model:

$$\begin{cases} \tau = \tau_y + k\dot{\gamma} & \tau > \tau_y; \\ \dot{\gamma} = 0 & \tau \leq \tau_y. \end{cases}$$

Here, τ_y is the yield stress and k is the plastic viscosity. The green flow curve with a yield stress and a changing slope is a representation of a Herschel-Bulkley (HB) model:

$$\begin{cases} \tau = \tau_y + k\dot{\gamma}^n & \tau > \tau_y; \\ \dot{\gamma} = 0 & \tau \leq \tau_y. \end{cases}$$

n is a power index, which is taken to be smaller than one. These two models describe simple, non-thixotropic yield-stress fluids, for which the viscosity and the yield stress are time-independent. Examples of simple yield-stress fluids are some Carbopol solutions, foams, and concentrated emulsions [16]. Even for simple yield-stress fluids, however, there has been a debate over the last three decades as to whether the material truly changes from a solid to a liquid when the yield stress is exceeded, or if the transition is instead from a highly viscous liquid to a less viscous liquid. Barnes and Walters (1985) measured the viscosity of yield stress materials using a stress-controlled rheometer; their results showed a high plateau viscosity at low shear stresses and a decreasing viscosity at higher stresses [17]. Barnes and collaborators also reported the similar phenomenon in [18, 19]. They argued that their results indicated that there was no true yield stress, but rather that the low-stress state was a Newtonian fluid with a very high viscosity. A similar phenomenon was observed in iron-oxide suspensions [20] and kaolin dispersions [21]. More recent experiments by Møller et al. (2009) demonstrated that the plateau viscosity at low shear stresses is a transient effect resulting from long relaxation times in the materials close to the yield stress [22]. They observed that the plateau viscosity at low shear stresses increased as the equilibration time at each value of the stress increased. They also showed that the viscosity increased with time for as long as 10^4 s when a small constant shear stress was applied. This work clearly demonstrated that the earlier measurements of Barnes and others were not performed in a steady state, and provided strong evidence for a true yield stress.

The yield stress is difficult to measure, and different results are obtained using different measuring methods [23]. One method is to determine the yield stress from the stress overshoot

measured when a constant shear rate is applied to a material initially at rest [24]. However, the value of the stress overshoot strongly depends on the applied shear rate, and the overshoot is not detected at high shear rates [25]. Another method of determining the yield stress is measuring the shear stress as a function of the shear rate by either increasing or decreasing the shear rate in steps, and fitting the data to either a Bingham model or a HB model. However, in measurements performed by applying increasing steps in the shear rate, the fluid undergoes a transition from a solid to a liquid during the first step. Elasticity plays an important role in this process and the sample requires a long time to get to the steady state. Measuring a flow curve by applying decreasing steps in the shear rate from high to low values avoids the long waiting time needed to reach equilibrium and any effects of viscoelasticity [26].

1.2.3 Thixotropy

It is often reported that the measured yield stress can be very different depending on the measuring time [27, 28]. Sometimes, this is simply because the sample has not reached steady state when the data are collected [22]. A more fundamental explanation is that the material's rheological properties, such as viscosity and yield stress, vary significantly with time. Fluids that behave in this way are referred to as thixotropic, and include, for example, attractive glasses [29], adhesive emulsions [30], granular systems [31], pastes [32], and yogurt [33]. In thixotropic fluids, the rate at which the microstructure recovers after being disrupted by shear is slower than the rate of the shear itself. This implies that there is an equilibration time over which the fluid properties adjust following a change in shear rate. In a thixotropic material, the viscosity decreases with time in an induced flow, and increases when the fluid comes to rest [34]. The viscosity of a thixotropic fluid is determined by a competition between the formation and destruction of structure in the fluid. Fig. 1.5 shows the flow curves of a thixotropic fluid, measured first by increasing the shear rate in steps, and then by decreasing it in steps. There is a hysteresis between the two curves and the decreasing branch indicates a lower viscosity than the increasing branch, since the structure of the fluid has been destroyed during the prior

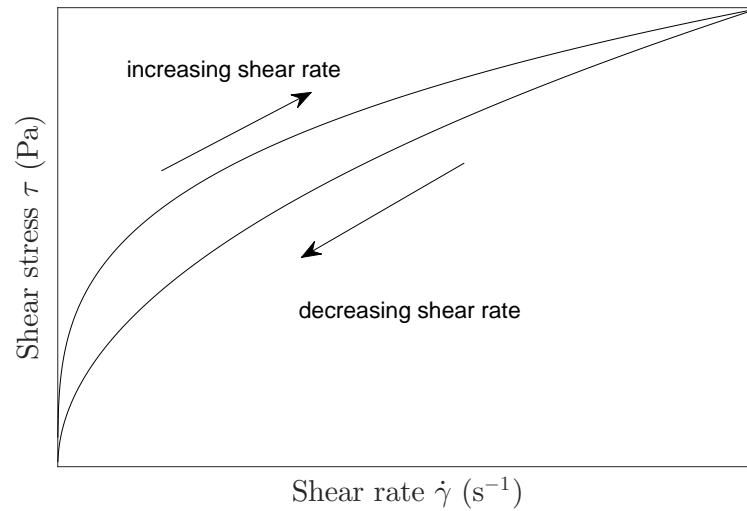


Figure 1.5: Flow curves of a thixotropic fluid measured with increasing steps in the shear rate and then decreasing steps.

increase of the shear. The structural breakdown in thixotropic fluids can show avalanche behavior, as observed by Coussot et al. [35]. They studied bentonite clay suspensions placed on an inclined plate. They found that at a fixed slope angle above a critical value, the sample began to flow and accelerated, indicating that the viscosity decreased at a constant stress due to the breakdown of the microstructure. In contrast, for a slope smaller than the critical value, they observed that the sample initially started flowing, then stopped completely [36]. This revealed that at small enough stresses, the viscosity increased with time at a constant stress. This is a consequence of the domination of structural build-up over break-up at small stresses. This phenomenon is called viscosity bifurcation [36]. The increase of viscosity with time is also called aging, while the decrease of viscosity at high shear rates is also called shear rejuvenation [29].

Thixotropy can be modeled in terms of the evolution of a structure parameter λ that represents the degree of structure in the material. Typically, a large value of λ indicates a highly

structured state [37, 38]. One such model is given by

$$\begin{aligned}\frac{d\lambda}{dt} &= \frac{1}{\theta} - k\lambda\dot{\gamma}, \\ \eta &= \eta_0(1 + \beta\lambda^m)\end{aligned}\tag{1.7}$$

[26, 29]. In this model, θ is the characteristic time to reform the structure, taken to be constant. k , β , and m are constant parameters of the model. η_0 is the constant viscosity at the limit of the fully unstructured state when $\lambda = 0$. The second term in the expression for $\frac{d\lambda}{dt}$ represents the rate of structural breakage, determined by the shear rate. The variation of λ with time depends on the competition between structural breakdown and reformation. By solving this model for $\frac{d\lambda}{dt} = 0$, we get the steady state value of the structure parameter, $\lambda_{eq} = \frac{1}{k\theta\dot{\gamma}}$. Inserting this into the equation for the viscosity and using the fact that $\tau = \eta\dot{\gamma}$, we find the steady state shear stress to be

$$\tau_{eq} = \frac{\eta_0\beta}{(k\theta)^m\dot{\gamma}^{m-1}} + \eta_0\dot{\gamma}.\tag{1.8}$$

The stress for $m > 1$ is shown as a function of shear rate in Fig. 1.6. The shear stress has a minimum at a critical shear rate $\dot{\gamma}_c$, and there is a region where the shear stress decreases as the shear rate increases. This part of the flow curve is unsteady, and if imposed shear rate is smaller than $\dot{\gamma}_c$, shear banding is observed [39, 26], as discussed below.

In thixotropic yield-stress fluids, shear localization that results in a heterogeneous flow field is often observed when a low shear rate is imposed. According to the Bingham or HB models, any nonzero shear rates should be observable for an appropriately chosen stress that is larger than the yield stress. In thixotropic fluids such as concentrated suspensions and emulsions, however, shear banding, which is the coexistence of an unsheared region and a region of sheared material, is observed [40, 32]. Interestingly, the shear rate in the sheared band is always equal to the critical shear rate $\dot{\gamma}_c$ [36]. This shear banding is predicted by the flow curve shown in Fig. 1.6. The regime where stress decreases as shear rate increases is not stable and cannot be measured experimentally [41, 42]. As a result, shear banding occurs when the

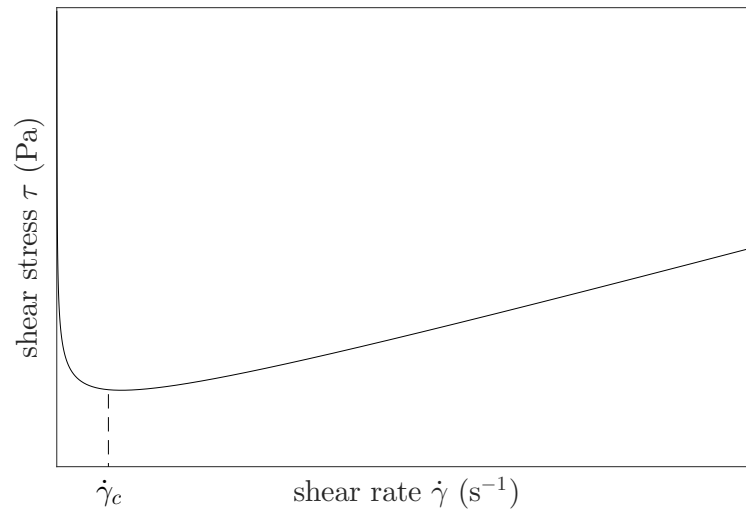


Figure 1.6: The flow curve solved for $m > 1$ using Eq. (1.8).

globally imposed shear rate is smaller than $\dot{\gamma}_c$. Only shear rates larger than $\dot{\gamma}_c$ or, equivalently, viscosities smaller than a critical value can be observed in thixotropic fluids. This behavior is in agreement with the viscosity bifurcation mentioned above.

Waxy crude oil is a thixotropic fluid and shows strong temperature-dependence. At temperatures below a value called the pour point, it has a crystalline structure consisting of wax particles which form a gel-like network structure, giving the oil a yield stress [43]. At high temperatures, the wax melts and the crude oil behaves like a Newtonian fluid [44]. Below the pour point, the fluid is thixotropic and its yield stress and viscosity strongly depend on shear history and cooling rate since the waxy crystalline structure takes a relatively long time to reform or break up [45, 46]. A problem of importance to engineers in oil fields is the restart of waxy crude oil in pipelines after a period of shutdown [47]. Flow can be restarted by displacing the gelled oil by a warm Newtonian oil pumped into the pipe under a constant pressure. In the absence of thixotropy and compressibility, the minimum pressure drop across the entire length of the pipe required to restart the oil would be $\Delta P = \frac{2\tau_y L}{R}$, where τ_y is the yield stress,

and L and R are the length and the radius of the pipe, respectively. In reality, since waxy crude oil is compressible and thixotropic, a smaller pressure drop can also activate oil transportation [48, 49, 50]. There is very little experimental work on the start-up flow of waxy crude oil, mainly because of the difficulties brought by the thixotropy and compressibility. In Chap. 4 we model this problem in a study of the start-up flow of Carbopol solutions, which are simple yield-stress fluids with very weak thixotropy and compressibility.

1.2.4 Yielding

The Bingham and Herschel-Bulkley models say that the yield-stress fluid changes from a solid to a liquid suddenly when the yield stress is exceeded. Physically, however, this yielding or fluidization transition does not occur instantaneously, but is a very complex and dynamic process. Putz et al. measured the stress-controlled flow curves of Carbopol solutions on a shear rheometer and observed three regimes: an elastic solid regime at low stress, in which the shear rate remained constant with increasing shear stress; a viscous liquid regime characterized by the Herschel-Bulkley model at high stress; and a regime in between that showed flow behavior somewhere between elastic and viscous [51]. Divoux et al. studied the yielding of Carbopol with a constant applied shear rate in the Couette geometry and observed that before steady homogeneous flow developed, the shear was localized close to the rotor. The fluidization of the material was observed to be a transient process and took a certain amount of time, depending on the applied shear rate. This fluidization time, t_f , was governed by a power-law function of the applied shear rate $t_f(\dot{\gamma}) \sim \frac{A}{\dot{\gamma}^\alpha}$ [52, 53]. They observed that for small applied shear rates this shear banding remained stationary for hours before the system suddenly became fully fluidized. Divoux et al. also studied the yielding of Carbopol under controlled-stress conditions, by applying a constant shear stress larger than the yield stress [54]. They observed that the yielding process in this case involved several steps: creep deformation, wall slip, shear banding, and finally homogeneous flow. The fluidization time was again a power-law function of the applied stress: $t_f(\tau) \sim \frac{B}{(\tau - \tau_y)^\beta}$. Combining the results from these two experiments, Divoux et al. were

able to derive the HB relation, $\tau = \tau_y + \tilde{\eta}\dot{\gamma}^n$, with $\tilde{\eta} = (\frac{B}{\lambda A})^{\frac{1}{n}}$, and $n = \frac{\alpha}{\beta}$ [54]. The expression for the power-law index n was in agreement with their experimental results. Divoux's experiments demonstrated that shear banding occurs in Carbopol when it yields, even though it is a simple yield-stress fluid with little or no thixotropy. Gibaud et al. studied the yielding of an attractive colloidal gel by applying a constant shear stress in the Couette geometry [55]. They observed that fluidization initially started at the rotor and gradually propagated throughout the whole sample, with a fluidization time that decreased exponentially as a function of the applied shear stress: $t_f \sim \exp(\frac{-\tau}{\tau_0})$, where τ_0 is a constant. This expression for t_f follows a Kramers-type law $t_f \sim \exp(\frac{E(\tau)}{k_B T})$, where $E(\tau) = -\tau v$ is the energy barrier and $v = \frac{k_B T}{\tau_0}$. The importance of this work is to relate yielding to overcoming of an energy barrier [55]. Rajaram et al. used a fast scanning confocal microscope to image the microstructural evolution of a dilute colloidal gel while it was yielding in the cone-and-plate geometry, with a constant applied shear rate [56]. They observed three stages of microstructural change: an initial small movement of particles along the flow direction, the final disconnected clusters, and an intermediate structure between these two. This work relates the yielding dynamics to direct visualization of the microstructure's evolution. All of these experiments show that yielding is an indirect process in which complex behavior may occur. In Chap. 4, we will use particle image velocimetry to image the flow field of Carbopol in a pipe while it is yielding.

1.2.5 Confinement effects

Many industrial fluids, like cosmetics, condiments, polymer melts, and glass melts exhibit complex non-Newtonian flow behaviour. In some cases, the flow of these products occurs in small geometries, motivating research on their fluid dynamics in confined systems. Some experiments in this area are closely related to real industrial processes, such as freezing and melting of metal oxide gels and porous glasses [57], and thin films of polymer melts [58]. In general, it is found that when the scale of the flow geometry was comparable with the characteristic length scale of the microstructure of the complex fluids their rheology deviated from their

bulk behavior. Confinement effects are also interesting from a purely fundamental perspective. Cohen et al. studied the microstructure of colloidal suspensions when they were confined between two flat plates [59]. They found that the layers of colloidal particles buckled and that particles moved between layers to fill the volume in a more efficient way. Klein et al. studied Octamethylcyclotetrasiloxane between two parallel plates [60]. They observed that the material changed from a viscous liquid to a solid when the separation between the plates decreased below seven times the thickness of the molecular layer [60]. Goyon et al. investigated the flow of a concentrated yield-stress emulsion in two-dimensional microchannels, and demonstrated the departure of the rheology from the bulk rheology when the height of the channel became small enough [61, 62]. They observed that the fluid was sheared even in regions where the stress was smaller than the bulk yield stress, and fitted the measured velocity profiles using a non-local fluidity model. This model suggests that the local fluid dynamics does not only depend on the local stress but also on the state of the surrounding fluid. This study reveals the dynamical cooperativity of yield-stress fluids, which is negligible in large systems but becomes more pronounced in small geometries. In Chap. 5, we studied the flow of Carbopol solutions confined to square microchannels with sides ranging from 500 down to 50 μm . In the smaller channels, confinement affects the organization of the microgel particles, and the rheology is observed to be different from the bulk rheology.

1.3 Summary of Present Work

1.3.1 Overview

The flow behaviour of complex fluids is interesting in fundamental science and relevant to applications in many industries. This thesis reports on three experiments on the rheological, mechanical and thermal behaviour of complex fluids. The complex fluids studied are solutions of hydroxyethyl cellulose (HEC), which is a linear polymer in water, and Carbopol, which is a polymer microgel consisting of particles of polyacrylic acid with crosslinkers. HEC is vis-

coelastic and has zero yield stress. Carbopol is a model yield-stress fluid with little thixotropy [29].

1.3.2 Rheology and heat transport properties of a hydroxyethyl cellulose–based MRI tissue phantom

In Chap. 3, we study the rheological properties and heat transport of a saline solution of hydroxyethyl cellulose which has been recommended for use as a tissue phantom in testing the behavior of medical devices in MRI scanners. It has been stated in the standards governing these tests that the viscosity of the fluid used should be large enough that bulk transport or convection currents are not supported [63]. In this study we evaluated a hydroxyethyl cellulose phantom to determine the degree to which it supports convective, as compared to conductive, heat transport. We study the rheological properties of this fluid, and find that it behaves as a typical viscoelastic polymer solution. As a result, it flows in response to local heating, such as would occur due to eddy-current heating of a metallic device in an MR scanner. We use laboratory experiments and numerical simulations to determine the convective and conductive contributions to the heat transport in a simple model of this system. Our results indicate that convective heat transport is of the same order of magnitude as conductive transport under conditions typical of MRI device tests. This indicates that heating tests conducted with this fluid are not completely conservative in terms of estimating local temperature changes for medical devices *in vivo*. It also indicates that convective processes should be included along with conduction in computer simulations of device heating in order to allow accurate comparison with experimental measurements.

1.3.3 Start-up flow of a yield-stress fluid in a vertical pipe

In Chap. 4, we investigate the start-up flow and yielding of a simple yield-stress fluid (Carbopol 940) in a vertical pipe. The Carbopol was displaced from below by a Newtonian

liquid (Fluorinert FC-40) injected at a constant, controlled rate at the bottom of the pipe. Rough and smooth-walled pipes were used to study the effects of wall boundary conditions. The shear stress at the wall was known from the pressure in the Carbopol measured by a pressure gauge fixed on the pipe wall. The shear rate was known from measurements of the velocity profile in the Carbopol made using particle-image velocimetry. In the rough-walled pipe, the yielding involved a long transition with several steps: elastic deformation, the onset of wall slip, yielding at the wall, and finally a steady-state plug flow that is well-described by the predictions of the Herschel-Bulkley model. In contrast, in the smooth-walled pipe, the wall shear stress never exceeded the yield stress. Our results demonstrate the importance of elasticity during the yielding process, particularly for faster displacements.

1.3.4 Confinement effects on the rheology of Carbopol in microchannels

In Chap. 5, we study the flow of Carbopol solutions confined to square microchannels with sides ranging from $500\ \mu\text{m}$ down to $50\ \mu\text{m}$. Velocity profiles in the midplane of the channels were measured using particle image velocimetry. For comparison, we also study the flow of water and an HEC solution that do not have micrometer-scale structure. In the larger channels, the measured velocity profiles in Carbopol agreed well with simulations based on the bulk-scale rheology of the Carbopol and the Herschel-Bulkley model. In contrast, in microchannels with sides of $150\ \mu\text{m}$ or smaller, the velocity profiles could not be fitted by a model with a finite yield stress, but instead were described by a power-law model with zero yield stress. Previous light-scattering studies have shown that Carbopol has structural elements with a length scale greater than $50\ \mu\text{m}$ [64], and we explain the vanishing of the yield stress in terms of the confinement of these structural elements by the microchannels.

Bibliography

- [1] R. G. Larson. *The structure and rheology of complex fluids*, volume 150. Oxford university press New York, 1999.
- [2] A. Morozov and S. E. Spagnolie. *Complex Fluids in Biological Systems*. Springer, 2015.
- [3] D. Bonn, S. Tanase, B. Abou, H. Tanaka, and J. Meunier. Laponite: Aging and shear rejuvenation of a colloidal glass. *Physical Review Letters*, 89:015701, 2002.
- [4] K. K. Chawla and M. A. Meyers. *Mechanical behavior of materials*. Prentice Hall, 1999.
- [5] D. Roylance. Engineering viscoelasticity @ONLINE, 2001.
- [6] E. Wiechert. *Ueber elastische Nachwirkung*. PhD thesis, Königsberg University, 1889.
- [7] A. Fall, F. Bertrand, G. Ovarlez, and D. Bonn. Shear thickening of cornstarch suspensions. *Journal of Rheology*, 56:575–591, 2012.
- [8] S. T. Milner. Relating the shear-thinning curve to the molecular weight distribution in linear polymer melts. *Journal of Rheology*, 40:303–315, 1996.
- [9] S. Chien. Red cell deformability and its relevance to blood flow. *Annual Review of Physiology*, 49:177–192, 1987.
- [10] L. Bergström. Shear thinning and shear thickening of concentrated ceramic suspensions. *Colloids and Surfaces A: Physicochemical and Engineering Aspects*, 133:151–155, 1998.
- [11] H. A. Barnes. Shear-thickening (dilatancy) in suspensions of nonaggregating solid particles dispersed in newtonian liquids. *Journal of Rheology*, 33:329–366, 1989.
- [12] H. M. Laun. Rheological properties of aqueous polymer dispersions. *Macromolecular Materials and Engineering*, 123:335–359, 1984.

- [13] N. J. Wagner and J. F. Brady. Shear thickening in colloidal dispersions. *Physics Today*, 62:27–32, 2009.
- [14] J. F. Brady and G. Bossis. The rheology of concentrated suspensions of spheres in simple shear flow by numerical simulation. *Journal of Fluid Mechanics*, 155:105–129, 1985.
- [15] X. Cheng, J. H. McCoy, J. N. Israelachvili, and I. Cohen. Imaging the microscopic structure of shear thinning and thickening colloidal suspensions. *Science*, 333:1276–1279, 2011.
- [16] G. Ovarlez, S. Cohen-Addad, K. Krishan, J. Goyon, and P. Coussot. On the existence of a simple yield stress fluid behavior. *Journal of Non-Newtonian Fluid Mechanics*, 193:68–79, 2013.
- [17] H. A. Barnes and K. Walters. The yield stress myth? *Rheologica Acta*, 24:323–326, 1985.
- [18] H. A. Barnes. The yield stress—a review or $\pi\alpha\nu\tau\alpha$ $\rho\epsilon\iota$ -everything flows? *Journal of Non-Newtonian Fluid Mechanics*, 81:133–178, 1999.
- [19] G. P. Roberts and H. A. Barnes. New measurements of the flow-curves for Carbopol dispersions without slip artefacts. *Rheologica Acta*, 40:499–503, 2001.
- [20] C. W. Macosko. *Rheology: principles, measurements, and applications*. Wiley-vch, 1994.
- [21] J. Schurz. The yield stress—an empirical reality. *Rheologica Acta*, 29:170–171, 1990.
- [22] P. C. F. Møller, A. Fall, and D. Bonn. Origin of apparent viscosity in yield stress fluids below yielding. *Europhysics Letters*, 87:38004, 2009.
- [23] M. Dinkgreve, J. Paredes, M. M. Denn, and D. Bonn. On different ways of measuring the yield stress. *Journal of Non-Newtonian Fluid Mechanics*, 238:233–241, 2016.

- [24] H. A. Barnes and Q. D. Nguyen. Rotating vane rheometry-a review. *Journal of Non-Newtonian Fluid Mechanics*, 98:1–14, 2001.
- [25] J. R. Stokes and J. H. Telford. Measuring the yield behaviour of structured fluids. *Journal of Non-Newtonian Fluid Mechanics*, 124:137–146, 2004.
- [26] P. Coussot. *Rheometry of pastes, suspensions, and granular materials: applications in industry and environment*. John Wiley & Sons, 2005.
- [27] Q. D. Nguyen and D. V. Boger. Measuring the flow properties of yield stress fluids. *Annual Review of Fluid Mechanics*, 24:47–88, 1992.
- [28] A. E. James, D. J. A. Williams, and P. R. Williams. Direct measurement of static yield properties of cohesive suspensions. *Rheologica Acta*, 26:437–446, 1987.
- [29] P. C. F. Møller, A. Fall, V. Chikkadi, D. Derks, and D. Bonn. An attempt to categorize yield stress fluid behaviour. *Philosophical Transactions of the Royal Society of London A: Mathematical, Physical and Engineering Sciences*, 367:5139–5155, 2009.
- [30] A. Ragouilliaux, G. Ovarlez, N. Shahidzadeh-Bonn, B. Herzhaft, T. Palermo, and P. Coussot. Transition from a simple yield-stress fluid to a thixotropic material. *Physical Review E*, 76:051408, 2007.
- [31] F. Da Cruz, F. Chevoir, D. Bonn, and P. Coussot. Viscosity bifurcation in granular materials, foams, and emulsions. *Physical Review E*, 66:051305, 2002.
- [32] N. Huang, G. Ovarlez, F. Bertrand, S. Rodts, P. Coussot, and D. Bonn. Flow of wet granular materials. *Physical Review Letters*, 94:028301, 2005.
- [33] H. S. Ramaswamy and S. Basak. Rheology of stirred yogurts. *Journal of Texture Studies*, 22:231–241, 1991.
- [34] J. Mewis and N. J. Wagner. Thixotropy. *Advances in Colloid and Interface Science*, 147:214–227, 2009.

- [35] P. Coussot, Q. D. Nguyen, H. T. Huynh, and D. Bonn. Avalanche behavior in yield stress fluids. *Physical Review Letters*, 88:175501, 2002.
- [36] P. Coussot, Q. D. Nguyen, H. T. Huynh, and D. Bonn. Viscosity bifurcation in thixotropic, yielding fluids. *Journal of Rheology*, 46:573–589, 2002.
- [37] C. F. Goodeve. A general theory of thixotropy and viscosity. *Transactions of the Faraday Society*, 35:342–358, 1939.
- [38] H. Usui. A thixotropy model for coal-water mixtures. *Journal of Non-Newtonian Fluid Mechanics*, 60:259–275, 1995.
- [39] D. C. H. Cheng. Hysteresis loop experiments and the determination of thixotropic properties. *Nature*, 216:1099–1100, 1967.
- [40] P. Coussot, J. S. Raynaud, F. Bertrand, P. Moucheron, J. P. Guilbaud, H. T. Huynh, S. Jarny, and D. Lesueur. Coexistence of liquid and solid phases in flowing soft-glassy materials. *Physical Review Letters*, 88:218301, 2002.
- [41] J. Yerushalmi, S. Katz, and R. Shinnar. The stability of steady shear flows of some viscoelastic fluids. *Chemical Engineering Science*, 25:1891–1902, 1970.
- [42] T. Divoux, M. A. Fardin, S. Manneville, and S. Lerouge. Shear banding of complex fluids. *Annual Review of Fluid Mechanics*, 48:81–103, 2016.
- [43] M. Kane, M. Djabourov, J. L. Volle, J. P. Lechaire, and G. Frebourg. Morphology of paraffin crystals in waxy crude oils cooled in quiescent conditions and under flow. *Fuel*, 82:127–135, 2003.
- [44] J. A. Ajienka and C. U. Ikoku. The effect of temperature on the rheology of waxy crude oils. *OnePetro*, 1991.
- [45] L. T. Wardhaugh and DV D. V. Boger. The measurement and description of the yielding behavior of waxy crude oil. *Journal of Rheology*, 35:1121–1156, 1991.

- [46] C. Chang, D. V. Boger, and Q. D. Nguyen. The yielding of waxy crude oils. *Industrial and Engineering Chemistry Research*, 37:1551–1559, 1998.
- [47] C. Chang, Q. D. Nguyen, and H. P. Rønningsen. Isothermal start-up of pipeline transporting waxy crude oil. *Journal of Non-Newtonian Fluid Mechanics*, 87:127–154, 1999.
- [48] G. Vinay, A. Wachs, and J-F. Agassant. Numerical simulation of non-isothermal viscoplastic waxy crude oil flows. *Journal of Non-Newtonian Fluid Mechanics*, 128:144–162, 2005.
- [49] M. R. Davidson, Q. D. Nguyen, C. Chang, and H. P. Rønningsen. A model for restart of a pipeline with compressible gelled waxy crude oil. *Journal of Non-Newtonian Fluid Mechanics*, 123:269–280, 2004.
- [50] G. Vinay, A. Wachs, and I. Frigaard. Start-up transients and efficient computation of isothermal waxy crude oil flows. *Journal of Non-Newtonian Fluid Mechanics*, 143:141–156, 2007.
- [51] A. M. V. Putz and T. I. Burghelea. The solid–fluid transition in a yield stress shear thinning physical gel. *Rheologica Acta*, 48:673–689, 2009.
- [52] T. Divoux, D. Tamarii, C. Barentin, and S. Manneville. Transient shear banding in a simple yield stress fluid. *Physical Review Letters*, 104:208301, 2010.
- [53] T. Divoux, D. Tamarii, C. Barentin, S. Teitel, and S. Manneville. Yielding dynamics of a Herschel-Bulkley fluid: A critical-like fluidization behaviour. *Soft Matter*, 8:4151–4164, 2012.
- [54] T. Divoux, C. Barentin, and S. Manneville. From stress-induced fluidization processes to Herschel-Bulkley behaviour in simple yield stress fluids. *Soft Matter*, 7:8409–8418, 2011.

- [55] T. Gibaud, D. Frelat, and S. Manneville. Heterogeneous yielding dynamics in a colloidal gel. *Soft Matter*, 6:3482–3488, 2010.
- [56] B. Rajaram and A. Mohraz. Dynamics of shear-induced yielding and flow in dilute colloidal gels. *Physical Review E*, 84:011405, 2011.
- [57] H. K. Christenson. Confinement effects on freezing and melting. *Journal of Physics: Condensed Matter*, 13:R95, 2001.
- [58] G. Luengo, F. J. Schmitt, R. Hill, and J. Israelachvili. Thin film rheology and tribology of confined polymer melts: contrasts with bulk properties. *Macromolecules*, 30:2482–2494, 1997.
- [59] I. Cohen, T. G. Mason, and D. A. Weitz. Shear-induced configurations of confined colloidal suspensions. *Physical Review Letters*, 93:046001, 2004.
- [60] J. Klein and E. Kumacheva. Confinement-induced phase transitions in simple liquids. *Science*, pages 816–816, 1995.
- [61] J. Goyon, A. Colin, G. Ovarlez, A. Ajdari, and L. Bocquet. Spatial cooperativity in soft glassy flows. *Nature*, 454:84, 2008.
- [62] J. Goyon, A. Colin, and L. Bocquet. How does a soft glassy material flow: finite size effects, non local rheology, and flow cooperativity. *Soft Matter*, 6:2668–2678, 2010.
- [63] ASTM. *F2182-11a: Standard Test Method for Measurement of Radio Frequency Induced Heating On or Near Passive Implants During Magnetic Resonance Imaging*. ASTM International, 2011.
- [64] D. Lee, I. A. Gutowski, A. E. Bailey, L. Rubatat, J. R. de Bruyn, and B. J. Frisken. Investigating the microstructure of a yield-stress fluid by light scattering. *Physical Review E*, 83:031401, 2011.

Chapter 2

Materials and methods

2.1 Introduction

This chapter describes the materials and important techniques, instruments, and software used in this work. First, the two polymer solutions used in this work will be introduced. Then we will explain how a shear rheometer is used to measure the viscoelastic properties of materials, and describe the measuring tools and rheometric tests used in this work. We will discuss the principles of Particle Image Velocimetry (PIV), the technique used for visualizing the flow in all of the experiments presented in this thesis. Apparatus built for one of the experiments will be described. The LabVIEW software used for the automation of the instruments presented, and the fabrication of our microfluidic devices will be introduced. Finally, Ansys Fluent, the software used to do the computational fluid dynamics, will be described.

2.2 Materials

2.2.1 Hydroxyethyl cellulose

Hydroxyethyl cellulose (HEC) is a hydrophilic polymer which forms a three-dimensional network structure when dissolved in water [1]. Fig. 2.1 shows the repeat unit of its chemical

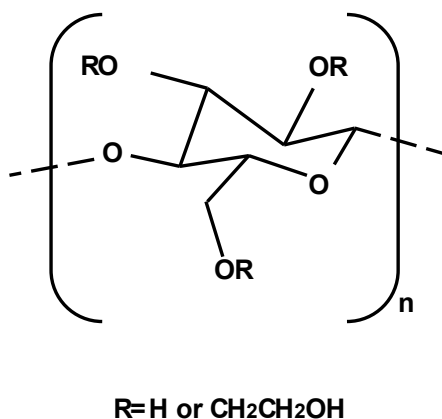


Figure 2.1: The chemical formula of Hydroxyethyl cellulose (HEC).

formula. The recipe and procedure for making the HEC solution will be discussed in detail in Chap. 3. HEC is widely used as an ingredient in industries, including use in building materials, toothpaste, ink, drugs and food. HEC was used in two experiments in this thesis: one which explored its suitability as a tissue phantom for use in Magnetic Resonance Imaging (MRI) tests (Chap. 3) and another on flow in a microfluidic device (Chap. 5).

MRI is a popular technique for medical imaging. However, localized eddy-current heating in medical implants or devices, caused by the rapidly varying electromagnetic field, may damage the devices or even injure patients [2]. It is therefore necessary to test how these medical devices behave when they are placed in MRI systems. Polymeric materials known as tissue phantoms, which are intended to mimic the properties of real tissue, are used in these tests. A good tissue phantom should have dielectric, mechanical, and thermal properties similar to real tissue. HEC is often used as an MRI phantom [3].

2.2.2 Carbopol

The other material we used in this work is Carbopol 940, which is a polymer microgel consisting of polydisperse particles of cross-linked polyacrylic acid chains. Carbopol is widely used as a rheology modifier in cosmetics, foods, and medicines [4]. Fig. 2.2 shows the chemical formula of polyacrylic acid. In Carbopol, long chains of polyacrylic acid are linked together by polyalkenyl polyethers or divinyl glycol [5]. Carbopol is soluble in water, and when initially dissolved has a low $pH \sim 3$ due to ionization of the carboxylic acid groups. When neutralized by adding NaOH, the osmotic pressure of the Na^+ counterions [6] causes the polymer particles to swell to the extent that the microgel particles interact to form a jammed gel structure. The details of the preparation of our Carbopol solutions will be described in Chap. 4. Carbopol solutions are viscoelastic and have a yield stress. The yield stress behaviour is associated with the jamming of the microgel particles [7, 8, 9]. Carbopol has very low thixotropy, and is thus close to being an ideal yield stress fluid [10]. Because of this, it is used extensively as a model yield stress fluid [11]. Several groups have attempted to measure the size of the Carbopol particles in solution. Lee et al. used static light scattering to measure the particle size of Carbopol [7]. They observed two distinct length scales, a scale on the order of a few nanometers which did not vary with experimental conditions, and a larger scale which depended on the pH and concentration of the sample. They associated the smaller scale with the highly crosslinked polymer core of the swollen particles and the larger scale with the size of the swollen polymer blobs. The microstructure of Carbopol is shown schematically in Fig. 2.3. This larger scale ranged from a few microns to above $50 \mu m$ depending on Carbopol concentration and pH . Jofore et al. used confocal microscopy to measure the size of the Carbopol particles, and showed that the swollen particles have an average size between 10 and $40 \mu m$ [6]. Géraud et al. measured the size of the swollen microgel particles using confocal microscopy, and found it to be on the order of a few microns [12]. The individual Carbopol particles probably overlap significantly and the difference may indicate that the size measured by Lee and Jofore is that of an aggregate of several interacting particles rather than the size of an individual particle [6].

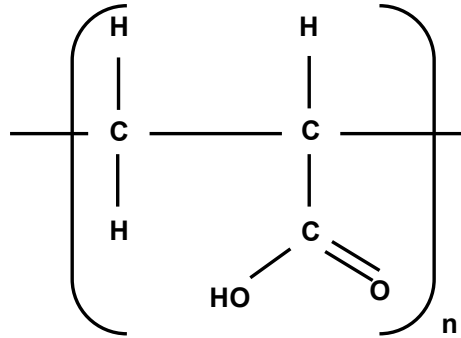


Figure 2.2: The chemical formula of polyacrylic acid.

It may also reflect differences in the details of sample preparation.

2.3 Techniques

In this section, the two main techniques used in this work will be described: shear rheometry for rheological measurements and Particle Image Velocimetry (PIV) for flow visualization.

2.3.1 Shear Rheometry

A rotational shear rheometer is an instrument used to measure the way a fluid flows in response to applied stress or strain. Measurements can be performed by applying a known shear stress and measuring the resulting shear rate, or vice-versa. The former mode is referred to as stress-controlled, and the later one is strain-controlled. Modern, high-quality stress-controlled rheometers have software that allow them to mimic strain-controlled operation. Several different measuring geometries are commonly used in rotational rheometry, including cone-and-plate, plate-plate, and concentric cylinders (Couette). In the experiments described in this

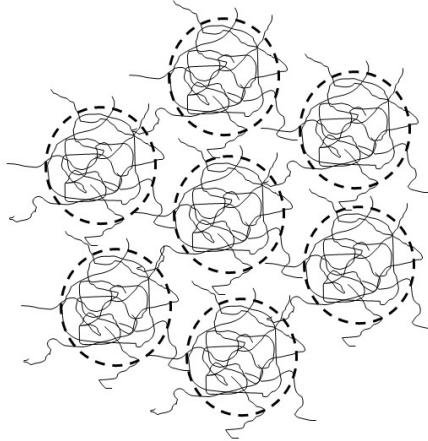


Figure 2.3: The microstructure of Carbopol. The dashed circles represent the swollen polymer blobs.

thesis, we used cone-and-plate tools to characterize our samples. Fig. 2.4 is a sketch of a cone-and-plate tool. The cone is truncated by a small amount. If extrapolated, the tip of the cone would just touch the bottom plate. The sample fluid is sandwiched between the upper cone and the lower plate. Our measurements were done using stress-controlled rheometers, in which the upper cone rotates, while the plate is fixed. A known torque is applied, and the rotation (strain) is measured. In our experiments, the cone angle θ_0 was 4° , which is small enough that the small-angle approximation is valid. The applied shear stress is

$$\tau = \frac{3M}{2\pi R^3}, \quad (2.1)$$

where M is the torque applied to the cone, and R is the cone's radius. In this geometry, the shear rate in the sample fluid is uniform, and is given by

$$\dot{\gamma} = \frac{\Omega}{\theta_0}. \quad (2.2)$$

Here, Ω is the measured angular velocity of the rotating cone.

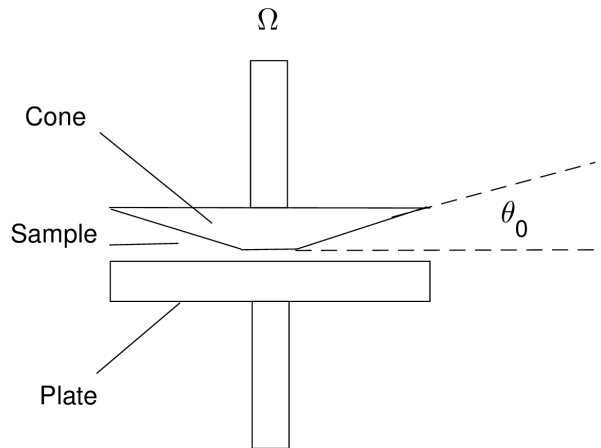


Figure 2.4: A schematic diagram of the cone-and-plate measuring tool of the shear rheometer. Ω is the angular velocity of the rotating cone. θ_0 is the cone angle.

We used two types of rheological tests in this work: measurement of the steady-shear flow curve and small amplitude oscillatory shear measurements. The flow curve is measured in strain-controlled mode by varying the shear rate in steps, and measuring the shear stress. In the oscillatory test, also carried out in strain-controlled mode, a sinusoidal strain with a small amplitude is applied to the sample. The strain is given by

$$\gamma = \gamma_0 \sin(\omega t), \quad (2.3)$$

where t is the time, ω is the angular frequency, and γ_0 is the amplitude of the strain. For small strains, the resulting shear stress is also sinusoidal in time, with the same angular frequency:

$$\tau = \tau_0 \sin(\omega t + \phi). \quad (2.4)$$

Here, ϕ is the phase difference between the strain and stress, and τ_0 is the amplitude of the stress. The stress can be written in terms of two components, one in phase with the applied

strain, and one that is 90° out of phase with the strain:

$$\tau = \tau' + \tau'' = \tau'_0 \sin(\omega t) + \tau''_0 \cos(\omega t). \quad (2.5)$$

The elastic modulus is defined as the ratio

$$G' = \frac{\tau'_0}{\gamma_0}, \quad (2.6)$$

and the viscous modulus is

$$G'' = \frac{\tau''_0}{\gamma_0}. \quad (2.7)$$

G' is also called the storage modulus, as it is proportional to the amount of energy per unit volume stored in elastic deformation of the sample over one cycle, while G'' is also referred to the loss modulus, as it is the amount of energy dissipated by viscosity per unit volume over one cycle [13].

2.3.2 Particle Image Velocimetry (PIV)

Two-dimensional Particle Image Velocimetry (PIV) was used to visualize the instantaneous flow fields in the fluids being studied as a function of the position and time. The experimental fluids were seeded with tracer particles which were assumed to behave as passive scalar particles advected by the fluid flow. In the experiments of Chaps. 3 and 4, the tracer particles were illuminated by a thin laser sheet, and the light scattered by the particles was recorded with a camera at certain time intervals. In the microfluidic experiments described in Chap. 5, the tracer particles were illuminated by a light source, and imaged with a camera attached to a microscope. The recorded video frames were analyzed with PIV software, the principles of which will be explained below.

PIV determines the mean displacement of particles within a region, referred to as an interrogation window, by calculating the spatial cross-correlation function of two images taken at

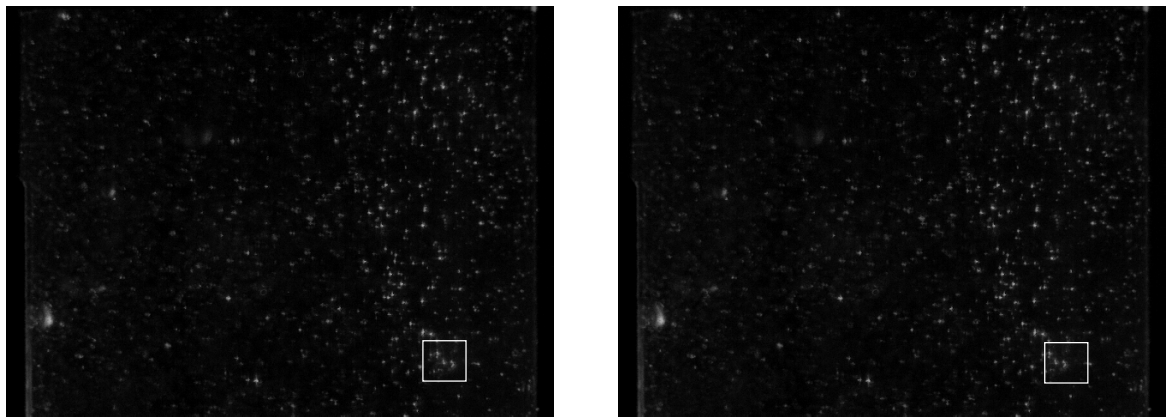
Frame 1 at time t Frame 2 at time $t + \Delta t$

Figure 2.5: Two successive video frames used for PIV analysis. The bright points are small particles suspended in the experimental fluid and illuminated by a light source. The squares in the frames are interrogation windows.

different times. The average velocity in the interrogation window is then calculated by dividing the displacement by the time interval between images. Fig. 2.5 shows two successive video frames, one recorded at time t and the next at time $t + \Delta t$. The spatial cross-correlation and the velocity field were calculated using the MATPIV package implemented in MATLAB by Sveen [14]. The cross-correlation function is given by

$$S(\Delta x, \Delta y) = \sum_{x,y} (I_1(x, y) - I_2(x + \Delta x, y + \Delta y))^2. \quad (2.8)$$

Here, $I_1(x, y)$ is the light intensity at coordinate (x, y) in an interrogation window in Frame 1. $I_2(x + \Delta x, y + \Delta y)$ is the intensity at coordinate $(x + \Delta x, y + \Delta y)$ in the same interrogation window in Frame 2. $(\Delta x, \Delta y)$ is the average displacement of the fluid in this interrogation window. The most accurate $(\Delta x, \Delta y)$ is found by trying different values of $(\Delta x, \Delta y)$ to minimize $S(\Delta x, \Delta y)$ [15]. The velocity vector is the displacement vector $(\Delta x, \Delta y)$ divided by Δt . This calculation is repeated for all interrogation windows to obtain the velocity vectors over the whole image. In MATPIV, this calculation starts with large interrogation windows with a pixel size of 64×64 . Then the frames are divided into smaller windows with a pixel size of 32×32 , for which the calculation uses the result from the former iteration as an initial guess. The calculation goes down to windows with a pixel size of 8×8 , to optimize the results. MATPIV allows the user to exclude regions of the image that are not of interest and to filter out velocity vectors which are dramatically larger or smaller than neighbouring vectors [14].

2.4 Apparatus

In this section, we will describe the set-up of the experiment used in Chap. 4 to study the yielding of Carbopol, the Labview software used for instrument control and data acquisition in the experiments in Chaps. 3 and 4, and the fabrication of the microfluidic devices used for the experiments discussed in Chap. 5.

2.4.1 Apparatus for yielding experiments

Fig. 2.6 shows the overall set-up of the experiment used in Chap. 4 to investigate the startup flow of Carbopol in a pipe. Fig. 2.7 shows some of the components in more detail, including the rough-walled pipe, pressure gauges, reservoir sealed with a piston, laser, light slit, and cylindrical lens. The red dashed line in the pipe in the left-hand image in Fig. 2.7 is the interface between Carbopol and a Newtonian fluid, Fluorinert. The Fluorinert was contained in a reservoir sealed with a piston, which was driven by an actuator (Newport) at a constant speed. The back of the reservoir was fixed in place by a holder. During the experiments, the actuator pushed the piston, and the Fluorinert was injected from the reservoir into the bottom of the pipe, displacing the Carbopol from below. The wall shear stress in Carbopol was known from the pressure in the Carbopol, which was measured by the pressure gauges fixed on the pipe wall. Two voltmeters (KEITHLEY) were connected to the pressure gauges. The pressure gauges produced a voltage signal, which was monitored by the voltmeters and then transferred to the computer. Images of the tracer particles suspended in the Carbopol were obtained using a computer controlled ccd camera, and then saved on a computer. The experimental details are described fully in Chap. 4.

2.4.2 NI LabVIEW

LabVIEW was used to control the experiments and acquire data from the measuring instruments. It is a graphically-based programming language developed by National Instruments. A LabVIEW program is written in the form of a graphical block diagram (LabVIEW-source code), in which the different functions are connected by drawing wires that transfer variables. LabVIEW controls instruments through the sub-programs called virtual instruments, or VIs. Each VI has a block diagram and a front panel. The front panel includes input controls, through which users provide information to the VI, and displays showing the output of the VI, which could include the data measured by the instrument. Front panel inputs and displays appear as terminals in the block diagram. GPIB, USB, or other drivers provided by National Instruments

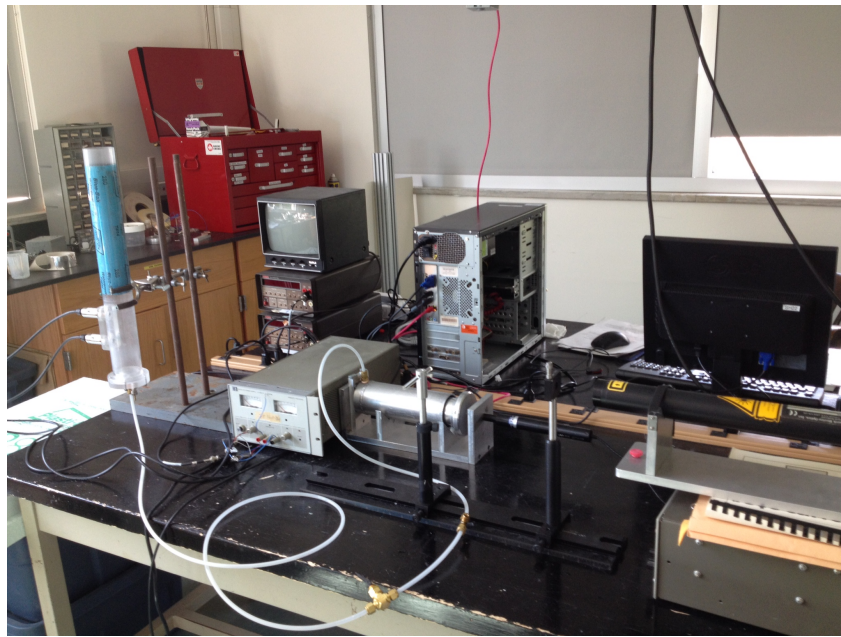


Figure 2.6: The overall set-up of the experiments in Chap. 4.

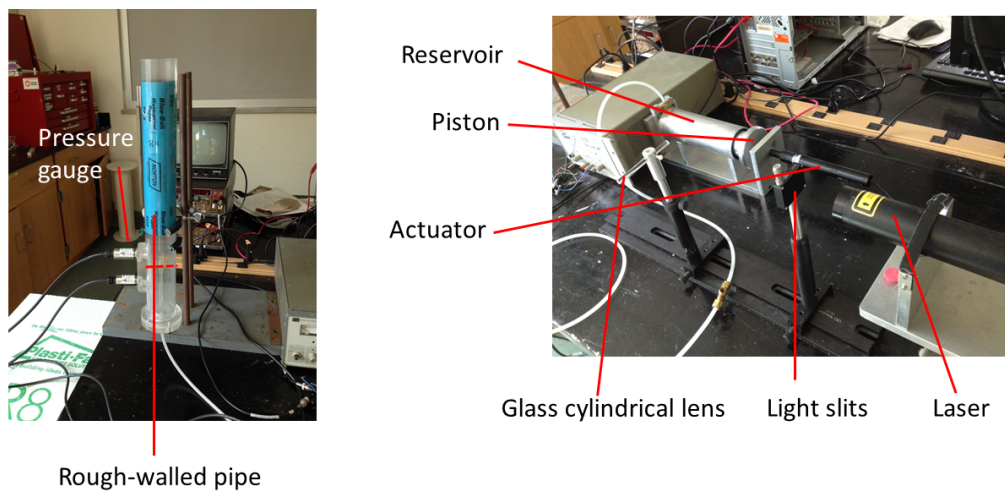


Figure 2.7: Some components of the overall apparatus shown in Fig. 2.6.

are used to interface instruments with the computer.

In the start-up flow experiments described in the previous section, Labview was used to control the camera and the voltmeters connected to the pressure gauges. The LabVIEW VI for controlling the voltmeter (not shown) was downloaded from the Keithley website. A GPIB-USB-HS (IEEE 488) device with USB slots, shown in the left picture in Fig. 2.8, was used to interface two voltmeters to the computer. Fig. 2.9 shows the block diagram of the LabVIEW program used to control the camera used in experiments in Chaps. 3 and 4. A PCI-1407 image acquisition board (National Instruments), shown in the right picture in Fig. 2.8, was used to connect the camera to the computer. Functions from NI's IMAQ library were used to acquire images. These functions directed the camera to acquire images in a certain time interval and save them directly to the computer memory. The functions shown in the block diagram in Fig. 2.9 initialize the camera, grab a single frame, write the image to a specified folder and close the camera. In Fig. 2.9, these IMAQ functions are in a while loop. One image is taken each time the loop is executed. The while loop executes based on the output of a Pause/Continue function in a case structure. This allows the users to start or stop taking images at any time. The Wait Until Next ms Multiple function controls the time interval between iterations of the while loop. The function Elapsed Time2 records the real time of each recorded image, and these times are also saved to the computer.

2.4.3 Fabrication of microfluidic devices

The experiments described in Chap. 5 used microfluidic channels. In general, a microfluidic device contains chambers or channels, with a least one dimension being on the order of microns, through which a fluid flows. Different materials have been used to manufacture microfluidic devices, such as plastics, elastomers, glass and silicon [16]. The fabrication of microchannels made of glass or silicon involves mask-based photolithography, dry and wet etching, and thin film deposition, all of which add complexity to the fabrication process [17]. In our work, polydimethylsiloxane (PDMS) was utilized to fabricate our microchannel devices,



NI GPIB-USB-HS



NI IMAQ PCI-1407

Figure 2.8: Left: GPIB-USB-HS (IEEE 488) used to connect voltmeters to the computer. Right: PCI-1407 (IMAQ) hardware used to connect the camera to the computer.

as it is known for its ability to replicate features, low cost, high transparency, high-pressure tolerance, nontoxicity, and good elastic properties [18, 19]. We fabricated our PDMS microfluidic devices following the procedure described in [20]. Briefly, the top piece of the channel was made by casting the PDMS onto a mold that was machined out of Plexiglas. The bottom piece of the channel was a PDMS film spin-coated onto the glass bottom of a cell culture dish. The two pieces are then bonded together. The details of the fabrication are fully described in Chap. 5.

2.5 Ansys Fluent

Fluent is a general purpose program for modeling fluid flow [21]. In Chap. 5, Fluent was used to simulate the laminar flow of water, HEC and Carbopol solutions through approximately square channels with a fixed inlet velocity. The simulations are broken into several steps:

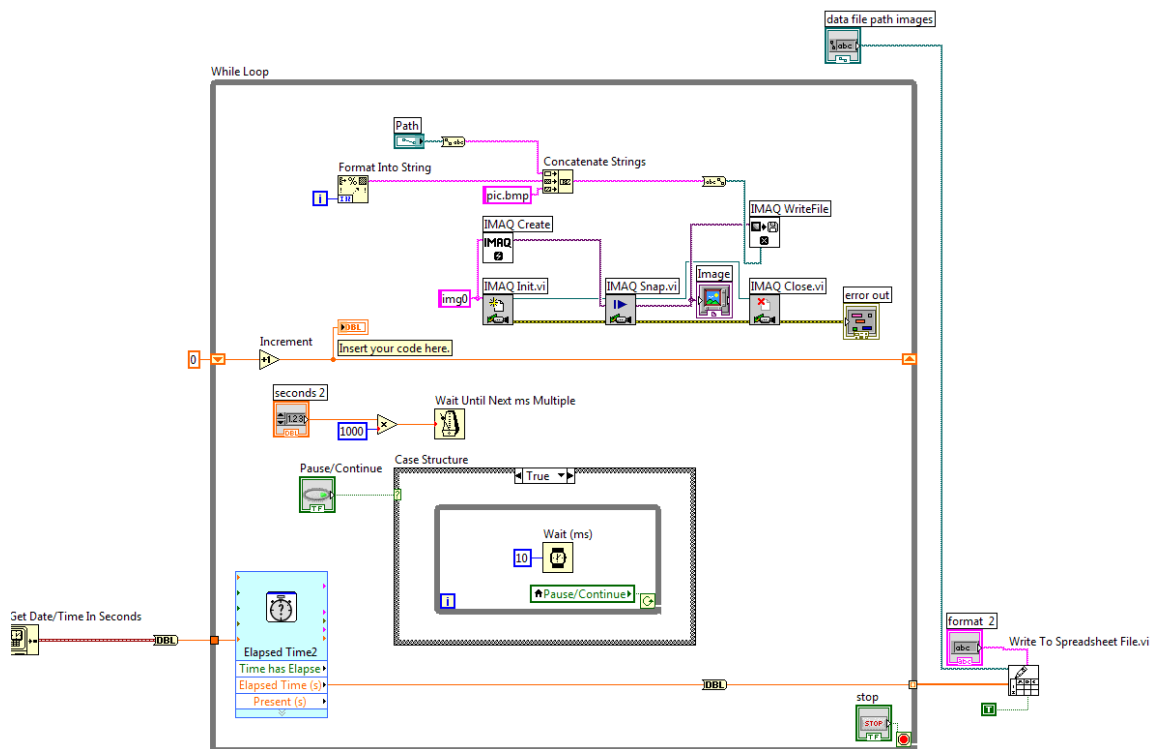


Figure 2.9: The LabVIEW block diagram code controlling the camera in the experiments described in Chaps. 3 and 4.

drawing the flow geometry; meshing the geometry; and setting the boundary conditions, the rheological parameters of the fluid and the mathematical models. In Chap. 5, channels with five different dimensions are used. Fig. 2.10 displays the computational domain used to simulate one of these channels. The channel has a width of $87\ \mu\text{m}$, a height of $65\ \mu\text{m}$ and a length of 1 cm. Fig. 2.11 shows results from one example simulation for water flowing in this channel. The boundary condition of this simulation is a constant inlet velocity equal to 0.00195 m/s. The meshing elements used for this simulation are uniform squares, as shown in the top picture in Fig. 2.11, since we expect the velocity profile of the water to have a parabolic shape, as shown in the middle and bottom graphs in Fig. 2.11. The same mesh was used for simulations of HEC, since its velocity field was also expected to vary smoothly across the channel. Fig. 2.12 shows one example simulation for a Carbopol solution in the same channel. The boundary condition here is a constant inlet velocity of 0.00057 m/s. In this case, since the velocity field for Carbopol was expected to vary rapidly near the walls but show a plug in the middle of the channel, as shown in the middle and the bottom graphs in Fig. 2.12, we used the inflation function in the meshing step of Fluent to produce a finer mesh near the walls than in the central region. In this case, the meshing elements have irregular shapes as illustrated in the top picture in Fig. 2.12. More details of the simulations are provided in Chap. 5.

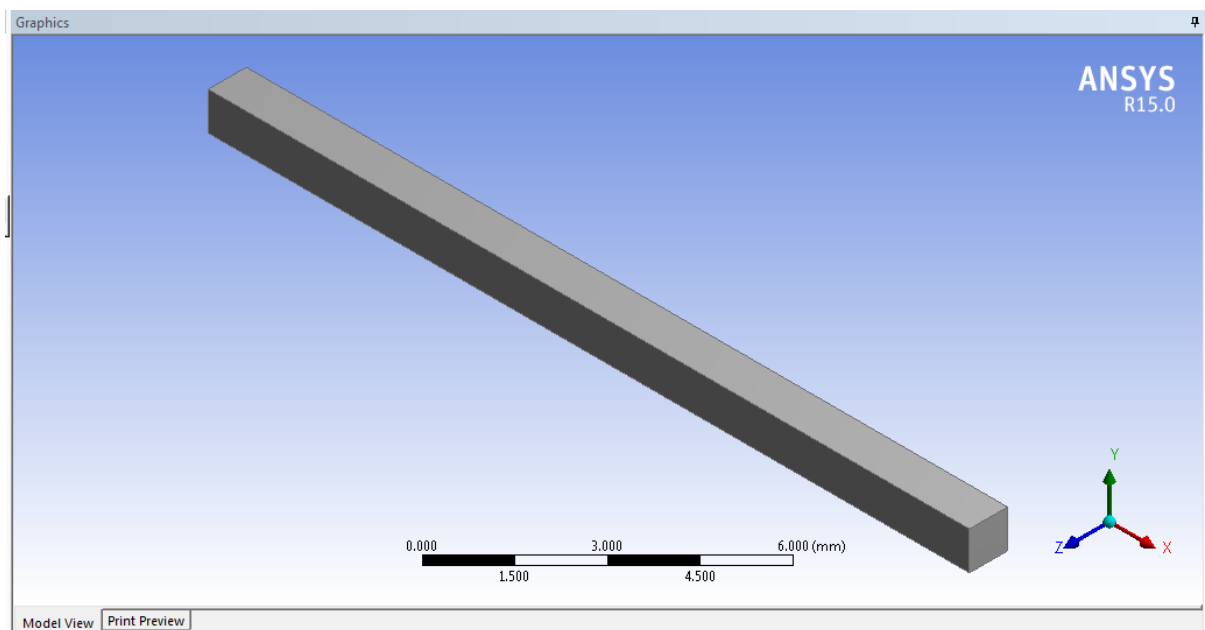


Figure 2.10: The computational domain used to simulate a channel in Chap. 5.

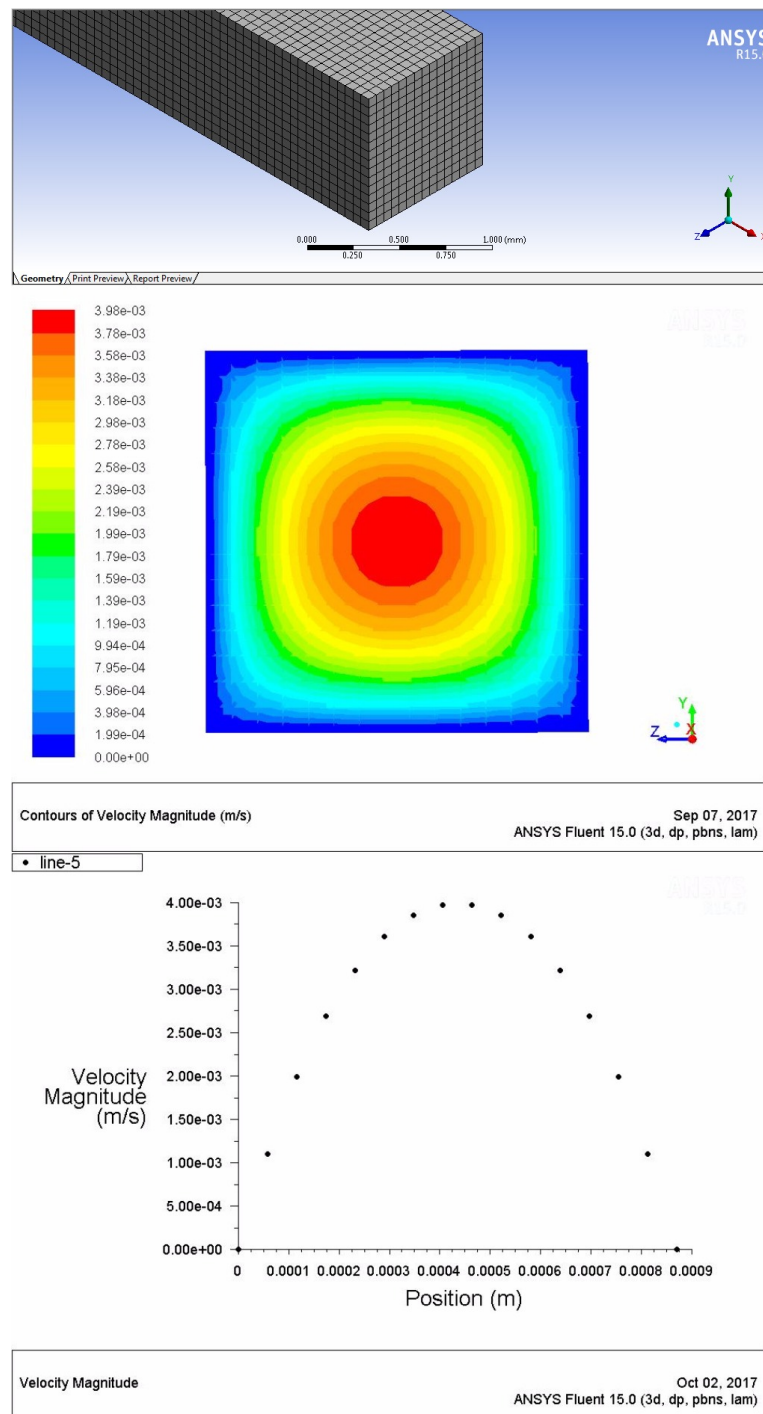


Figure 2.11: The results of a simulation for water flowing in the channel shown in Fig. 2.10. Top: the computational mesh used in the simulations. Middle: the simulated velocity map at the outlet of the channel. Bottom: the simulated velocity profile on the mid-height line at the outlet of the channel.

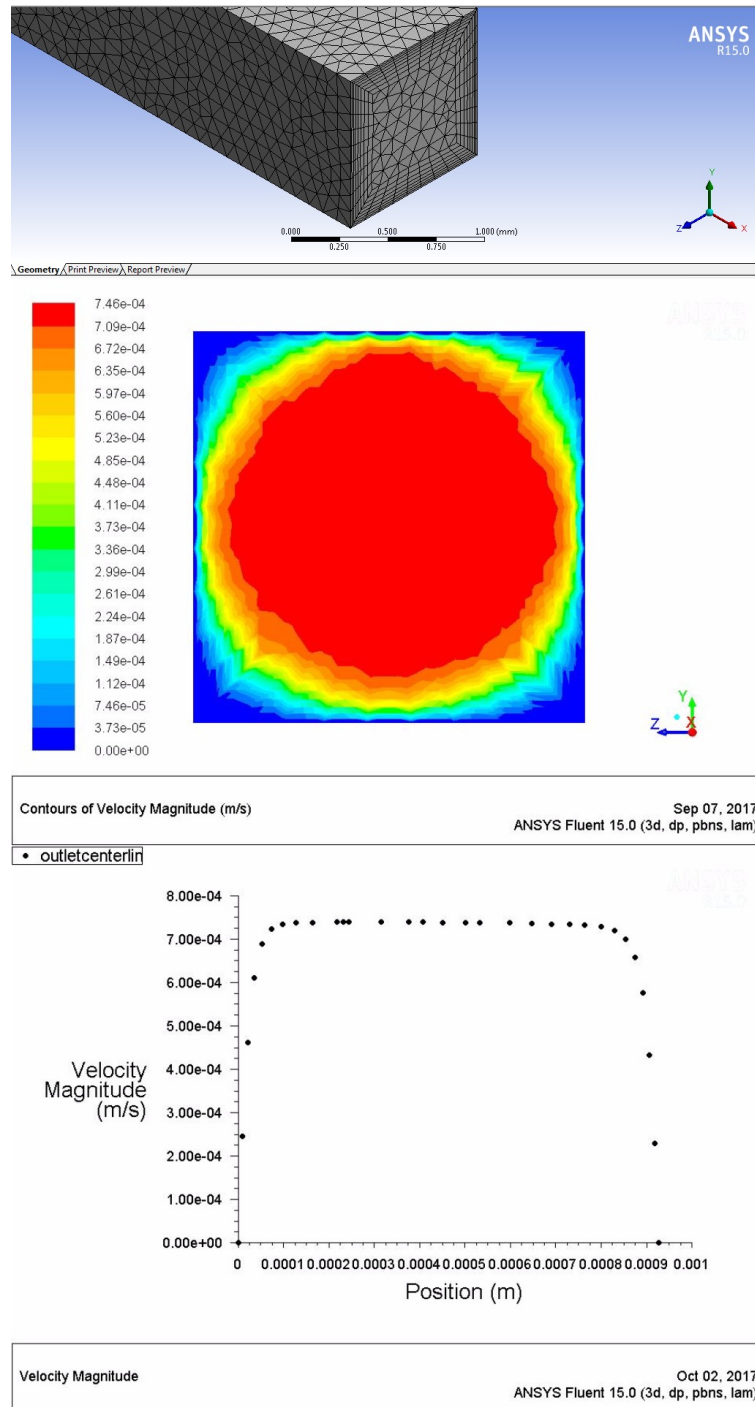


Figure 2.12: The results of a simulation for Carbopol in the channel shown in Fig. 2.10. Top: the computational mesh used in the simulations. Middle: the simulated velocity map at the outlet of the channel. Bottom: the simulated velocity profile on the mid-height line at the outlet of the channel.

Bibliography

- [1] A. Maleki, A. L. Kjøniksen, K. D. Knudsen, and B. Nyström. Dynamical and structural behavior of hydroxyethylcellulose hydrogels obtained by chemical gelation. *Polymer International*, 55:365–374, 2006.
- [2] J. V. Crues, A. M. Karacozoff, and F. G. Shellock. *MRI bioeffects, safety, and patient management*. Biomedical Research Publishing Group, 2014.
- [3] ASTM. *F2182-11a: Standard Test Method for Measurement of Radio Frequency Induced Heating On or Near Passive Implants During Magnetic Resonance Imaging*. ASTM International, 2011.
- [4] D. D. Braun and M. R. Rosen. *Rheology Modifiers Handbook: Practical Use and Application*. Elsevier, 2013.
- [5] Lubrizol. <http://www.lubrizol.com/personalcare/products/carbopol/981.html>, 2013.
- [6] B. D. Jofore, P. Erni, G. Vleminckx, P. Moldenaers, and C. Clasen. Rheology of microgels in single particle confinement. *Rheologica Acta*, 54:581–600, 2015.
- [7] D. Lee, I. A. Gutowski, A. E. Bailey, L. Rubatat, J. R. de Bruyn, and B. J. Frisken. Investigating the microstructure of a yield-stress fluid by light scattering. *Physical Review E*, 83:031401, 2011.
- [8] F. K. Oppong, L. Rubatat, B. J. Frisken, A. E. Bailey, and J. R. de Bruyn. Microrheology and structure of a yield-stress polymer gel. *Physical Review E*, 73:041405, 2006.
- [9] J. Y. Kim, J. Y. Song, E. J. Lee, and S. K. Park. Rheological properties and microstructures of Carbopol gel network system. *Colloid and Polymer Science*, 281:614–623, 2003.
- [10] P. C. F. Møller, A. Fall, and D. Bonn. Origin of apparent viscosity in yield stress fluids below yielding. *Europhysics Letters*, 87:38004, 2009.

- [11] P. C. F. Møller, A. Fall, V. Chikkadi, D. Derks, and D. Bonn. An attempt to categorize yield stress fluid behaviour. *Philosophical Transactions of the Royal Society of London A: Mathematical, Physical and Engineering Sciences*, 367:5139–5155, 2009.
- [12] B. Géraud, L. Jørgensen, C. Ybert, H. Delanoë-Ayari, and C. Barentin. Structural and cooperative length scales in polymer gels. *European Physical Journal E*, 40:5, 2017.
- [13] C. W. Macosko. *Rheology: principles, measurements, and applications*. Wiley, 1994.
- [14] K. Sveen. An introduction to matpiv v. 1.6.1. <http://www.mn.uio.no/math/english/people/aca/jks/matpiv/>, 2004.
- [15] S. de Vet. *On the shape of impact craters and the collapse of an unstable transient cavity in granular media*. PhD thesis, The University of Western Ontario, 2009.
- [16] G. M. Whitesides. The origins and the future of microfluidics. *Nature*, 442:368, 2006.
- [17] K. Ren, J. Zhou, and H. Wu. Materials for microfluidic chip fabrication. *Accounts of Chemical Research*, 46:2396–2406, 2013.
- [18] J. Friend and L. Yeo. Fabrication of microfluidic devices using polydimethylsiloxane. *Biomicrofluidics*, 4:026502, 2010.
- [19] A. Dietzel. *Microsystems for Pharmatechnology: Manipulation of Fluids, Particles, Droplets, and Cells*. Springer, 2016.
- [20] D. Lorusso, H. N. Nikolov, J. S. Milner, N. M. Ochotny, S. M. Sim, S. J. Dixon, and D. W. Holdsworth. Practical fabrication of microfluidic platforms for live-cell microscopy. *Biomedical Microdevices*, 18:78, 2016.
- [21] FLUENT Manual. Ansys fluent 12.0 users guide. <http://users.ugent.be/~mvbelleg/flug-12-0.pdf/>, 2012.

Chapter 3

Rheology and heat transport properties of a HEC-based MRI tissue phantom

3.1 Introduction

Magnetic resonance imaging (MRI) is a commonly-used medical imaging technique [1]. It provides three-dimensional images with relatively high spatial resolution (typically on the order of 1 mm), excellent soft-tissue contrast, and, since it involves no ionizing radiation, has no known negative health effects. A major concern, however, is the interaction of the electromagnetic fields within the MR scanner with active or passive medical devices such as cardiac pacemakers or orthopedic implants. In particular, MRI involves strongly-varying gradient fields in the kHz frequency range and intense RF fields at tens to hundreds of MHz. These cause localized eddy-current heating in conducting materials which could damage or interfere with the operation of an electronic device, or, worse, cause injury to the patient [2]. Because of this, medical devices must be rigorously tested before they can be approved for use in MRI systems. A recent review of safety standards for MRI devices appears in [3]. MRI device testing makes use of tissue phantoms as a proxy for human subjects. Such phantoms would ideally have electromagnetic, transport, and mechanical properties which mimic those of human tissue

under the conditions that prevail in the MR scanner.

Heat is transported in tissue by flowing blood and by thermal conduction. The effect of blood flow is important, but difficult to model in a laboratory phantom. Tissue is solid-like and transports heat by conduction, but not by convective flow of the tissue itself. To properly model this behavior, a phantom material should similarly conduct, but not convect when heated locally. Any thermally-driven flow would remove additional heat from the site of the device under test, reducing the temperature rise in its vicinity. Since testing and certification processes for medical devices are assumed to be conservative, a phantom material which leads to systematic underestimation of local heating must be fully characterized and understood.

A variety of materials have been used as tissue phantoms in MR device testing, including Newtonian fluids such as saline solutions containing ethylene glycol [4], non-Newtonian carageenan [5, 6] and agarose gels [7, 8], and so-called “gelled salines,” made by adding polymer to a salt solution [9, 10, 11, 12, 13]. The most commonly-used phantom materials are saline solutions of polyacrylic acid (PAA) [9, 10, 11] and hydroxyethylcellulose (HEC) [12, 13]; recipes for making these materials are laid out in ASTM publication F2182-11a, “Standard Test Method for Measurement of Radio Frequency Induced Heating On or Near Passive Implants During Magnetic Resonance Imaging” [14]. The polymer increases the viscosity of the solution, with the idea being that convection can be suppressed if the phantom is “sufficiently viscous” [10]. Specifically, Sect. 8.2.4 of ASTM F2182-11a states that “The viscosity shall be great enough so that the phantom material does not allow bulk transport or convection currents. Generally this is achieved by inclusion of a gelling agent.” From a fluid-dynamical perspective, this is not particularly satisfactory. Convection driven by horizontal temperature gradients has no threshold and will not be completely suppressed unless the viscosity is infinite [15]. In other words, to fully eliminate convective heat transport, the phantom must be a true gel with a yield stress that is larger than any thermally-induced stresses.

In this chapter we investigate the rheological and thermal behavior of the HEC-saline solution prescribed by Ref. [14]. Our results show that this material is a typical viscoelastic

polymer solution with no yield stress. We demonstrate both experimentally and by numerical simulation that the convective contribution to heat transport in this material is similar in magnitude to the conductive contribution under conditions that could be encountered in typical MRI device-testing applications. These results lead us to conclude that heating tests conducted with this fluid are not completely conservative in terms of estimating local temperature changes for medical devices in vivo.

3.2 Methods

3.2.1 Sample Preparation

2-hydroxyethyl cellulose (HEC) is a water-soluble linear polymer. In accordance with ASTM Standard F2182-11a [14], we used HEC purchased from Sigma-Aldrich, cat. no. 09368. The polymer is supplied as a white powder. Its molecular weight is not specified, but is estimated by the manufacturer to be approximately 250,000 g/mol. 15.5 g NaCl (> 99% purity, Sigma-Aldrich S9888) was added to 10 l of distilled water and mixed for 2-3 minutes with an IKA RW16 overhead mixer until the salt had completely dissolved. 310 g of HEC powder (3.0% by weight) was added gradually and stirred as above for about 3 hours until the solution was homogeneous. The result is a transparent, homogeneous, viscous solution. The solution was allowed to rest for at least 24 h before it was used in our experiments.

The addition of salt increases the electrical conductivity of the polymer solution to 0.47 S/m at 20°C (a range of 0.40-0.60 S/m is specified in [14]), matching the typical dc conductivity of tissue [16, 17]. As discussed below, the salt also decreases the viscous and elastic moduli of the solution, but does not qualitatively change its rheological behavior.

For flow visualization experiments, 1.0 g fluorescent polyethylene spheres (Cospheric UVPMS-BO-1.03) with a diameter of 215-250 μm and a density of 1.03 g/cm³ were treated with Tween-80 surfactant to make them hydrophilic, then mixed into 4.3 l of the HEC solution. These particles were used as tracers in visualizing the flow field, as discussed below.

3.2.2 Rheological Measurements

The viscoelastic properties of the HEC solution were measured using an AR 1500ex stress-controlled rheometer (TA Instruments) with a 4 cm diameter 4° cone-and-plate geometry. Fine grit sandpaper was affixed to the tool to prevent slip. A home-made environmental housing surrounding the tool minimized evaporation of the sample over the course of the measurements. Temperature was controlled to ± 0.1 K using a Peltier plate controller. Viscosity was measured under steady shear for shear rates $\dot{\gamma}$ from 0.0047 to 300 s^{-1} at several temperatures and for a range of equilibration times at each shear rate. The viscous and elastic moduli, G'' and G' respectively, were measured using small-amplitude oscillatory shear for angular frequencies ω from 0.05 to 500 s^{-1} . We used a controlled stress amplitude of 0.014 Pa, which we confirmed was in the linear viscoelastic regime under all experimental conditions. To investigate the effect of aging of the HEC solutions, measurements were performed on both fresh solutions and on solutions that had been stored in a closed container at room temperature for three weeks.

3.2.3 Heat transport and flow measurements

Heat transport in a fluid results from a combination of thermal conduction and convection. The total heat flux \vec{j} between two points at temperatures T_0 and $T_0 + \Delta T$ is given by

$$\vec{j} = -D\nabla T - \rho C \Delta T \vec{u}, \quad (3.1)$$

where D is the thermal conductivity, ρ the fluid density, C the heat capacity at constant pressure, and \vec{u} the fluid velocity. The first term on the right hand side of Eq. (3.1) is the conductive heat transport, which is proportional to the temperature gradient ∇T , and the second term is the convective contribution.

As discussed in Sec. 3.1, heat transport in a tissue phantom is assumed to be conductive under normal testing conditions. To study the degree to which this is the case in an HEC phantom we used the experimental set-up shown in Figure 3.1. 4.3 l of HEC solution containing

suspended tracer particles was poured into a glass tank of length 29.9 cm, width 14.8 cm, and total depth 19.0 cm, giving a fluid depth of 9.7 cm. A 400 W cylindrical immersion heater (Omega, EMH-060) controlled with a variable transformer was mounted vertically at the left-hand side of the tank. This heater mimics localized heating in an MRI test due, for example, to eddy-current heating of a medical device. The tank rested on a table in our lab but was not otherwise insulated; room temperature was approximately 19 ± 1 °C. Temperature in the fluid was measured 2.5 times per second at four points approximately 0, 3, 9, and 17 cm from the right-hand edge of the heater and at depths ranging from 1.5 to 3.3 cm from the free surface of the fluid, using a computer-controlled Neoptix OmniFlex temperature monitoring system with fluoroptic temperature probes (Neoptix T1C-05-PP05), referred to below as probes 1-4 respectively. For comparison, measurements were also performed using water as the test fluid.

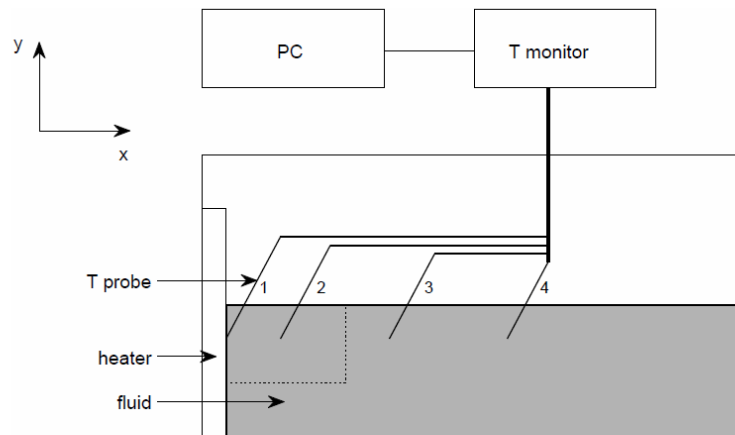


Figure 3.1: The experimental set-up used to measure convective heat transport in fluids. A tank contains the fluid of interest, which is seeded with small flow visualization particles. The tank is 30.5 ± 0.1 cm in length, 21.2 ± 0.1 cm in height, and 15.5 ± 0.1 cm in width into the page. A heater is mounted at the left-hand edge of the tank, and the temperature measured at four locations with optical temperature probes. The visualization particles are illuminated by a laser sheet coming in from the right-hand side of the diagram, and their motion is recorded by a video camera looking into the page. The dotted rectangle indicates the region imaged by the camera. The origin of the x - y coordinate system shown is at the bottom left corner of the tank.

The velocity field in the HEC solution was measured using particle image velocimetry (PIV). The beam from a 12 mW, 6328 Å laser (Research Electro-Optics) was formed into a thin sheet using a cylindrical lens and passed through the tank from right to left from the perspective of Figure 3.1, illuminating a vertical (x - y) plane in the center of the tank. Laser light scattered from the suspended tracer particles was detected with a ccd camera positioned in front of the tank. Images of the tracer particles in a region approximately 6.6 cm wide by 4.7 cm high at the top left corner of the fluid, as indicated in Figure 3.1, were recorded by the computer at a fixed frame rate with the aid of a LabView program (National Instruments, Austin TX). The two-dimensional velocity field in this region was calculated from these images using the MatPIV software package [18].

3.2.4 Numerical simulations

Time-dependent flow and heat transfer in the fluids of interest were modeled using the Laminar Flow and Heat Transfer in Fluids modules of the COMSOL Multiphysics software (COMSOL Inc., Burlington MA). Surface tension at the fluid-air interface and the Marangoni effect were taken into account, although they contribute only a small correction to the dominant density-driven convective flow in the systems studied. The values of surface tension and the Marangoni coefficient were taken to be the same as for water. The temperature dependence of the properties of water is built into COMSOL. For simulations of HEC, the shear-rate and temperature dependence of the viscosity were modelled using the experimental measurements described in Sec. 5.3 below. Numerical integration of the equations for the velocity and temperature fields was performed using the backward differentiation formula. Results were output every 5-10 minutes of simulated time, depending on the system studied. Sufficient intermediate steps were taken to ensure convergence.

The two-dimensional simulation domain was a rectangle with dimensions corresponding to the length and depth of the fluid in the tank described in Sec. 3.2. The finite element mesh used had a higher density of elements near the heater and the fluid-air boundary. The heater at the

left-hand boundary was modelled by a constant temperature equal to that measured at the heater and a no-slip boundary condition. The bottom and right boundaries had no slip and a constant temperature equal to room temperature. The top boundary was modelled as a free fluid-air surface with no specified temperature and a slip boundary condition. The initial velocity of the fluid was set to zero, and the initial temperature to room temperature, everywhere in the computational domain.

3.3 Results

3.3.1 Rheology

Results from steady-shear measurements at 25°C are plotted in Figure 3.2 for a freshly-mixed 3wt% saline HEC solution and for a solution that had been allowed to age for three weeks. The shear stress σ is plotted as a function of shear rate $\dot{\gamma}$ in Figure 3.2(a), while Figure 3.2(b) shows the viscosity $\eta = \sigma/\dot{\gamma}$ vs. $\dot{\gamma}$. The fluid is shear-thinning and the viscosity approaches a Newtonian plateau at low $\dot{\gamma}$. The viscosity of the aged HEC solution is lower than that of the fresh material, with the difference being about a factor of three at low shear rates. We observed no evidence of either a yield stress or a high-shear-rate viscosity plateau over the range of shear rates studied.

The viscosity data were fit to the Cross model [19],

$$\eta = \frac{\eta_0}{1 + (\dot{\gamma}/\dot{\gamma}_0)^{1-n}}, \quad (3.2)$$

where η_0 is the zero-shear-rate viscosity, $\dot{\gamma}_0$ is a characteristic shear rate that corresponds roughly to that at which shear thinning becomes significant, and n is a power law index. Fits to Eq. (3.2) are shown in Figure 3.2(b) and describe the data well. The inset to Figure 3.2 shows that η_0 is independent of the waiting time allowed for the system to relax at each shear rate, confirming that our measurements were made with the fluid in a steady state. The zero-

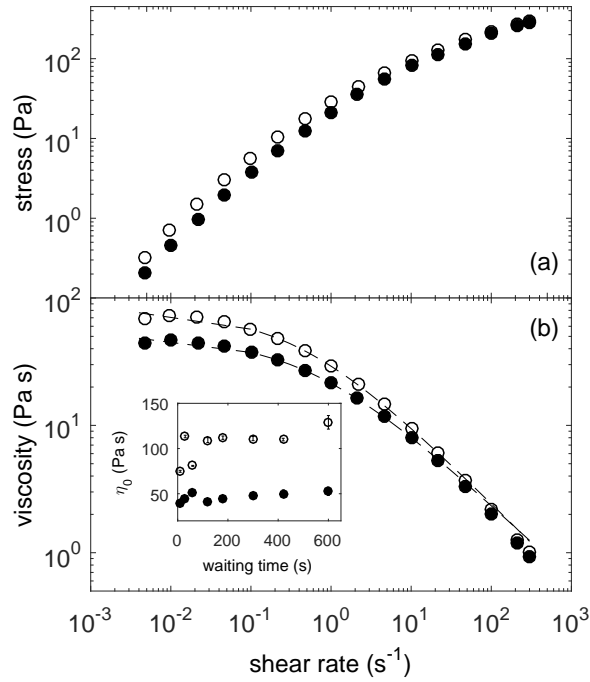


Figure 3.2: (a) The shear stress σ as a function of shear rate $\dot{\gamma}$ of the HEC-saline solution at 25°C. The waiting time at each value of $\dot{\gamma}$ was 1 min. (b) Viscosity η obtained from the data plotted in (a). The dashed lines are fits to the Cross model, Eq. (3.2). The open circles are for fresh HEC, while the filled circles are for the aged solution. The inset shows the viscosity at a $\dot{\gamma} = 1 \text{ s}^{-1}$ measured with different values of the waiting time.

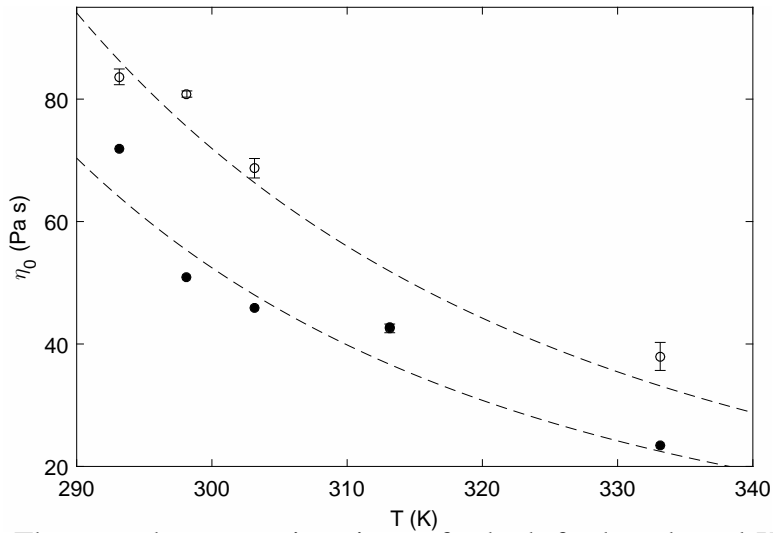


Figure 3.3: The zero-shear-rate viscosity η_0 for both fresh and aged HEC solutions plotted as a function of temperature. The open and filled circles are data for the fresh and aged HEC solutions, respectively. The dashed lines are fits to Eq. (3.3), as discussed in the text.

shear-rate viscosity of the fresh HEC-saline solution is roughly a factor of 10^4 larger than that of water.

The effect of temperature on η_0 is illustrated for both fresh and aged HEC solutions in Figure 3.3. Although there is some scatter in the data, the observed temperature dependence is reasonably well-described by an Arrhenius model [20],

$$\eta_0 \propto e^{E_a/RT}, \quad (3.3)$$

where E_a is an activation energy, R the gas constant, and T the absolute temperature. Fits to the data give $E_a = 19 \pm 6$ kJ/mol and 21 ± 7 kJ/mol for the fresh and aged solutions, respectively; these values are equal within their uncertainties.

Figure 3.4 shows the master curve for the viscous and elastic moduli, G'' and G' respectively, of the fresh HEC solution. The data were measured under small-amplitude oscillatory shear at temperatures ranging from 20°C to 60°C and scaled to a reference temperature of 25°C using time-temperature superposition [20]. The angular frequency ω was scaled by a temperature-dependent factor α and the moduli by a factor β to superimpose the crossover point at which the two moduli are equal. The quality of the superposition is excellent over the range of temperatures and frequencies studied; similar results were obtained for the aged solution. Data measured with a solution containing the same concentration of HEC but no salt (not shown) were qualitatively similar, but with G' and G'' roughly a factor of two higher and a slightly lower crossover frequency. The frequency scaling factor $\alpha(T)$ is plotted for both the fresh and aged solutions in the inset to Figure 3.4. β , the scaling factor of the moduli, is not shown, but was approximately 1 at all temperatures. The results shown in Figure 3.4 are typical for an entangled polymer solution. Both moduli increase with increasing frequency, $G'' > G'$ at low frequencies, and there is a crossover frequency ω_c above which $G' > G''$. Power-law fits to the lowest-frequency data for the fresh HEC, shown as dashed lines in Figure 3.4, give power-law indices of 0.95 ± 0.13 and 0.76 ± 0.15 for G' and G'' , respectively. Results

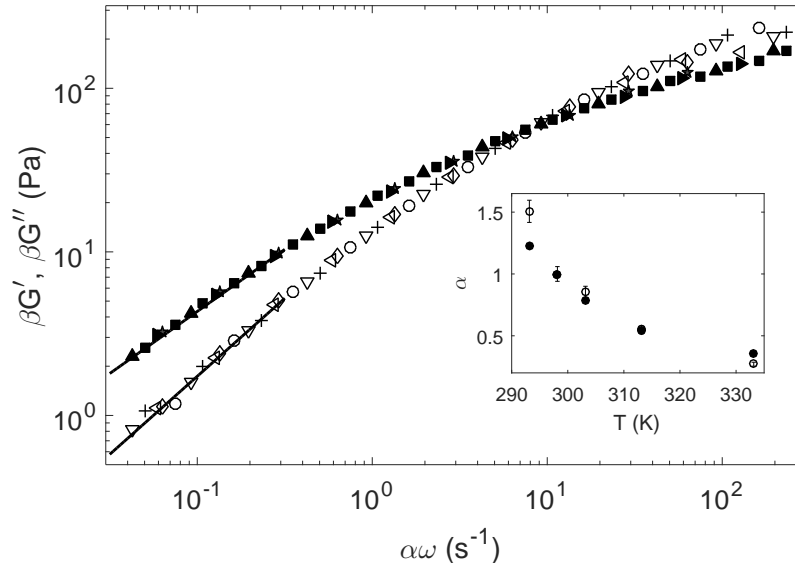


Figure 3.4: Elastic and viscous moduli of the fresh HEC-saline solution, scaled to a temperature of 25°C using time-temperature superposition. The different symbols indicate data recorded at different temperatures: \circ : 20°C, \square : 25°C, ∇ : 30°C, \triangle : 40°C, \diamond : 60°C. Solid symbols are G'' and open symbols are G' . The dashed lines are power-law fits to the lowest-frequency data. The inset shows the frequency scaling factor α for fresh (open symbols) and aged (solid symbols) HEC-saline solution.

for the aged solution are similar. These power-law indices are lower than the values of 2 and 1, respectively, that are predicted by the simple Maxwell model, perhaps indicating that our lowest-frequency data are not in the terminal regime, or, more likely, that the polymer is significantly polydisperse. The crossover frequency ω_c characterizes the slowest relaxation rate in the polymer system and corresponds to a longest relaxation time $\tau_c = 2\pi/\omega_c$. The roughly exponential decrease of α with increasing T indicates that polymer relaxation is more rapid at higher temperatures, as expected. Aging decreases both moduli slightly, but the temperature dependence of the moduli does not change significantly with age.

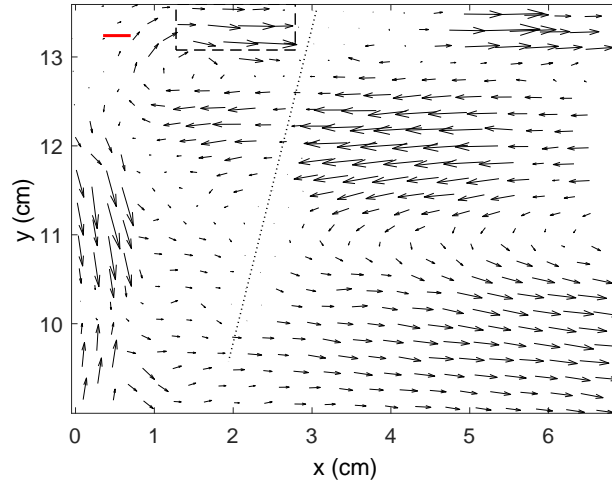


Figure 3.5: The velocity field measured in an experiment using water. The field of view is at the top left of the fluid, in a vertical plane through the center of the tank, as discussed in the text. The edge of the heater is at $x = 0$; the bottom of the tank is at $y = 0$, and the free surface of the fluid is at the top of the image. The tip of temperature probe 1 is close to the heater, and the dotted line shows the approximate position of temperature probe 2. The temperature difference between these two probes was 4.2 K. The length of the scale bar at the top left corresponds to a velocity of 0.05 cm/s.

3.3.2 Thermal convection

To provide a baseline for our measurements of convective flow in the polymer phantom material, we first studied the flow induced in water by the heater at the side of the tank. 6.0 l of water containing fluorescent tracer particles was poured into the tank to a depth of 13.6 cm. The measurements were made several minutes after the heater in the tank had been turned on, but the system was far from a steady state. At the time of the measurements, the temperature probe closest to the heater was 4.2 K above ambient room temperature. Figure 3.5 shows the velocity field in the upper left corner of the fluid, in the x - y plane illuminated by the laser sheet. These data were extracted from pairs of images recorded 0.25 s apart. Immediately adjacent to the heater, there is a narrow region of strong upflow that is not resolved by our PIV system. A complex recirculating flow is observed, with the flow velocity to the right (away from the heater) near the surface of the fluid and in the lower part of the measured region, and to the left (towards the heater) in a stream about 2 cm below the free surface. The Reynolds number

Re is defined as $Re = \rho u \ell / \eta$, where ρ is the density of the fluid, η the viscosity, u the flow velocity, and ℓ a characteristic length scale, which we take here to be the depth of the tank. Re is the ratio of inertial to viscous forces in the flow. The average horizontal velocity in the region outlined by the small dotted rectangle in Figure 3.5 is 0.024 ± 0.016 cm/s; we take this as the value of u . Using approximate values of $\rho = 1000$ kg/m³ and $\eta = 0.001$ Pa s for water at room temperature, we estimate $Re \approx 33$ for this flow.

We can estimate the relative importance of convective and conductive contributions to the heat flux for this experiment using Eq. (3.1). We use the temperatures T_1 and T_2 measured by temperature probes 1 and 2, respectively, and the distance d between these two probes to estimate $\Delta T = T_2 - T_1 = 4.2$ K and $\nabla T = \Delta T / d = 245$ K/m. We used tabulated values for the physical properties of water at room temperature, so $D = 0.6$ W/m K and $C = 4200$ J/kg K. Eq. (3.1) then gives the magnitude of the total heat flux in the region between the first two temperature probes as approximately 4400 W/m², and the ratio r of the convective term in Eq. (3.1) to the conductive term is approximately

$$r = \frac{\rho C \Delta T \vec{u}}{D \nabla T} \approx 29. \quad (3.4)$$

In this case, the convective heat transport substantially dominates over conductive transport.

Figure 3.6 shows the velocity fields measured in two experiments on the HEC solution. Data from the first, shown in Figure 3.6(a), were obtained with the heater power adjusted so that the temperature difference ΔT between probes 1 and 2 at the time of the measurements was 10.8 K. The velocity field was calculated from images taken 18 s apart. As above, the measurements were made several minutes after the heater was turned on, but the system had not yet reached a steady state. This value of ΔT is within the range allowed in MRI scans. The flow field is much simpler than in Figure 3.5, with a single recirculating vortex visible in the field of view. The fluid flows upwards close to the heater, away from the heater in the upper few cm of the tank, and back towards the heater in the lower part of the tank. The averaged

horizontal velocity in the region within the dotted rectangle in Figure 3.6(a) is $(5.3 \pm 1.9) \times 10^{-4}$ cm/s. This is two orders of magnitude smaller than the velocity measured in water due to the much higher viscosity of the HEC solution, and the flow is perhaps not immediately noticeable to the naked eye in the absence of tracer particles. The probes were separated by 4.2 cm, giving $\nabla T = 260$ K/m. The thermodynamic properties of HEC solutions are not tabulated. Since our solutions are 97% water, we assume that ρ , D , and C are the same as for water. Using the zero-shear-rate viscosity of the HEC solution measured above, we estimate Re for this flow to be approximately 6×10^{-6} . From Eq. (3.1), the total heat flux between probes 1 and 2 is estimated to be $j = 390$ W/m², which is again much smaller than that for the water experiment. Despite the fact that the viscosity of the phantom material substantially reduces the flow velocity, the convective contribution to the heat flux is approximately equal to the conductive contribution: For the flow field plotted in Figure 3.6(a), $r \approx 1.6$.

Figure 3.6(b) shows the velocity field in the HEC solution under stronger heating. In this case images were recorded every 2 s, $\Delta T = 49$ K, and $Re \approx 7 \times 10^{-5}$. The flow field is qualitatively similar to that shown in Figure 3.6(a), but the thermally-driven convective flow and heat flux are correspondingly stronger. The averaged horizontal flow velocity in the indicated region is $(2.8 \pm 0.1) \times 10^{-3}$ cm/s and $r \approx 6.1$.

The three experimental situations discussed above were simulated using Comsol, as described in Sec. 3.2. Since the experiments were not performed in steady state, we carried out time-dependent simulations. We compared our experimental data to simulations at times for which the temperatures measured by our fiber-optic probes agreed well with those calculated in the simulations. The results are presented in Figure 3.7 and Table 3.1.

Simulations for water are shown in the top row (Figure 3.7(a)-(c)), for HEC with the lower heating power in the middle row (Fig 3.7(d)-(f)), and for HEC solution with the higher heating power in the bottom row (Figure 3.7(g)-(i)). The first column of Figure 3.7 shows vector plots of the simulated flow field in the entire tank; the middle column shows the same data in the upper left corner of the tank, corresponding to the region in which the flow field was measured

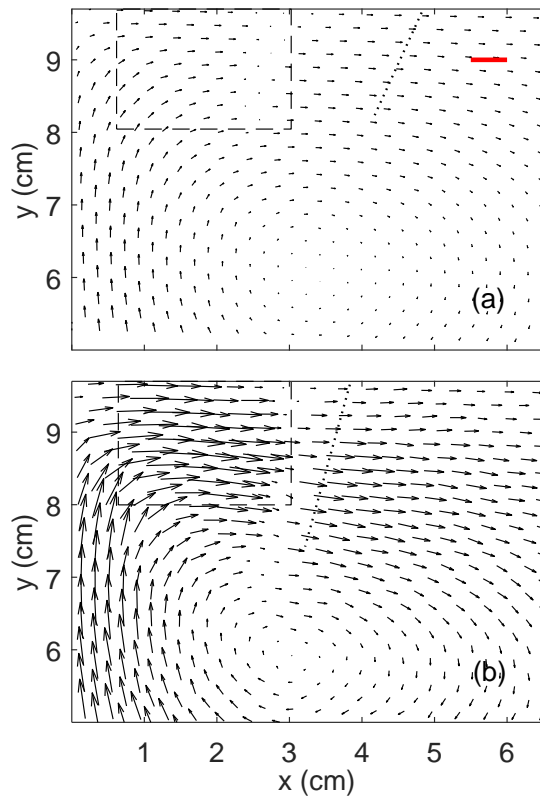


Figure 3.6: The velocity field in experiments on the HEC solution. (a) shows the velocity field when the temperature difference between probes 1 and 2 was 10.8 K; (b) is for a temperature difference of 49 K. The field of view is at the top left of the fluid, in a vertical plane through the center of the tank, as discussed in the text. The edge of the heater is at $x = 0$; the bottom of the tank is at $y = 0$, and the free surface of the fluid is at the top of the image. The tip of temperature probe 1 is close to the heater, and the dotted line shows the approximate position of temperature probe 2. The length of the scale bar at the top right of (a) corresponds to a velocity of 3×10^{-3} cm/s.

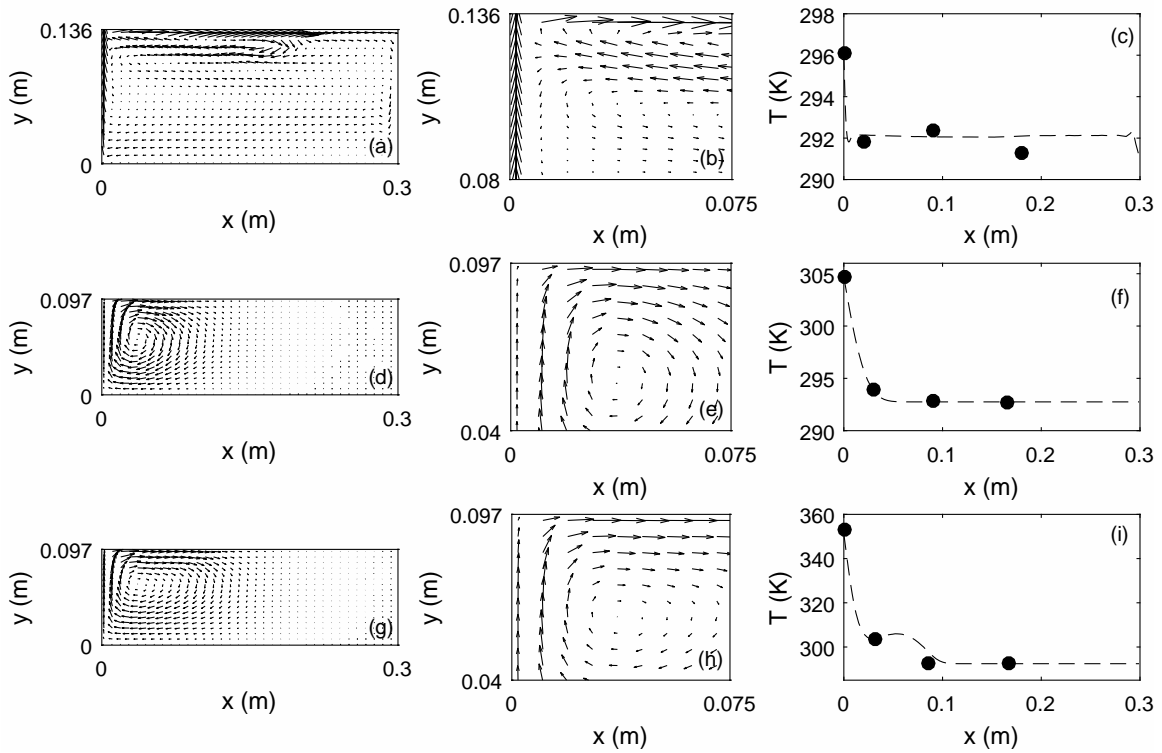


Figure 3.7: Simulations of the flow and temperature fields for the three experiments described in the text. (a)-(c): Water, $T_1 = 295.9$ K; (d)-(f): HEC solution, $T_1 = 304.7$ K, (g)-(i): HEC solution, $T_1 = 352.8$ K. The left-hand column shows the velocity field in the entire simulated domain, which models the tank used in the experiments. The center column shows the velocity field in the upper left corner of the domain. This corresponds to the region in which the velocity was measured experimentally, as shown in Figs. 3.5 and 3.6. The right-hand column shows the temperatures measured at the four probes as solid circles, and the simulated temperature at approximately the same depth as a dashed line.

experimentally; and finally, the third column shows the temperature as a function of horizontal position obtained from the simulations at a depth below the free surface roughly equal to the depth of the temperature probes, compared with the actual temperature measured by those probes. Overall, the numerical simulations are in good qualitative, and reasonable quantitative, agreement with the experimental data.

The simulation data for water shown in Figure 3.7(a)-(c) are for a time 10 min after the beginning of the simulation. Despite the complexity of the flow, there is reasonable qualitative agreement with the measured flow pattern, as can be seen by comparing Figure 3.7(b) with the experimental results shown in Figure 3.5. There is a strong flow away from the heater close to the surface of the fluid, inflow a few cm below the surface, and a weaker outflow near the bottom of the figure. The simulated temperatures 4 cm below the free surface are compared with experimental data in Figure 3.7(c) also agree reasonably well; the differences are in part due to the fact that the temperature probes were not all positioned at the same depth in the fluid. The x -component of the simulated flow velocity at a point corresponding approximately to the dashed rectangle in Figure 3.5 is in very good agreement with the value estimated from the experiments, as is the simulated total heat flux. The ratio of convective to conductive heat transport is larger in the simulations than estimated experimentally, but given the complexity of the flow, the approximations involved in estimating the experimental heat flux, and the fact that the simulations were two-dimensional, the level of agreement between experiment and simulation is satisfactory.

The flows in HEC are substantially simpler, reflecting their much lower Reynolds number, and consist of one large vortex that occupies most of the tank. As time progresses in the simulations, the large vortex expands to the right, eventually filling the tank. The simulated flow patterns shown in Figure 3.7(d) and (e) for HEC with the lower heat input are for a time 15 min from the start of the simulation, and agree very well with the measured flow field shown in Figure 3.6(a). The simulated temperature field plotted in Figure 3.7(f), corresponding to a depth of 2 cm, also shows excellent agreement with the measured temperature data. In this

Table 3.1: Comparison of simulated and experimentally determined heat transport.

		v_x (cm/s)	j (W/m ²)	r
water	expt.	$(2.4 \pm 1.6) \times 10^{-2}$	4.4×10^3	29
	sim.	2.3×10^{-2}	4.7×10^3	280
HEC, low power	expt.	$(5.3 \pm 1.9) \times 10^{-4}$	3.9×10^2	1.6
	sim.	8.8×10^{-4}	4.2×10^2	0.9
HEC, high power	expt.	$(2.8 \pm 1.1) \times 10^{-3}$	5.9×10^3	6.1
	sim.	4.9×10^{-3}	5.6×10^3	5.8

case, the simulated velocity in the rectangular reference area is slightly larger than estimated from the experiments, but the simulated and experimental values for the total heat transport are in reasonable agreement. The simulations indicate that the convective contribution to the heat transport is roughly equal to the conductive contribution, as in the experiment. The data in Figure 3.7(g)-(i) for HEC with the higher heat input are similarly for a time of 15 min, and again show semi-quantitative agreement with the experimental results. In particular, the ratio of convective to conductive heat transport in this case is roughly 6 for both experiment and simulation.

3.4 Discussion and Conclusion

We have measured the rheological properties of a saline solution of hydroxyethyl cellulose that is commonly used as a tissue phantom in the testing of MRI devices. This material behaves as a typical entangled polymer solution. It has no yield stress and is shear thinning, with the shear-rate-dependence of the viscosity being well-described by the Cross model. The viscoelastic moduli obey time-temperature superposition, with the expected temperature dependence. Our rheological data are consistent with previous results on HEC solutions [21].

The viscosity of the HEC solution is roughly four orders of magnitude higher than that of water. As a result, the convective flow velocity resulting from a horizontal temperature gradient is very small. Nonetheless, the results of our flow-visualization experiments show clearly that the convective contribution to heat transport in this material is of the same order of magnitude

as the conductive contribution for quite modest local temperature differences. This conclusion is reinforced by numerical simulations.

The HEC saline solution recommended for use as a phantom in MRI device tests is referred to in [14] as a “slurry,” despite the fact that it contains no insoluble component, and a “gelled saline,” despite the fact that it is not gelled. This is not just an issue of semantics: both slurries and gels would be expected to have a yield stress. In contrast, our results demonstrate conclusively that the HEC solution has no yield stress, but rather behaves as a typical viscoelastic polymer solution. As a result, it flows in response to an arbitrarily small horizontal temperature gradient, resulting in a convective contribution to heat transport in the fluid. For temperature gradients that are typical of those observed in MRI tests, our results show that, although the flow velocity in the fluid is only on the order of $\mu\text{m/s}$, the convective heat transport in this fluid can easily be significant.

Phantoms used in MRI device testing should ideally mimic the thermal, mechanical, and electrical properties of human tissue. This is, of course, a difficult requirement to meet, and indeed different types of tissue have different properties. Phantom materials should also be straightforward to prepare, safe to handle, and store well. The HEC saline solution described in [14] meets many of these requirements. Nonetheless, we have shown that it flows, and so transports heat convectively, under MRI test conditions, while tissue does not.

A primary reason for testing medical devices for use within MRI systems is to ensure patient safety. It is important that a patient implanted with the device will not be injured by an increase in device temperature due to eddy-current heating while in the MR scanner. In this context, it is crucial that the tests be conservative and that they be fully characterized and understood. Any heating measured in a phantom under test conditions should be greater than that expected in a patient under worst-case clinical conditions. If a significant fraction of the heat produced by eddy-current heating is carried away from the device by convective flow of the phantom material, this must be recognized and accounted for when evaluating the safety margins associated with those tests. In ASTM F2182-11a, it is stated that the phantom

viscosity should be such that “the phantom material does not allow bulk transport or convection currents.” The standard then goes on to state (Sect. 8.3) that either PAA or HEC gelled salines are “suitable.” This suggests that convection currents will be negligible when using these materials, when in fact we have shown that is not the case. We have shown that convection can have a cooling effect on a device similar to that of conduction alone. While these gelled salines are practical materials for this application, our results make it clear that one cannot assume that convective heat transport is absent.

The contribution of convection to heat transport in gelled salines such as HEC may be particularly relevant when comparing computer simulations of device heating to experimental tests [22]. Currently, computer simulations of device heating typically only include conduction. Based on our results, they would thus appear to underestimate cooling effects, potentially by a factor as high as 2-6. Proper validation of computer simulations is a critical component of medical device testing efforts, and this is clearly a factor that should be included in these efforts.

There exist many other polymer-based materials that have a true yield stress. Such viscoplastic materials do not flow when subjected to shear stress lower than the yield stress, but rather behave as a soft elastic solid. This class of materials would seem to be well suited for use as tissue phantoms in MRI testing applications, and we will explore this possibility in future work.

Bibliography

- [1] C. Westbrook and C. K. Roth. *MRI in practice*. Wiley-Blackwell, Oxford, 2011.
- [2] F. G. Shellock and J. V. Crues, editors. *MRI: Bioeffects, safety, and patient management*. Biomedical Research Publishing Group, Playa Del Rey, 2014.
- [3] T. O. Woods. Standards for medical devices in MRI: Present and future. *Journal of Magnetic Resonance Imaging*, 31:1186–1189, 2013.
- [4] W. Kainz, G. Neubauer, R. Überbacher, F. Alesch, and D. D. Chan. Temperature measurement on neurological pulse generators during MR scans. *BioMedical Engineering OnLine*, 1:2, 2002.
- [5] K. Yoshimura, H. Kato, M. Kuroda, A. Yoshida, A. Hanamoto, A. Tanaka, M. Tsunoda, S. Kanazawa, K. Shibuya, S. Kawasaki, and Y. Hiraki. Development of a tissue-equivalent MRI phantom using carrageenan gel. *Journal of Magnetic Resonance Imaging*, 50:1011–1017, 2003.
- [6] Y. Ikemoto, T. Wataru, K. Yoshitomi, S. Ohno, T. Harimoto, S. Kanazawa, K. Shibuya, M. Kuroda, and H. Kato. Development of a human-tissue-like phantom for 3.0-T MRI. *Medical Physics Journal*, 38:6336–6342, 2011.
- [7] G. D. Waiter and M. A. Foster. Lanthanide-edta doped agarose gels for use in NMR imaging phantoms. *Journal of Magnetic Resonance Imaging*, 15:929–938, 1997.
- [8] W. D. D’Souza, E. L. Madsen, O. Unal, K. K. Vigen, G. R. Frank, and B. R. Thomadsen. Tissue mimicking materials for a multi-imaging modality prostate phantom. *Medical Physics Journal*, 28:688–700, 2001.
- [9] A. R. Rezai, D. Finelli, J. A. Nyenhuis, G. Hrdlicka, J. Tkach, A. Sharan, P. Rugieri, P. H. Stypulkowski, and F. G. Shellock. Neurostimulation systems for deep brain stimulation:

- In vitro evaluation of magnetic resonance imaging-related heating at 1.5 Tesla. *J. Magn. Reson. Imaging*, 15:241–250, 2002.
- [10] S. M. Park, J. A. Nyenhuis, C. D. Smith, E. J. Lim, K. S. Foster, K. B. Baker, G. Hrdlicka, A. R. Rezai, P. Ruggieri, A. Sharan, F. G. Shellock, P. H. Stypulkowski, and Tkach J. Gelled versus nongelled phantom material for measurement of MRI-induced temperature increases with bioimplants. *IEEE Trans. Magn.*, 39:3367–3371, 2003.
- [11] K. R. Gorny, M. F. Presti, S. J. Goerss, S. C. Hwang, D.-P. Jang, I. Kim, H.-K. Min, Y. Shu, C. P. Favazza, K. H. Lee, and M. A. Bernstein. Measurements of RF heating during 3.0-T MRI of a pig implanted with deep brain stimulator. *Magn. Reson. Imaging*, 31:783–788, 2013.
- [12] G. Hartsgrove, A. Kraszewski, and A. Surowiec. Simulated biological materials for electromagnetic radiation absorption studies. *Bioelectromagnetics*, 8:29–36, 1987.
- [13] U. D. Nguyen, J. S. Brown, I. A. Chang, J. Krycia, and M. S. Mirotznik. Numerical evaluation of heating of the human head due to magnetic resonance imaging. *IEEE Trans. Biomed. Eng.*, 51:1301–1309, 1987.
- [14] ASTM. *F2182-11a: Standard Test Method for Measurement of Radio Frequency Induced Heating On or Near Passive Implants During Magnetic Resonance Imaging*. ASTM International, 2011.
- [15] A. Bejan, editor. *Convection Heat Transfer*. Wiley, New York, 1995.
- [16] A Dabbagh, B. J. J. Abdullah, C. Ramasindarum, and N. H. A. Kasim. Tissue-mimicking gel phantoms for thermal therapy studies. *Ultrasonic Imaging*, 36:291–316, 2014.
- [17] P. Ehses, F. Fidler, P. Nordbeck, E. D. Pracht, M. Warmuth, P. M. Jakob, and W. R. Bauer. MRI thermometry: Fast mapping of RF-induced heating along conductive wires. *Journal of Magnetic Resonance Imaging*, 60:457–461, 2008.

- [18] K. Sveen. An introduction to matpiv v. 1.6.1. <http://www.mn.uio.no/math/english/people/aca/jks/matpiv/>, 2004.
- [19] C. W. Macosko. *Rheology: principles, measurements, and applications*. Wiley-VCH, New York, 1994.
- [20] R. G. Larson. *The structure and rheology of complex fluids*. Oxford University Press, New York, 1999.
- [21] N. Arfin and H. B. Bohidar. Concentration selective hydration and phase states of hydroxyethyl cellulose (HEC) in aqueous solutions. *International Journal of Biological Macromolecules*, 50:759–767, 2012.
- [22] C. D. Smith, A. V. Kildishev, J. A. Nyenhuis, K. S. Foster, and J. D. Bourland. Interactions of magnetic resonance imaging radio frequency magnetic fields with elongated medical implants. *Journal of Applied Physics*, 87:6188–6190, 2000.

Chapter 4

Start-up flow of a yield-stress fluid in a vertical pipe

4.1 Introduction

The startup of flow in a fluid initially at rest has been of interest for many years. Stokes solved the problem of a fluid driven by an impulsively-started plate in [1]. The pressure-driven startup of a Newtonian fluid in a circular pipe was studied by Szymansky et al. [2]; full solutions can be found in [3, 4].

The transient startup flow in non-Newtonian fluids is less well-understood. In this paper, we study the startup of Carbopol, a polymer microgel that is commonly used as a model yield-stress fluid. Yield-stress fluids behave as soft solids when the shear stress is below the yield stress τ_y , but flow when the stress is greater than τ_y [5]. Yield-stress fluids have important applications in the food industry, personal care products, and geological flows. Waxy crude oil has a yield stress, and the restart of waxy crude oil in pipelines is an important issue in oil recovery [6, 7]. In the Newtonian case, the startup flow is governed by viscosity. In the case of Carbopol and other yield-stress fluids, elasticity and the yield stress must also play a role.

Carbopol is a nearly-ideal yield-stress fluid with minimal thixotropy [8, 9]. The yielding

transition in Carbopol and the transient flow at startup have been studied in both controlled strain and controlled stress experiments by Divoux and co-workers [10, 11, 12, 13]. They used a combination of rheometry and spatially resolved ultrasonic velocimetry in Couette (concentric cylinder) and parallel-plate geometries. Under an imposed stress and with rough boundaries, they observed that the yielding transition was spatially heterogeneous and proceeded through several stages: an initial slow creep deformation, followed by the appearance of wall slip, then shear banding, before the Carbopol eventually reached a fully fluidized steady state in which the wall slip velocity went to zero. The duration of the transient flow increased as the applied stress approached τ_y from above [11]. A similar scenario, but with no initial creep stage, was observed in controlled rate experiments [12].

Much of the research on startup flows in yield-stress fluids has been motivated by waxy crude oil [14, 15, 16]. Waxy crude oil has a very complex rheological behavior [17, 15, 14, 18, 19, 20]. In particular, it can cool while being transported from the reservoir in a pipeline, causing wax precipitation and the formation of a gel-like structure that gives it a yield stress. Following a stoppage, flow is typically restarted by injection of a Newtonian fluid which displaces the gelled oil. Doing this safely and effectively requires an understanding of the effect of yield stress on startup.

The startup flow of a fluid described by the Bingham model—which includes the yield stress but not elasticity—in a circular pipe has been found analytically [21]. Several numerical models of startup flow in yield-stress fluids in pipelines have been presented, using models and methods of varying complexity, incorporating compressibility and elasticity [15, 22, 23, 24, 25, 26, 27, 28, 29]. Experimental studies using model fluids have also been published. Lee et al. used rheometry and a model pipeline to study the breakup of a model wax-oil mixture in [30]. The solid-fluid transition in Carbopol was studied using rheometry in [9]. Dimitriou et al. investigated steady state and startup flow in a model wax-oil system using rheometry and particle image velocimetry [31]. Unsteady flow of Carbopol in capillary tubes was investigated in [32]. Sierra et al. studied the pressure required to restart the flow of Carbopol in a horizontal

pipe [16]. Several models of yield stress fluids based on a structure parameter that describes the state of the materials have been described, as reviewed in [33]. In particular, in this paper we make use of an elasto-viscoplastic model, introduced by de Souza Mendes [34, 35].

In this chapter, we investigate the startup flow of Carbopol in vertically-oriented cylindrical pipes with both rough and smooth boundary conditions. A more dense, immiscible Newtonian fluid was injected into the bottom of the pipe, increasing the pressure on the Carbopol and eventually displacing it and causing it to yield. We measured the pressure in the Carbopol, and used particle image velocimetry (PIV) to study the transient flow field within the Carbopol. For rough boundary conditions, our results are consistent with the yielding process described in [11]: we observed elastic deformation, followed by wall slip and full yielding. The transient flow field in the Carbopol was roughly parabolic at early times, approaching the expected plug flow as the system approached a steady state. For smooth walls, the Carbopol moved through the pipe due to wall slip, but full yielding was not observed.

4.2 Experiment

4.2.1 Fluid preparation

The fluids used in this work are solutions of Carbopol 940 (Lubrizol) with concentrations of 0.13, 0.18 and 0.5 wt%. Carbopol is widely used as a model yield-stress fluid [36, 37]. It is a nearly ideal viscoplastic fluid with very weak thixotropy and stable properties [38]. It consists of polydisperse cross-linked particles of polyacrylic acid and has a $pH \approx 3$ when initially dissolved in water. When the resulting solution is neutralized by addition of NaOH, the particles swell and jam together, forming a micro-gel network structure that gives the fluid a yield stress [39, 40].

The Carbopol was prepared as follows [41]. Dry Carbopol powder was dispersed into 500 ml deionized water at room temperature while stirring with a commercial mixer (Arrow Engineering 1750) until it was completely dissolved. NaOH solution with concentration 40.0

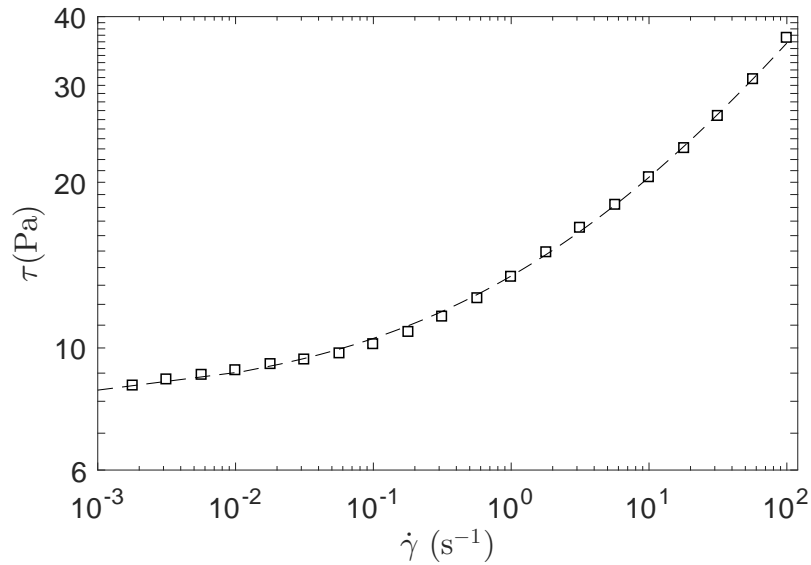


Figure 4.1: The shear stress τ as a function of shear rate $\dot{\gamma}$ of 0.13 wt% Carbopol containing 0.6 vol% glass beads. Symbols are the measured data, and the dashed line is a fit to the Herschel-Bulkley model, as described in the text.

mg/ml was added to raise the pH to 6. The pH was monitored with a Beckman 300 series pH meter. The stirring was continued for 12 hours to ensure that the gel was homogeneous. Glass beads with a diameter $420 \mu\text{m}$ and a density 2.5 g/cm^3 were mixed into the Carbopol with a volume fraction of approximately 0.006. These beads were used as tracers for visualizing the flow field in our experiments, as described below. The density ρ of the Carbopol seeded with glass beads was $1050 \pm 10 \text{ kg/m}^3$ for all three concentrations.

4.2.2 Rheological characterization

An Anton Paar MCR302 rheometer was used to measure the rheological properties of the Carbopol seeded with glass beads. We used a cone-plate geometry with a 50 mm diameter and 4° cone angle. Sandpaper with a roughness of $50 \mu\text{m}$ was affixed to the rheometer tool to minimize wall slip. An environmental housing surrounding the tool minimized evaporation of the sample during the measurements. Fig. 4.1 shows a flow curve for 0.13 wt% Carbopol

Table 4.1: Yield stress and Herschel-Bulkley model parameters for the Carbopol gels containing glass beads used in this work.

c (wt%)	τ_y (Pa)	n	k (Pa s n)
0.13	7.9±0.1	0.347±0.009	5.6±0.2
0.18	40.5±0.6	0.32±0.08	20.7±0.8
0.5	79±1	0.324±0.006	44±1

containing 0.6 vol% glass beads measured by increasing the imposed shear rate $\dot{\gamma}$ in steps and measuring the shear stress τ . Measurements were carried out at a temperature of 20.00±0.01 °C. The waiting time at each step ranged from 10 mins at the lowest shear rate to 30 s at the highest. The Herschel-Bulkley (HB) model, $\tau = \tau_y + k\dot{\gamma}^n$, was fitted to the data to determine the yield stress τ_y , flow index n , and consistency k . The fit parameters obtained for the three Carbopol solutions used in this work are shown in Table 4.1.

4.2.3 Experimental setup

Our experiments were carried out using the apparatus shown schematically in Fig. 4.2. A Plexiglas pipe 50.0 cm in height and 5.67 cm in inner diameter was mounted vertically. Two different pipes were used, with different boundary conditions. One had untreated walls with a surface roughness of approximately 0.15 μm . The other had 50 μm -grit sandpaper glued to the inner wall to give a rough surface, leaving a transparent region at the bottom of the pipe for visualization. The top of the pipe was open. The bottom was connected by a 3 mm diameter plastic tube to a reservoir sealed with a piston. The pipe was partly filled with Carbopol poured carefully in from above. The reservoir contained a Newtonian liquid, Fluorinert FC-40 (3M). Fluorinert has a density of 1855 kg/m 3 and is immiscible with Carbopol (and water). A motorized actuator drove the piston at a constant, controllable rate, causing the Fluorinert to enter the bottom of the pipe and displace the Carbopol. After injecting a small volume of Fluorinert into the pipe, we waited for one week to allow the number of bubbles in the Carbopol to decrease before starting our experiments. The rate at which Carbopol was displaced by the Fluorinert was controlled by the speed of the piston. We characterized this

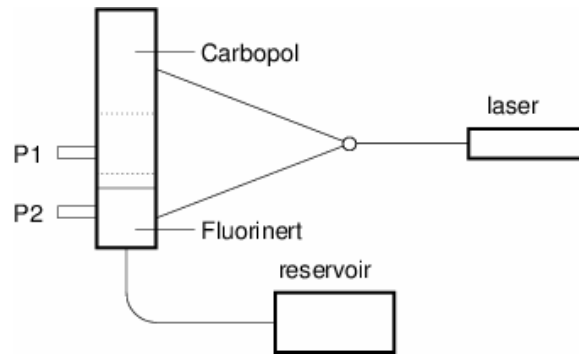


Figure 4.2: A schematic diagram of the experimental apparatus. P_1 and P_2 are pressure gauges. The solid horizontal line near the bottom of the pipe is the interface between the Carbopol and Fluorinert. The area between the dotted lines is the region used for flow visualization.

by the volumetric flow rate Q_l , calculated by integrating the measured velocity field over the cross-section of the pipe when the flow had reached a steady state.

Particle Image Velocimetry (PIV) was used to measure the velocity field in the Carbopol. The beam from a 633 nm, 12 mW HeNe laser (Research Electro-Optics) was reshaped into a vertical light sheet by a cylindrical lens, as shown in Fig. 4.2. The light sheet passed through the center of the pipe, where laser light scattered from the flow visualization particles suspended in the Carbopol. A ccd camera (Pulnix) controlled by a LabView program (National Instruments) recorded images of the illuminated particles at 1 s intervals. The field of view was 5.82×4.46 cm², and the spatial resolution of the camera was 11 pixels per mm. Two-dimensional velocity fields in this region were calculated from the recorded images using the MatPIV software package [42].

Two electronic pressure gauges (Omegadyne PX309) were mounted in the wall of the pipe, as shown in Fig. 4.2. Pressure gauge P_1 is located above the Carbopol-Fluorinert interface, in the Carbopol, while P_2 is located below the interface, in the Fluorinert. The wall shear stress at the location of P_1 is given by

$$\tau_w = \frac{R(\Delta P - \rho g L)}{2L}, \quad (4.1)$$

where $\Delta P = P_1 - P_0$ is the difference between the pressure P_1 measured by the gauge and the atmospheric pressure P_0 . ρ is the density of Carbopol, g the gravitational acceleration, and L the height of the Carbopol column above the gauge. P_1 changes as the Fluorinert is injected into the pipe, and L changes as the Carbopol is displaced, so τ_w is thus a function of time.

4.3 Results

We first present results from an experiment using 0.18 wt% Carbopol in the rough-walled pipe with a very low displacement rate, $Q_l = 5.02 \times 10^{-8} \text{ m}^3/\text{s}$. P_1 and the wall shear stress τ_w , calculated using Eq. (4.1), are plotted in Fig. 4.3. In this experiment, injection of the Fluorinert started at time $t = 90 \text{ s}$, at which time P_1 and τ_w started to increase. Around $t = 200 \text{ s}$, the rate of increase began to slow. Although P_1 continued to increase slowly, τ_w reached a plateau at a value slightly higher than the yield stress of the Carbopol. The dashed lines in Fig. 4.3(a) are linear fits to $P_1(t)$ for $160 \text{ s} \leq t \leq 200 \text{ s}$ and $300 \text{ s} \leq t \leq 400 \text{ s}$. These lines cross at a time t^* . We refer the value of τ_w at t^* as τ_w^* . In this experiment, $\tau_w^* = 47 \pm 2 \text{ Pa}$, slightly larger than the yield stress, $\tau_y = 40.5 \pm 0.6 \text{ Pa}$.

Fig. 4.4 shows profiles of the net velocity $v - v_s$ as a function of radial position r , averaged over the three time intervals marked by rectangles in Fig. 4.3(b). Here v is the velocity determined from the PIV data and v_s is the slip velocity at the wall of the pipe, determined from a linear fit to $v(r)$ near the wall. During the time interval labeled 1 on Fig. 4.3, when τ_w was increasing, the velocity profile was approximately parabolic. In interval 2, when the slope of τ_w started to decrease, the value of $v - v_s$ at the center of the pipe reached its maximum. The velocity profile at this time was still roughly parabolic. Finally, in time interval 3, when τ_w had reached its plateau value, the velocity was roughly constant in the central portion of the pipe and the velocity profile appeared to be approaching the plug-flow profile predicted by the HB

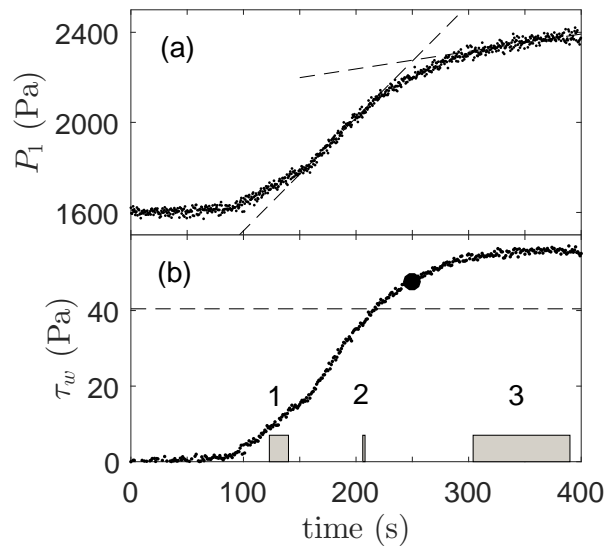


Figure 4.3: Data from an experiment using 0.18 wt% Carbopol in the rough-walled pipe with a very slow displacement rate, $Q_l = 5.02 \times 10^{-8} \text{ m}^3/\text{s}$. (a) P_1 , the pressure in the Carbopol. The dashed lines are linear fits to $P_1(t)$ at early (160-200 s) and late times (300-400 s). The time at which the two fits intersect is t^* . (b) τ_w , the wall shear stress, calculated from Eq. (4.1). The black circle is τ_w^* , the wall shear stress at t^* . The dashed line is the yield stress measured with the rheometer. The three time intervals discussed in the text and in Fig. 4.4 are shown by the grey rectangles. The uncertainty of τ_w is approximately the size of the symbols.

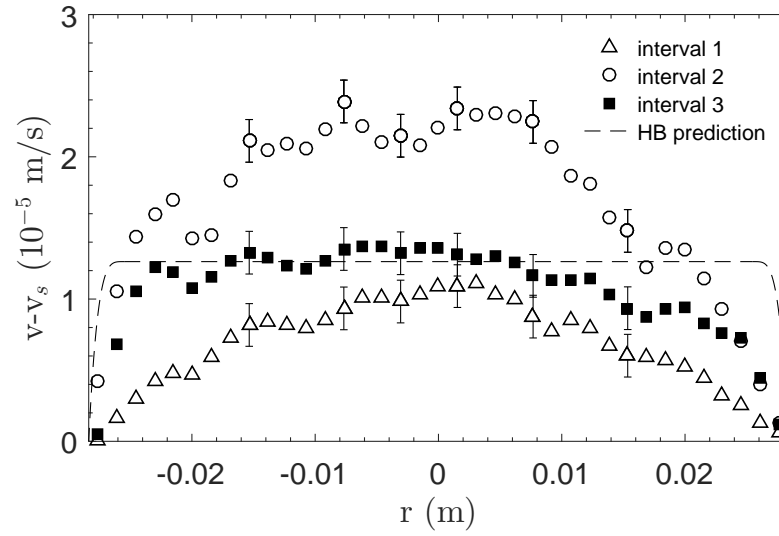


Figure 4.4: The flow velocity $v(r)$ corrected for the slip velocity v_s for the same experiment as in Fig. 4.3. The r axis spans the full diameter of the pipe. The dashed line is the steady-state velocity profile predicted by the HB model.

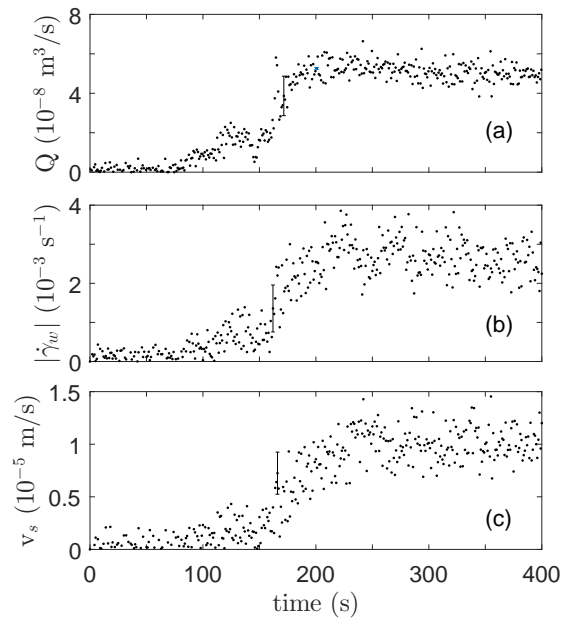


Figure 4.5: Additional results for the experiment shown in Fig. 4.3. (a) Q , the volumetric flow rate. (b) $|\dot{\gamma}_w|$, the absolute value of the wall shear rate. (c) v_s , the slip velocity.

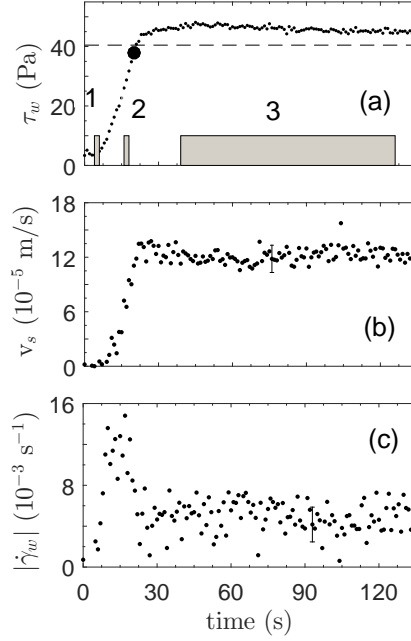


Figure 4.6: Data from an experiment using 0.18 wt% Carbopol in the rough-walled pipe with a displacement rate of $Q_l = 3.41 \times 10^{-7} \text{ m}^3/\text{s}$. (a) τ_w , the wall shear stress. The dark circle is τ_w^* , and the dashed line is the yield stress. The rectangles indicate the three time intervals referred to in Fig. 4.7. The uncertainty of τ_w is approximately the size of the symbols. (b) v_s , the slip velocity. (c) $|\dot{\gamma}_w|$, the absolute value of the wall shear rate.

model [43]:

$$v - v_s = \begin{cases} \left(\frac{n}{n+1}\right) \left(\frac{\tau_w}{kR}\right) (R - R_p)^{\frac{1}{n}+1} & |r| < R_p; \\ \left(\frac{n}{n+1}\right) \left(\frac{\tau_w}{kR}\right) (R - R_p)^{\frac{1}{n}+1} \left[1 - \left(\frac{r-R_p}{R-R_p}\right)^{\frac{1}{n}+1}\right] & \text{otherwise.} \end{cases}$$

Here, R_p is the radius of the plug of the velocity profile, which is equal to $\frac{\tau_y R}{\tau_w}$. Fig. 4.5 shows the evolution of the volumetric flow rate Q , the absolute value of the wall shear rate $|\dot{\gamma}_w|$, determined from the slope of $v(r)$ near the wall, and the slip velocity v_s for the same experiment. Q and $|\dot{\gamma}_w|$ begin to increase when the injection of the Fluorinert starts. v_s begins to increase a short time later, as discussed below. All three quantities reach constant values, within the experimental scatter, at long times.

Fig. 4.6 shows data from an experiment with the same Carbopol solution in the rough-walled pipe, but with a higher displacement rate, $Q_l = 3.41 \times 10^{-7} \text{ m}^3/\text{s}$. As in the experiment

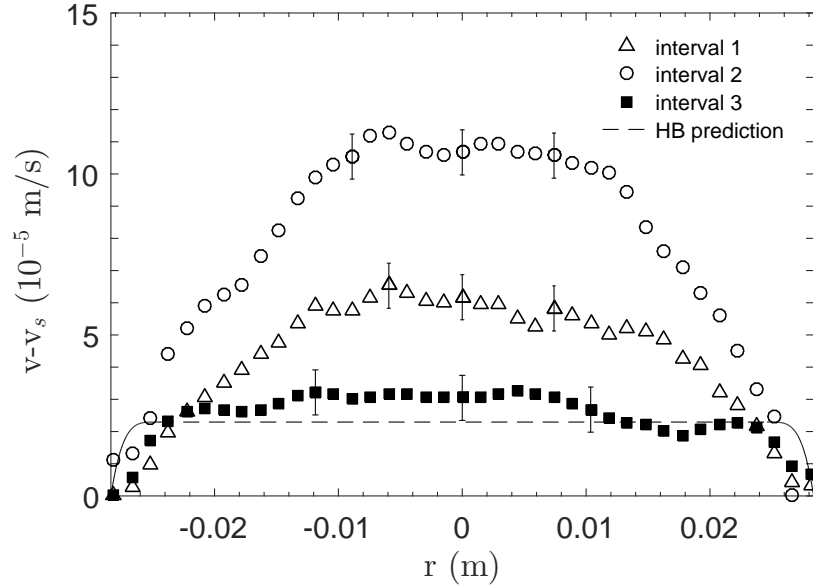


Figure 4.7: Velocity profiles for the same experiment as in Fig. 4.6. The dashed line is the velocity profile predicted by the HB model.

with low displacement rate, τ_w initially increased linearly, then approached a plateau which was slightly higher than τ_y . The value of τ_w^* at $t = t^*$ (black circle in Fig. 4.6(a)) is again close to τ_y , which is marked by the dashed line in Fig. 4.6(a).

Comparison of the two experiments shown in Figs. 4.3 and 4.6 shows that the time required for τ_w to reach its plateau value decreased as the displacement rate Q_l increased. Similarly, the slip velocity v_s increased more steeply and reached a higher value for the higher displacement rate. Interestingly, a peak was observed in the absolute value of the wall shear rate $|\dot{\gamma}_w|$ for the higher displacement rate (Fig. 4.6(c)), but not for the slow displacement rate (Fig. 4.5(b))

Fig. 4.7 shows the net velocity profiles for the experiment shown in Fig. 4.6. The general evolution of the flow field with time is similar to that seen in Fig. 4.4, but the flow profile observed at long times, when the wall stress had reached a steady value, was closer to that predicted by the HB model for the larger flow rate.

Data from two experiments in the smooth-walled pipe are shown in Fig. 4.8. The Carbopol concentration is again 0.18 wt%, and $Q_l = 5.02 \times 10^{-8} \text{ m}^3/\text{s}$ (left-hand graphs) and $5.49 \times 10^{-7} \text{ m}^3/\text{s}$ (right hand graphs). At the slower displacement rate, τ_w did not reach a plateau at long

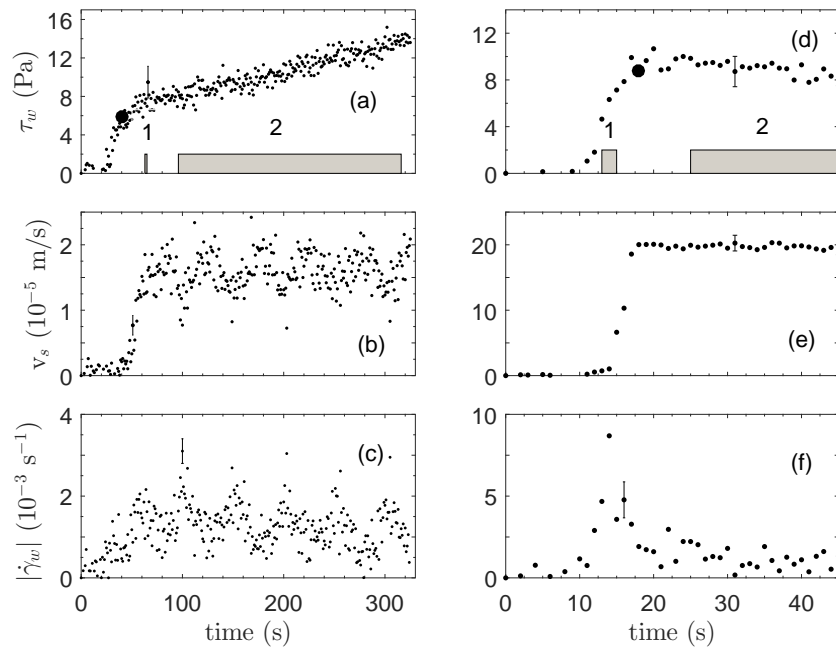


Figure 4.8: Results of two experiments with 0.18 wt% Carbopol in the smooth-walled pipe. (a), (b), and (c) are from an experiment with a low displacement rate, $Q_l = 5.02 \times 10^{-8} \text{ m}^3/\text{s}$. (a) τ_w , the wall shear stress. The black circle is τ_w^* . The two time intervals discussed in the text are shown by rectangles. (b) v_s , the slip velocity. (c) $|\dot{\gamma}_w|$, the absolute value of the wall shear rate. (d), (e), and (f) are the corresponding plots for an experiment with $Q_l = 5.49 \times 10^{-7} \text{ m}^3/\text{s}$.

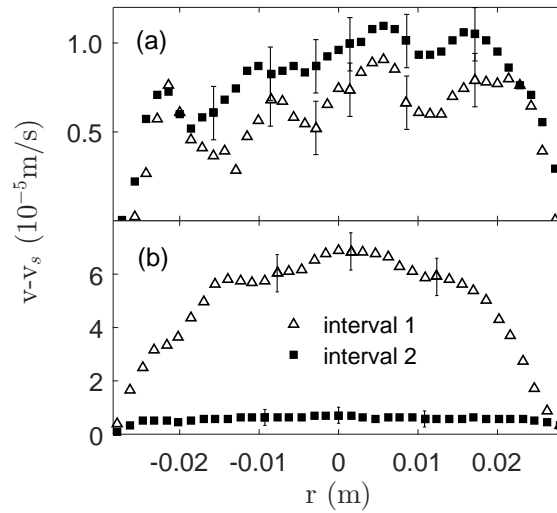


Figure 4.9: Velocity profiles, corrected for slip, for the two experiments shown in Fig. 4.8. (a) $Q_l = 5.02 \times 10^{-8}$ m³/s. (b) $Q_l = 5.49 \times 10^{-7}$ m³/s.

times, but rather continued to increase at a constant rate. τ_w^* , indicated by the black circle in Fig. 4.8(a), was much smaller than the yield stress, which was never exceeded over the whole experiment. This suggests that the observed fluid motion was a result of slip at the wall rather than yielding of the Carbopol. v_s and $|\dot{\gamma}_w|$ were also not constant at long times but varied roughly periodically in time, with the peaks of v_s coinciding with the troughs of $|\dot{\gamma}_w|$. This is suggestive of stick-slip motion at the walls of the tube [44].

At the higher displacement rate, shown in the right-hand graphs in Fig. 4.8, the wall shear stress initially increased, flattened out, then decreased slowly at long times. τ_w^* was again less than τ_y , as was the wall shear stress at long times. No periodic stick-slip behavior was observed in this experiment, but $|\dot{\gamma}_w|$ showed a clear peak before stabilizing at long times.

The velocity profiles measured in the two experiments plotted in Fig. 4.8 are shown in Fig. 4.9. The velocity profiles were averaged over the two time intervals indicated by rectangles in Fig. 4.8(a) and (d), respectively. For the lower displacement rate, $v(r) - v_s$ was roughly parabolic, but with large, persistent spatial deviations. The velocity profile showed no systematic time dependence, and in particular, did not approach plug-like flow at long times. At

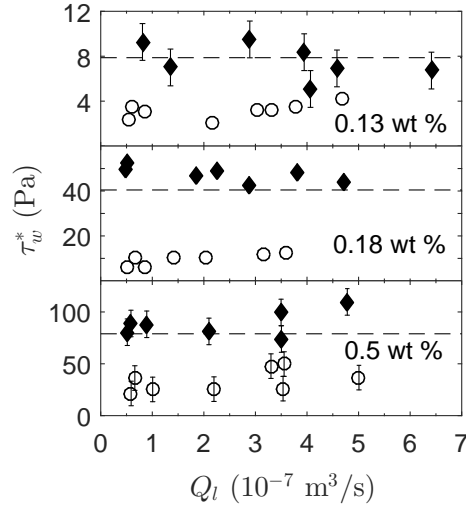


Figure 4.10: τ_w^* as a function of the displacement rate Q_l for three concentrations of Carbopol in both rough and smooth pipes. Solid diamonds: rough-walled pipe. Open circles: smooth-walled pipe. The horizontal dashed lines are the yield stress measured with the rheometer. When error bars are not shown, the uncertainties are approximately the size of the symbols.

the higher displacement rate, $v - v_s$ was maximal at time interval 1. The velocity profile was plug-like at long times, but since $\tau_w < \tau_y$, the HB model predicts no flow.

τ_w^* is plotted as a function of displacement rate Q_l in Fig. 4.10 for all three Carbopol concentrations in both rough and smooth pipes. For the rough-walled pipe, τ_w^* agrees with the yield stress within the experimental scatter, while in the smooth-walled pipe, τ_w^* is substantially lower than the yield stress and independent of flow rate.

Fig. 4.11 shows the wall shear stress $\tau_w(t)$ and slip velocity $v_s(t)$ at early times for two experiments. For 0.13 wt% Carbopol in the rough-walled pipe (Fig. 4.11(a)), the slip velocity started to increase from zero at the same time as the wall stress, when injection of the Fluorinert started. In contrast, for 0.18 wt% Carbopol in the smooth-walled pipe (and for all other experiments) (Fig. 4.11(b)), the slip velocity remained close to zero until the wall stress reached a threshold value τ_s . For 0.13 wt% Carbopol, $\tau_s = 0$ Pa in the rough-walled pipe and 1.0 ± 0.1 Pa in the smooth-walled pipe, while for 0.5 wt% Carbopol, $\tau_s = 58 \pm 2$ and 15 ± 2 Pa for rough

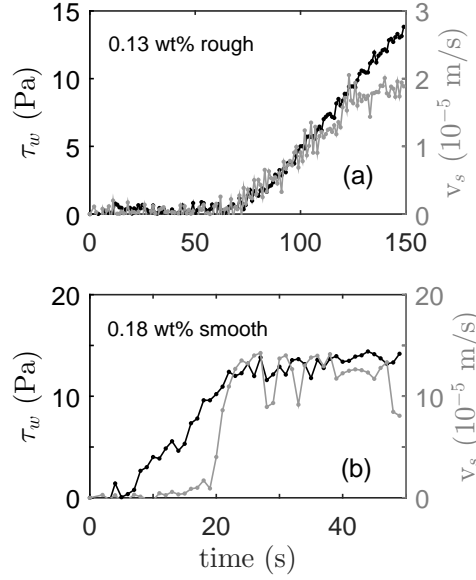


Figure 4.11: Wall shear stress τ_w (black dots and line) and slip velocity v_s (grey dots and line) as a function of time for (a) 0.13 wt% Carbopol in the rough-walled pipe and (b) 0.18 wt% Carbopol in the smooth-walled pipe.

and smooth walls, respectively. τ_s increased with Carbopol concentration, and, except for the lowest concentration, was higher for rough walls than for smooth.

4.4 Numerical simulation

A numerical model developed by de Souza Mendes and Thompson to describe elastoviscoplastic materials with thixotropy [35] was used to simulate our experiments. This model consists of two coupled differential equations, one relating shear stress to shear rate and one describing the evolution of a structure parameter λ . $\lambda = 0$ represents the fully unstructured state while $\lambda = \infty$ represents the fully structured state. The elastic and viscous moduli are functions of λ . The full model is described in the Appendix and in [35]. We simulated 0.5 wt% Carbopol in a cylindrical geometry with no slip at the wall, subject to an applied wall stress that varied sigmoidally in time, $\tau_w(t) = A(1 + B \exp(-Ct))^{-1}$, to mimic the experimental situation. Here,

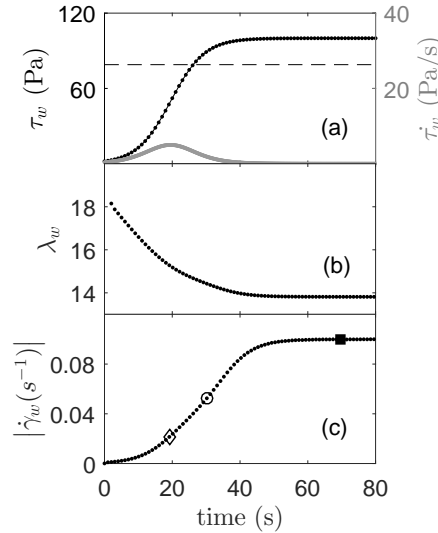


Figure 4.12: Results from a simulation of a slow displacement. (a) The imposed wall shear stress τ_w (black dots) and its time derivative $\dot{\tau}_w$ (grey dots) as a function of time. The dashed line is the yield stress. (b) $\lambda_w(t)$, the structure parameter at the wall of the pipe. (c) $|\dot{\gamma}_w|(t)$, the absolute value of the wall shear rate. The symbols indicate the times corresponding to the velocity profiles plotted in Fig. 4.13 .

A is the asymptotic value of τ_w at long times, B is a constant and C controls the rate at which τ_w approaches its long-time value.

We choose $A = 100$ Pa, slightly greater than the yield stress of the 0.5 wt% Carbopol solution given in Table 4.1, and $B = 50$. To model a slow displacement, we took $C = 0.2$ s⁻¹. Results from this simulation are shown in Fig. 4.12. λ_w , the structure parameter at the wall of pipe, decreases rapidly when the stress is first applied, indicating that the Carbopol near the wall destructures. The wall shear rate roughly follows the applied stress, approaching a plateau at long times, consistent with the experimental results for the slow displacement rate shown in Fig. 4.5(b). Velocity profiles from this simulation are shown in Fig. 4.13. v is approximately parabolic at early times, then evolves to a plug flow at long times. The evolution of the velocity profile coincides well with what is seen experimentally (Fig. 4.4).

We modeled a faster displacement using the same values of A and B , and $C = 1.5$ s⁻¹. Results from this simulation are shown in Figs. 4.14 and 4.15. Because τ_w increases more quickly,

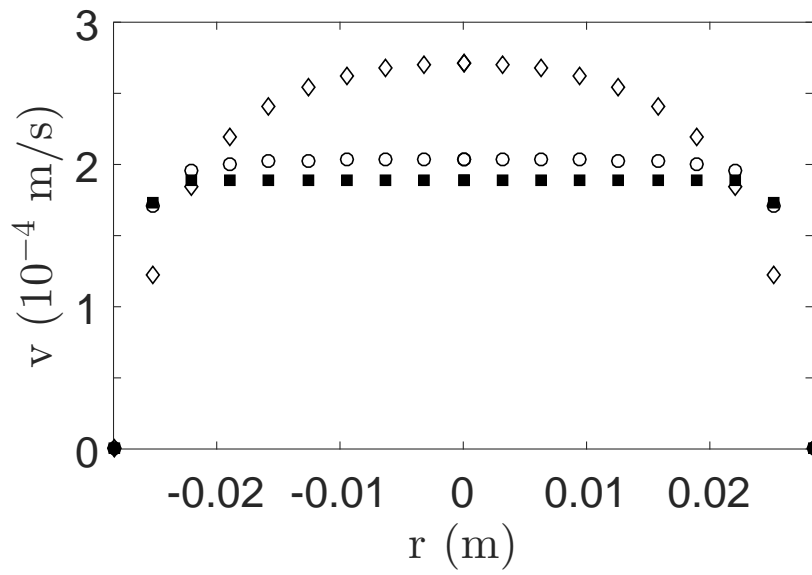


Figure 4.13: Simulated velocity profiles for a slow displacement. The symbols correspond to the times indicated in Fig. 4.12.

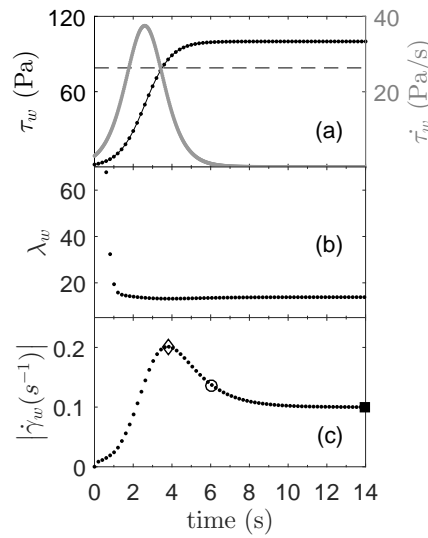


Figure 4.14: Results from a simulation of a fast displacement. (a) The imposed wall shear stress τ_w (black dots) and its time derivative $\dot{\tau}_w$ (grey dots) as a function of time. The dashed line is the yield stress. (b) $\lambda_w(t)$, the structure parameter at the wall of the pipe. (c) $|\dot{\gamma}_w|(t)$, the absolute value of the wall shear rate. The symbols indicate the times corresponding to the velocity profiles plotted in Fig. 4.15.

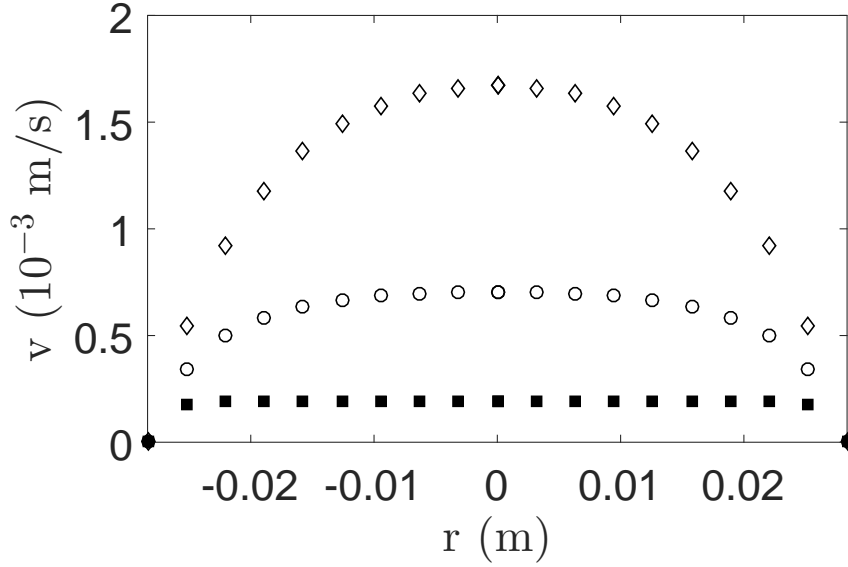


Figure 4.15: Simulated velocity profiles for a fast displacement. The symbols correspond to the times indicated in Fig. 4.14.

its derivative $\dot{\tau}_w$ is much larger than in the previous simulation, as shown in Fig. 4.14(a). Interestingly, λ_w decreases initially but then recovers slightly at long times (Fig. 4.14(b)). $|\dot{\gamma}_w|$ shows a clear peak before approaching its long-time value, consistent with the experimental results at high displacement rates (Fig. 4.6(c)). Velocity profiles for this simulation are shown in Fig. 4.15. The evolution of the velocity field is again similar to the experimental results (Fig. 4.7).

4.5 Discussion

Our experiments in the rough-walled pipe show that the yielding of Carbopol is a complex process involving several steps, and we observe a long transient before the flow field evolves to the steady-state plug flow predicted theoretically. The first stage is elastic deformation of the unyielded Carbopol, which results in the parabolic velocity profile measured at early times, as in Figs. 4.4 and 4.7. To understand this, note that the shear stress as a function of the radial coordinate r is $\tau(r) = \frac{\tau_w r}{R}$. For an elastic material governed by Hooke's law, $\tau = G_0 \gamma$,

where G_0 is the elastic modulus and γ is the strain. Combining these two expressions, we get $\gamma(r) = \frac{\tau_w r}{G_0 R} = \frac{\dot{\gamma}_w r}{R}$, where $\dot{\gamma}_w$ is the strain of a layer of Carbopol near the wall. Differentiation with respect to time gives $\dot{\gamma}(r) = \frac{\dot{\gamma}_w r}{R}$, and since $\dot{\gamma} = \frac{\partial v}{\partial r}$, integration with respect to r gives $v(r) = \frac{\dot{\gamma}_w r^2}{2R} + v(0)$, in agreement with the observed parabolic shape. Note that $\dot{\gamma}_w$ is negative in our experiments.

The next stage of yielding involves the development of slip at the wall of the pipe. No wall slip was observed until the wall shear stress exceeded a critical value τ_s , which was smaller than the yield stress. This behavior is in agreement with the description of slip in soft microgel materials in [45, 46]. Deformation of particles in contact with the walls leads to the formation of a lubrication layer and a sliding yield stress $\tau_s < \tau_y$, as observed in our experiments.

The development of wall slip is followed by yielding in a layer of fluid near the wall, as τ_w becomes greater than τ_y . As the wall stress is further raised beyond the yield stress, the thickness of the yielded layer also increases. The wall stress at the crossover time t^* determined from our pressure-time data corresponds well with the measured yield stress of the Carbopol, and so provides a good estimate of the actual yielding time of the material.

Finally, the wall stress approaches a plateau slightly larger than τ_y and the flow evolves to a steady state, with a velocity profile in reasonable agreement with the predictions of the HB model.

Our simulations based on the elasto-viscoplastic model of de Souza Mendes and Thompson [35] give very similar results. The simulations impose a no-slip boundary condition at the walls of the pipe, so do not show the wall-slip stage of the yielding process. The other stages of the simulated process are identical to those seen in the experiments, however: elastic deformation at early times, yielding near the wall, and a long transient that eventually evolves to a steady-state plug flow.

Our results agree with these of Divoux et al., who studied the fluidization of Carbopol in a Couette geometry [11, 13, 12]. They also observed a multi-stage yielding process, involving creeping deformation, wall slip, shear banding, and finally a homogeneous steady state [11].

The steady state flow is not homogeneous in our experiments, but includes an unyielded plug in the center of the pipe. This is due to the geometry of our experiments, for which $\dot{\gamma} = 0$ at the center of the pipe. Apart from this difference, the phenomenology of the yielding transition is identical. Divoux et al. showed that the duration of the yielding transition decreased as the applied shear rate or stress increased [11, 13, 12]. While we did not study this quantitatively, our results are again consistent with the previous work.

In the smooth-walled pipe, the wall shear stress never exceeds the yield stress. As a result, the Carbopol is not yielded and the flow observed at long times is entirely due to wall slip. As in the rough-walled pipe, we first observe elastic deformation, followed by the appearance of wall slip when the wall stress exceeds a threshold value τ_s . τ_s is smaller than that for the rough-walled pipe, consistent with previous work [12]. We also observe a stick-slip motion for the slowest flow, shown in Fig. 4.8(b) and (c), as observed in [12] and other experiments involving different polymer solutions [47, 48].

In the unyielded state, Carbopol is a soft, predominately elastic, solid, and our results demonstrate that elasticity plays a significant role in the yielding process. Indeed, the first stage of yielding involves elastic deformation, as described above. Another manifestation of elasticity is the peak in the wall shear rate that is observed in both experiments and simulations at higher flow rates (Figs. 4.6(c), 4.8(f), and 4.14(c)) but not at low flow rates (Figs. 4.5(b), 4.8(c), and 4.12(c)). The shear near the wall of the pipe will in general result from a combination of viscosity, in which case $\dot{\gamma}_w = \frac{\tau_w}{\eta}$, and elasticity, in which case $\dot{\gamma}_w = \frac{\dot{\tau}_w}{G_o}$. In our experiments with a higher flow rate, the wall stress initially increases quickly, leading to a high peak value of $\dot{\tau}_w$ (Fig. 4.14(a)). As a result, the elastic contribution to $\dot{\gamma}_w$ is larger than the viscous contribution, and the peak in $\dot{\tau}_w$ is reflected in the shear rate. At lower flow rates, $\dot{\tau}_w$ is much smaller (Fig. 4.12(a)), the viscous contribution to $\dot{\gamma}_w$ is more important, and no peak in $\dot{\gamma}_w$ is observed.

4.6 Conclusion

We studied the start-up flow and yielding of Carbopol in rough and smooth-walled vertical pipes. The Carbopol was displaced from below by an immiscible Newtonian fluid. The velocity field in the Carbopol was measured using PIV, and the wall shear stress was determined from measurements of the pressure in the Carbopol. The development of flow in the rough-walled pipe involved a long transient with several steps: elastic deformation, the onset of wall slip, yielding at the wall, and finally a steady-state plug flow that is well-described by the predictions of the Herschel-Bulkley model. In the smooth pipe, the wall shear stress never exceeded the yield stress. In this case, only the first two stages occurred: we observed elastic deformation followed by wall slip. These results are consistent with previous work on the yielding of Carbopol between concentric cylinders, allowing for the difference in geometry [11]. Simulations based on an elasto-viscoplastic model [35] show the same multi-step yielding process, in excellent agreement with our experiments. Our results indicate the importance of elasticity during the yielding process, first in the initial deformation stage, and later through the dominant contribution of elastic stress when the applied pressure increases rapidly.

4.7 Appendix

The equations of the elasto-viscoplastic model of de Souza Mendes and Thompson are [35]

$$\theta_1 = \left(1 - \frac{\eta_\infty}{\eta_v(\lambda)}\right) \frac{\eta_v(\lambda)}{G_s(\lambda)}; \theta_2 = \left(1 - \frac{\eta_\infty}{\eta_v(\lambda)}\right) \frac{\eta_\infty}{G_s(\lambda)} \quad (\text{A1})$$

$$\dot{\gamma} + \theta_2 \ddot{\gamma} = \frac{\theta_2}{\eta_\infty} \left(\frac{\tau}{\theta_1} + \dot{\tau} \right) \quad (\text{A2})$$

$$G_s(\lambda) = G_o e^{m\left(\frac{1}{\lambda} - \frac{1}{\lambda_0}\right)} \quad (\text{A3})$$

$$\eta_v(\lambda) = \eta_\infty e^\lambda \quad (\text{A4})$$

$$\lambda_{eq}(\tau) = \ln\left(\frac{\eta_{eq}(\tau)}{\eta_\infty}\right) \quad (\text{A5})$$

$$\frac{d\lambda}{dt} = \frac{1}{t_{eq}} \left[\left(\frac{1}{\lambda} - \frac{1}{\lambda_0}\right)^a - \left(\frac{\lambda}{\lambda_{eq}(\tau)}\right)^b \left(\frac{1}{\lambda_{eq}(\tau)} - \frac{1}{\lambda_0}\right)^a \right] \quad (\text{A6})$$

$$\eta_{eq}(\dot{\gamma}) = \frac{\tau_y}{\dot{\gamma}} + K\dot{\gamma}^{n-1} + \eta_\infty \quad (\text{A7})$$

Here θ_1 and θ_2 are the relaxation time and retardation time, respectively. $\eta_v(\lambda)$ and $G_s(\lambda)$ are the viscous and elastic moduli, both of which are functions of the structure parameter λ . η_∞ is the viscosity at infinite shear rate, corresponding to the fully unstructured state. τ , $\dot{\gamma}$, $\dot{\tau}$, $\dot{\gamma}$ are the shear stress, shear rate, and their derivatives with respect to time. G_o is the elastic modulus in the fully structured state, and m is a dimensionless number. λ_0 is the structure parameter in the fully structured state. λ_{eq} and η_{eq} are the structure parameter and viscosity in the equilibrium state, in which $\frac{d\lambda}{dt} = 0$, corresponding to the state probed with the rheometer. t_{eq} is the characteristic time for λ to approach equilibrium. It is 0 for a non-thixotropic fluid. a and b are dimensionless constants. τ_y is the yield stress, and n and K are the flow index and consistency from the HB model.

The simulations for 0.5 wt% Carbopol presented in this article were calculated using $\eta_\infty = 1.002 \times 10^{-3}$ Pa s, the viscosity of water at room temperature, $G_o = 450$ Pa as measured with the rheometer using small-amplitude oscillatory shear. $\lambda_0 = \infty$, as Carbopol is a yield-stress fluid, and $t_{eq} = 1 \times 10^{-3}$ s, because Carbopol is weakly thixotropic [8]. Following [35], we set $m = a = b = 1$. $\tau_y = 78.9$ Pa, $n = 0.324$, and $K = 44.4$ Pa s ^{n} for 0.5 wt% Carbopol as in Table 4.1.

The Carbopol is subjected to a wall shear stress $\tau_w(t) = A(1 + B \exp(-Ct))^{-1}$, mimicking

the functional form of τ_w in the experiments. A is the value τ_w reaches at long times, slightly larger than the yield stress (Fig. 4.3), B is a constant, and C controls the rate at which τ_w reaches the plateau. We used a cylindrical geometry with grid points equally spaced radially at $r_i = \frac{iR}{10}$ ($i = 1, 2, \dots, 10$). $R=2.837$ cm is the radius of the pipe. The shear stress at each radial grid point is: $\tau_{r_i} = \tau_w r_i / R$. τ_{r_i} and $\dot{\tau}_{r_i}$ are thus known at each point. Eqs. (A2) and (A6) are two coupled differential equations for λ and $\dot{\gamma}$, supplemented by Eqs. (A1), (A3), (A4), (A5), and (A7). This system of equations was solved numerically using Matlab's ODE45 function [49]. The initial conditions were chosen to be $\dot{\gamma}_{r_i}(t_0 = 0) = 10^{-4} \text{ s}^{-1}$ and $\lambda_{r_i}(t_0 = 0) = 700$, representing a highly structured state that is almost stationary [35].

To model slow displacement, we used $A = 100$ Pa, slightly larger than the yield stress of the Carbopol, $B = 50$, and $C = 0.2 \text{ s}^{-1}$. For simulation of a faster displacement, we set $C = 1.5 \text{ s}^{-1}$.

Bibliography

- [1] T. J. Bromwich. An application of Heaviside's methods of viscous fluid motion. *Journal of the London Mathematical Society*, 1:10–13, 1930.
- [2] G. Szymanski. Quelques solutions exactes des équations d'hydrodynamique du fluide visqueux dans le cas d'un tube cylindrique. *Journal de Mathématiques Pures et Appliquées*, 11:67–108, 1932.
- [3] W. E. Langlois and M. O. Deville. *Slow Viscous Flow, 2nd edition*. Springer, 2014.
- [4] R. Berker, S. A. Schaaf, A. E. Scheidegger, J. Weissinger, S. Corrsin, and C. Lin. *Handbuch der Physik*. Springer, 1963.
- [5] P. Coussot. Yield stress fluid flows: A review of experimental data. *Journal of Non-Newtonian Fluid Mechanics*, 211:31–49, 2014.
- [6] T. C. Davenport and R. S. H. Somper. The yield value and breakdown of crude oil gels. *Journal of the Institute of Petroleum*, 57:86–105, 1971.
- [7] H. P. Rønningsen. Rheological behaviour of gelled, waxy north sea crude oils. *Journal of Petroleum Science and Engineering*, 7:177–213, 1992.
- [8] P. C. F. Møller, J. Mewis, and D. Bonn. Yield stress and thixotropy: on the difficulty of measuring yield stresses in practice. *Soft Matter*, 2:274–283, 2006.
- [9] A. M. V. Putz and T. I. Burghelea. The solid–fluid transition in a yield stress shear thinning physical gel. *Rheologica Acta*, 48:673–689, 2009.
- [10] T. Divoux, D. Tamarii, C. Barentin, and S. Manneville. Transient shear banding in a simple yield stress fluid. *Physical Review Letters*, 104:208301, 2010.

- [11] T. Divoux, C. Barentin, and S. Manneville. From stress-induced fluidization processes to Herschel-Bulkley behaviour in simple yield stress fluids. *Soft Matter*, 7:8409–8418, 2011.
- [12] T. Divoux, C. Barentin, and S. Manneville. Stress overshoot in a simple yield stress fluid: An extensive study combining rheology and velocimetry. *Soft Matter*, 7:9335–9349, 2011.
- [13] T. Divoux, D. Tamarii, C. Barentin, S. Teitel, and S. Manneville. Yielding dynamics of a Herschel–Bulkley fluid: A critical-like fluidization behaviour. *Soft Matter*, 8:4151–4164, 2012.
- [14] C. Chang, D. V. Boger, and Q. D. Nguyen. The yielding of waxy crude oils. *Industrial and Engineering Chemistry Research*, 37:1551–1559, 1998.
- [15] C. Chang, Q. D. Nguyen, and H. P. Rønningsen. Isothermal start-up of pipeline transporting waxy crude oil. *Journal of Non-Newtonian Fluid Mechanics*, 87:127–154, 1999.
- [16] A. G. Sierra, P. R. Vargas, and S. S. Ribeiro. Startup flow of elasto-viscoplastic thixotropic materials in pipes. *Journal of Petroleum Science and Engineering*, 147:427–434, 2016.
- [17] F. H. Marchesini, A. A. Alicke, P. R. de Souza Mendes, and C. M. Ziglio. Rheological characterization of waxy crude oils: Sample preparation. *Energy & Fuels*, 26:2566–2577, 2012.
- [18] H. Teng and J. J. Zhang. Modeling the thixotropic behavior of waxy crude. *Industrial and Engineering Chemistry Research*, 52:8079–8089, 2013.
- [19] R. F. G. Visintin, R. Lapasin, E. Vignati, P. D’Antona, and T. P. Lockhart. Rheological behavior and structural interpretation of waxy crude oil gels. *Langmuir*, 21:6240–6249, 2005.

- [20] R. Mendes, G. Vinay, G. Ovarlez, and P. Coussot. Modeling the rheological behavior of waxy crude oils as a function of flow and temperature history. *Journal of Rheology*, 59:703–732, 2015.
- [21] I. Daprà and G. Scarpi. Start-up flow of a Bingham fluid in a pipe. *Meccanica*, 40:49–63, 2005.
- [22] M. R. Davidson, Q. D. Nguyen, C. Chang, and H. P. Rønningesen. A model for restart of a pipeline with compressible gelled waxy crude oil. *Journal of Non-Newtonian Fluid Mechanics*, 123:269–280, 2004.
- [23] G. Vinay, A. Wachs, and J-F. Agassant. Numerical simulation of weakly compressible Bingham flows: the restart of pipeline flows of waxy crude oils. *Journal of Non-Newtonian Fluid Mechanics*, 136:93–105, 2006.
- [24] I. Frigaard, G. Vinay, and A. Wachs. Compressible displacement of waxy crude oils in long pipeline startup flows. *Journal of Non-Newtonian Fluid Mechanics*, 147:45–64, 2007.
- [25] G. Vinay, A. Wachs, and I. Frigaard. Start-up transients and efficient computation of isothermal waxy crude oil flows. *Journal of Non-Newtonian Fluid Mechanics*, 143:141–156, 2007.
- [26] A. Wachs, G. Vinay, and I. Frigaard. A 1.5 D numerical model for the start up of weakly compressible flow of a viscoplastic and thixotropic fluid in pipelines. *Journal of Non-Newtonian Fluid Mechanics*, 159:81–94, 2009.
- [27] G. M. de Oliveira, L. L. V. da Rocha, A. T. Franco, and C. O. R. Negrão. Numerical simulation of the start-up of Bingham fluid flows in pipelines. *Journal of Non-Newtonian Fluid Mechanics*, 165:1114–1128, 2010.

- [28] C. O. R. Negrão, A. T. Franco, and L. L. V. Rocha. A weakly compressible flow model for the restart of thixotropic drilling fluids. *Journal of Non-Newtonian Fluid Mechanics*, 166:1369–1381, 2011.
- [29] P. R. de Souza Mendes, F. S-M. de Abreu Soares, C. M. Ziglio, and M. Gonçalves. Startup flow of gelled crudes in pipelines. *Journal of Non-Newtonian Fluid Mechanics*, 179:23–31, 2012.
- [30] H. S. Lee. *Computational and Rheological Study of Wax Deposition and Gelation in Subsea Pipelines*. PhD thesis, The University of Michigan, 2008.
- [31] C. J. Dimitriou, G. H. McKinley, and R. Venkatesan. Rheo-piv analysis of the yielding and flow of model waxy crude oils. *Energy & Fuels*, 25:3040–3052, 2011.
- [32] A. Poumaere, M. Moyers-González, C. Castelain, and T. Burghelea. Unsteady laminar flows of a Carbopol gel in the presence of wall slip. *Journal of Non-Newtonian Fluid Mechanics*, 205:28–40, 2014.
- [33] J. Mewis and N. J. Wagner. Thixotropy. *Advances in Colloid and Interface Science*, 147:214–227, 2009.
- [34] P. R. de Souza Mendes. Thixotropic elasto-viscoplastic model for structured fluids. *Soft Matter*, 7:2471–2483, 2011.
- [35] P. R. de Souza Mendes and R. L. Thompson. A unified approach to model elasto-viscoplastic thixotropic yield-stress materials and apparent yield-stress fluids. *Rheologica Acta*, 52:673–694, 2013.
- [36] S. J. Curran, R. E. Hayes, A. Afacan, M. C. Williams, and P. A. Tanguy. Properties of Carbopol solutions as models for yield-stress fluids. *Journal of Food Science*, 67:176–180, 2002.

- [37] G. Ovarlez, S. Cohen-Addad, K. Krishan, J. Goyon, and P. Coussot. On the existence of a simple yield stress fluid behavior. *Journal of Non-Newtonian Fluid Mechanics*, 193:68–79, 2013.
- [38] P. C. F. Møller, A. Fall, V. Chikkadi, D. Derks, and D. Bonn. An attempt to categorize yield stress fluid behaviour. *Philosophical Transactions of the Royal Society of London A: Mathematical, Physical and Engineering Sciences*, 367:5139–5155, 2009.
- [39] F. K. Oppong and J. R. de Bruyn. Diffusion of microscopic tracer particles in a yield-stress fluid. *Journal of Non-Newtonian Fluid Mechanics*, 142:104–111, 2007.
- [40] J. M. Piau. Carbopol gels: Elastoviscoplastic and slippery glasses made of individual swollen sponges: Meso-and macroscopic properties, constitutive equations and scaling laws. *Journal of Non-Newtonian Fluid Mechanics*, 144:1–29, 2007.
- [41] H. Tabuteau, P. Coussot, and J. R. de Bruyn. Drag force on a sphere in steady motion through a yield-stress fluid. *Journal of Rheology*, 51:125–137, 2007.
- [42] K. Sveen. An introduction to matpiv v. 1.6.1. <http://www.mn.uio.no/math/english/people/aca/jks/matpiv/>, 2004.
- [43] Y. Damianou, M. Philippou, G. Kaoullas, and G. C. Georgiou. Cessation of viscoplastic poiseuille flow with wall slip. *Journal of Non-Newtonian Fluid Mechanics*, 203:24–37, 2014.
- [44] P. E. Boukany, P. Tapadia, and S-Q. Wang. Interfacial stick-slip transition in simple shear of entangled melts. *Journal of Rheology*, 50:641–654, 2006.
- [45] S. P. Meeker, R. T. Bonnecaze, and M. Cloitre. Slip and flow in pastes of soft particles: Direct observation and rheology. *Journal of Rheology*, 48:1295–1320, 2004.
- [46] J. R. Seth, M. Cloitre, and R. T. Bonnecaze. Influence of short-range forces on wall-slip in microgel pastes. *Journal of Rheology*, 52:1241–1268, 2008.

- [47] P. P. Drda and S-Q. Wang. Stick-slip transition at polymer melt/solid interfaces. *Physical Review Letters*, 75:2698, 1995.
- [48] S-Q. Wang and P. A. Drda. Stick- slip transition in capillary flow of polyethylene. 2. molecular weight dependence and low-temperature anomaly. *Macromolecules*, 29:4115–4119, 1996.
- [49] D. J. Higham and N. J. Higham. *MATLAB guide*. SIAM, 2005.

Chapter 5

Confinement effects on the rheology of Carbopol

5.1 Introduction

Complex fluids have interesting and useful behavior that is intermediate between that of conventional liquids and solids. This is a result of their microstructure, which is typically on the scale of a few microns. Examples include colloidal suspensions consisting of a solvent and small particles, emulsions in which droplets of one phase are suspended in another, and polymer solutions with a microstructure formed by interacting polymer chains. Recently, the effects of confinement on the flow of colloidal suspensions [1], concentrated emulsions [2, 3], granular materials [4], and polymer gels [5] have been studied. When complex fluids are confined to a small region with a length scale comparable to the characteristic scale of their microstructure, their flow behavior deviates from that predicted by the rheology measured on the bulk scale. In such cases, the material cannot be treated as a continuum in the confinement direction, and the details of the microstructure become important. Confinement can also be important in practical applications such as coating, which involve flows that significantly confine the fluid.

Carbopol is a model yield-stress fluid. Its microstructure is seen as a network of expanded

polymer blobs [6, 7] which give the material a yield stress when jammed [7]. The size of the individual Carbopol particles has been measured using confocal microscopy, and found to be a few microns [8] or a few 10s of microns [5]. Lee et al. measured a length scale in excess of $50 \mu\text{m}$ using light scattering [6], possibly due to aggregates of interacting microgel particles [9, 5]. Several recent experiments have studied the effect of confinement on the flow behavior of Carbopol. Jofore et al. measured the flow curve of Carbopol in a microgap rheometer with gap ranging from 5 to $100 \mu\text{m}$ [5]. For gaps roughly the size of their microgel particles, with rough boundary conditions, the yield stress was found to be larger than its bulk value. A similar increase in yield stress with confinement was found in experiments using a squeeze flow rheometer [10]. Davies et al. measured the viscosity of Carbopol using a plate-plate geometry at different gaps [11]. Clasen et al. used a microgap rheometer to measure the flow curve of a skin cream consisting of microcrystalline wax particles with a size of around $50 \mu\text{m}$ [3]. For gaps smaller than $55 \mu\text{m}$, they did not detect a yield stress and wall slip became important.

Other microfluidic devices have also been used as the confining geometry. Goyon et al. studied the flow of a concentrated emulsion in large-aspect-ratio microfluidic channels with confinement in one direction [12, 2]. They demonstrated that the Herschel-Bulkley model, which described the bulk flow well, did not predict the flow field in the confined geometry. They developed a non-local fluidity model involving a cooperativity length scale over which the dynamics of the fluid were correlated, and successfully fitted their experimental data using this model. Similarly, Géraud et al. measured the flow of Carbopol confined to a two-dimensional microfluidic device [13, 8]. They also found a disagreement between the results of their experiments and the behavior predicted from the rheology at the bulk scale and interpreted their results in terms of the non-local fluidity model. The non-local fluidity model states that the dynamics in fluid is spatially correlated and the material may be yielded at stresses smaller than the bulk yield stress. This correlation is negligible in large geometries but becomes important in small geometries. These experiments indicate that when the container becomes small enough, the rheology becomes dependent on the size of the container.

Wall slip becomes important when flow is confined. Jofore et al. observed that for Carbopol at lower concentrations with smooth boundary conditions, the slip velocity increased when the separation between the plates of their microgap rheometer decreased below of a single particle [5]. Similar results were obtained by Clasen et al. using a skin cream [3]. For higher Carbopol concentrations, however, the slip velocity decreased when decreasing the gap [5].

In this chapter, approximately square microfluidic channels with different dimensions were used to study the flow of Carbopol confined in two dimensions. We measured the flow fields of Carbopol using Micro-PIV (Particle Image Velocimetry). We compared the experimentally measured flow fields with those predicted by the HB model, based on the rheology measured on bulk samples. For microchannels with widths greater than $300\ \mu\text{m}$, the velocity profiles show a plug at the center of the channel and agree well with the predictions of the HB model. For smaller microchannels, however, we observe strong disagreement between the experiments and the predictions based on the bulk rheology. In these small channels, a plug flow is not observed and the measured velocity profiles cannot be described using a model that has a yield stress. This shows that confinement dramatically modifies the rheology of Carbopol.

5.2 Experiment

5.2.1 Fabrication of microchannels

Approximately square polydimethylsiloxane (PDMS) microchannels were fabricated as described in [14]. PDMS gel (Sylgard 184) was mixed with a cross-linker (Dow Corning) in a 10:1 ratio, then degassed in a vacuum chamber. The microchannels were made in two parts. The top part, which included the volume of the channel along with inlet and outlet reservoirs, was made by casting PDMS onto a positive mold machined from Plexiglas with a CNC mill, shown in Fig. 5.1(a). Each mold incorporated three independent straight microchannels. After curing for 48 hours at room temperature, the top PDMS layer was peeled off the mold. Polyethylene tubes with an inner diameter of 0.58 mm and an outer diameter of 0.965 mm

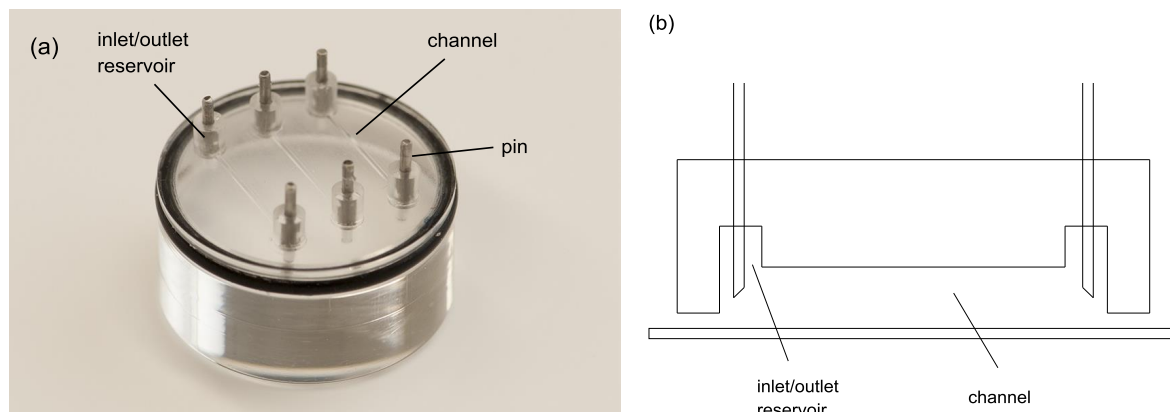


Figure 5.1: (a) The Plexiglas mold used to form the microchannels. The diameter of the mold is 1.7 cm. (b) The PDMS cast using the mold shown in (a) is bonded to the bottom plate, and polyethylene tubes are inserted into the inlet and outlet reservoirs to form the full microchannel assembly.

(Becton-Dickinson) were inserted into holes formed by pins in the mold, as shown in Fig. 5.1(a), and bonded with epoxy (Lepage Speed Set Professional Epoxy). The bottom of the channels was made by spin coating approximately $200 \mu\text{l}$ PDMS on the 3 cm diameter glass bottom of a cell culture dish (MatTek) for 60 s at 500 RPM followed by 300 s at 3000 RPM using a spin coater (MBraun MB-SC-ADV). The coated culture dish was placed in a beaker containing 300 ml water and partially cured for 150 seconds in a microwave oven (Master Chef) with a power of 900 W. The molded PDMS top piece was lightly pressed onto the partially cured bottom PDMS layer as shown in Fig. 5.1(b). The assembly was placed in the water bath again, and cured in the microwave oven for 5 minutes to irreversibly bond the top and bottom together. The top of the mold was polished. Therefore, the top of the PDMS microchannels was quite smooth, with a roughness estimated from scanning electron micrographs of approximately $0.5 \mu\text{m}$. The sides of the mode were not polished, and as a result the sides of the PDMS microchannels had a roughness of approximately $5 \mu\text{m}$.

Table 5.1: Dimensions of the microchannels

channel number	1	2	3	4	5
mold width (μm)	500 ± 30	300 ± 30	200 ± 10	100 ± 6	50 ± 5
channel width (μm)	451 ± 30	322 ± 30	134 ± 10	87 ± 6	54 ± 5
channel height (μm)	539 ± 30	249 ± 30	169 ± 10	65 ± 6	32 ± 5
channel length (cm)	1.00 ± 0.05	1.00 ± 0.05	1.00 ± 0.05	1.00 ± 0.05	1.00 ± 0.05

Microchannels with five different nominal sizes, ranging from 500 down to 50 μm in width, were used in our experiments. These are labeled as channels 1 through 5, as in Table 5.1. All channels were 1 cm in length. The actual dimensions of the channels were slightly different from those of the positive mold, and were determined from measurements made with a microscope (Olympus 1X71) with a 20 \times objective lens at three positions along the length of the channels. They are shown in Table 5.1. Fig. 5.2 shows an image of the cross-section of the top PDMS layer of Channel 4, which had a height of 65 μm and a width of 87 μm . Although the Plexiglas molds were accurately square in cross-section, the resulting channels were not, as can be seen in Fig. 5.2. This is presumably due to shrinkage of the PDMS on curing, and was taken into account in our simulations and data analysis.

5.2.2 Fluid preparation and bulk rheology

Experiments were performed using three fluids. MilliQ water with a viscosity of 0.001 Pa s at 20 $^{\circ}\text{C}$ was used in preliminary experiments to verify the performance and geometry of the microchannels. A saline solution of 3.4 wt% hydroxyethyl cellulose (HEC), a homogeneous polymer solution, was used to study the behavior of a complex fluid with a structural length scale much smaller than the dimensions of the microchannels. Finally, we studied the effect of confinement on the flow of a 0.14 wt% solution of Carbopol 940 (Lubrizol).

The HEC solution was prepared by first dissolving 0.466 g NaCl (Sigma-Aldrich S9888) in 300 ml distilled water, followed by mixing with a magnetic stirrer for 3 minutes. 10.5 g HEC powder (Sigma-Aldrich 09368) was slowly added to the solution, which was then stirred for three hours at room temperature.

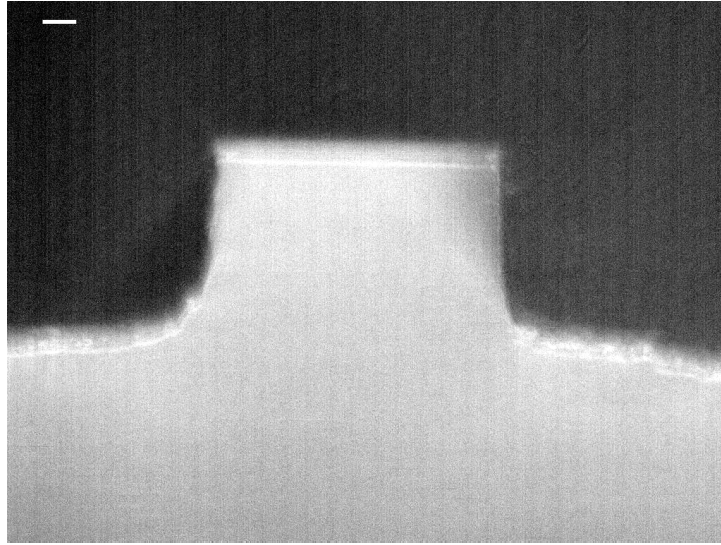


Figure 5.2: A micrograph of the cross-section of the top PDMS piece of Channel 4. The scale bar is $10\ \mu\text{m}$ in length.

Carbopol consists of polydisperse particles of cross-linked polyacrylic acid [15]. The particles are small (approximately $1\ \mu\text{m}$ in diameter) when dry, but expand to several microns in size in a neutralized solution [6, 8]. Jamming of these swollen polymer blobs results in Carbopol displaying yield-stress behavior [6, 16, 17]. The Carbopol solution was prepared by adding the required amount of Carbopol powder to deionized water and stirring with a magnetic stirrer until it was completely dissolved and the solution was homogeneous. When initially dissolved in water, Carbopol has a $p\text{H} \approx 3$. NaOH with a concentration of $40\ \text{mg/ml}$ was added to raise its $p\text{H}$ to 6, resulting in swelling of the microgel particles.

Fluorescent polymer microspheres (Duke Scientific) were added to all three fluids studied, with an approximate solid volume fraction of 0.0015% . $1\ \mu\text{m}$ diameter particles were used for experiments in Channels 1 and 2, $0.49\ \mu\text{m}$ diameter particles for Channels 3 and 4, and $0.21\ \mu\text{m}$ diameter particles for Channel 5.

An Anton Paar MCR302 rheometer was used to measure the rheological properties of the Carbopol and HEC solutions seeded with tracer particles. The measuring geometry was a cone-

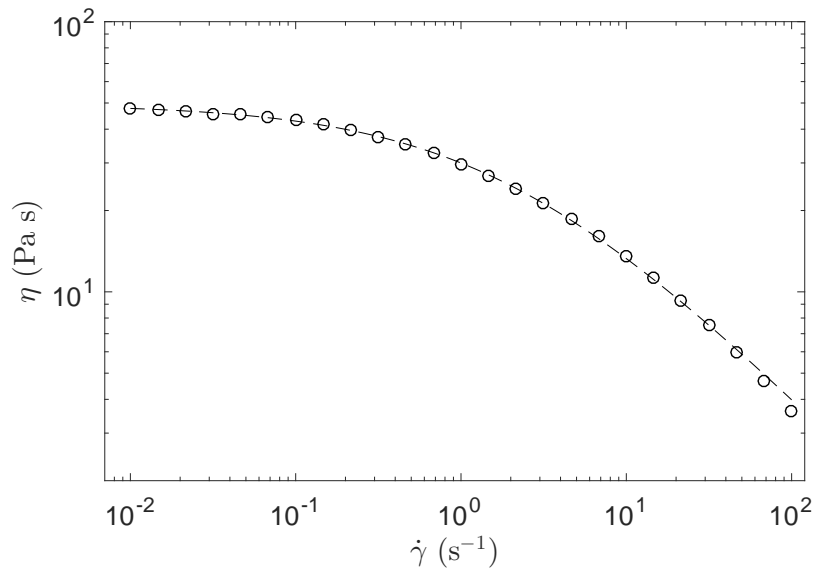


Figure 5.3: The viscosity as a function of shear rate for a 3.4 wt% HEC solution seeded with tracer particles. The dashed line is a fit of the Cross model to the data.

and-plate with a 50 mm diameter and 4° cone angle. Sandpaper with a roughness of $50\ \mu\text{m}$ was affixed to the rheometer tool to minimize wall slip. An environmental housing with an atmosphere saturated with water vapor surrounded the tool to minimize evaporation over the duration of the measurements. Fig. 5.3 shows the viscosity η as a function of shear rate $\dot{\gamma}$ for the 3.4 wt% HEC solution, with tracer particles, at a temperature of $20.00 \pm 0.01\ ^\circ\text{C}$, obtained by decreasing the shear rate in steps from $100\ \text{s}^{-1}$ to $0.001\ \text{s}^{-1}$. The waiting time at each shear rate varies from 2 seconds at the highest rate to 2 minutes at the lowest. The HEC solution is shear thinning, but has no yield stress, and its viscosity approaches a Newtonian plateau at low shear rates. The data are well described by a fit to the Cross model, $\eta = \eta_0 / \left(1 + \left(\frac{\dot{\gamma}}{\dot{\gamma}_0}\right)^{1-n}\right)$, where η_0 is the zero-shear-rate viscosity, $\dot{\gamma}_0$ is the characteristic shear rate at which the fluid changes from Newtonian to power-law behavior, and n is a power-law index. The fit gives $\eta_0 = 49.5 \pm 0.2\ \text{Pa}\cdot\text{s}$, $\dot{\gamma}_0 = 1.99 \pm 0.04\ \text{s}^{-1}$, and $n = 0.378 \pm 0.005$.

The flow curve of the 0.14 wt% Carbopol solution was measured as a function of shear rate using the same protocol as for the HEC measurements. The results are plotted in Fig. 5.4.

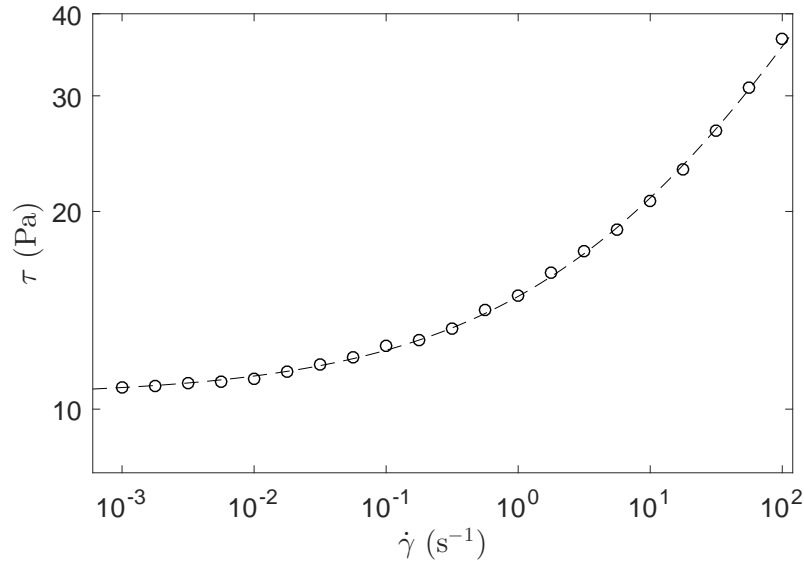


Figure 5.4: The shear stress as a function of shear rate for a 0.14 wt% Carbopol 940 solution seeded with tracer particles. The dashed line is a fit of the Herschel-Bulkley model to the data.

The data approach a finite yield stress at low shear rates, and are well described the Herschel-Bulkley (HB) model, $\tau = \tau_0 + k\dot{\gamma}^m$, where τ_0 is the yield stress, k is the consistency, and m is the power index. The fit gives $\tau_0=10.5\pm 0.2$ Pa, $k=4.4\pm 0.2$, and $m=0.38\pm 0.01$.

5.2.3 Micro-particle image velocimetry

Micro-PIV (Particle Image Velocimetry) was used to measure the velocity fields of the fluids flowing in the microchannels. A schematic diagram of the experiment is shown in Fig. 5.5. The fluid was pumped into the channel from a 1 ml syringe through a length of polyethylene tubing by a syringe pump (NEWERA NE-300) at flow rates ranging from 0.3 to 290 $\mu\text{l/hr}$. The fluorescent particles were illuminated in the green with an X-Cite 120Q light source and imaged in the red. They were visualized using a high-speed camera (Metek Vision Research Phantom VEO 340L) connected to the microscope, at frame rates ranging from 60 to 500 frames per second. A 10 \times objective lens was used for experiments with Channel 1, 20 \times with Channels 3 and 4, and 40 \times with Channel 5, to ensure that the width of the microchannel occu-

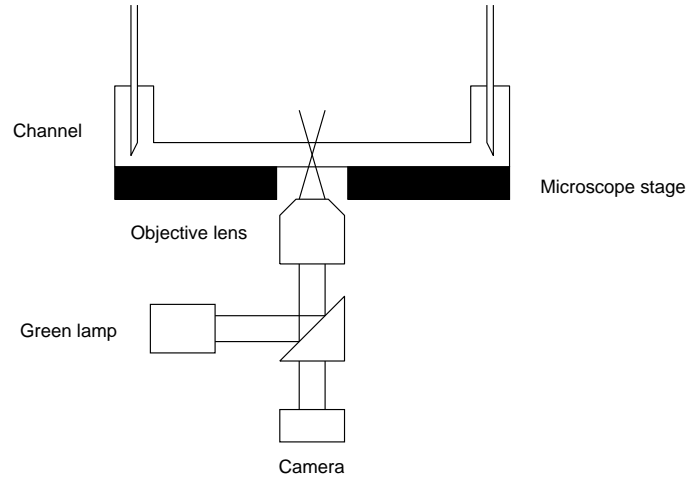


Figure 5.5: A schematic diagram of the experimental setup. The fluid was pumped into the microchannel at a constant rate from a syringe driven by a syringe pump. A camera connected to the microscope imaged the motion of fluorescent tracer particles suspended in the fluid.

pies at least 50% of the image. The spatial resolution of the images ranged from $3.7 \text{ pixels}/\mu\text{m}$ with the $40\times$ objective to $0.5 \text{ pixels}/\mu\text{m}$ for the $10\times$ objective. We measured velocity profiles at several heights, which we varied by adjusting the fine focus on the microscope. The profiles presented below were measured in the mid-plane. Two-dimensional velocity fields were calculated from the recorded images using the MatPIV software package [18].

5.2.4 Computational fluid dynamics

Ansys Fluent software was used to simulate the velocity fields of the fluids for the same geometries and mean flow rates as in the experiments [19]. For simulations of water and HEC, the cross section of the channel was meshed uniformly by squares, with 15 nodes across the channel width. Since the velocity fields calculated for Carbopol show a plug in the middle of

the channel, we used the inflation function in the meshing step of Fluent to produce a finer mesh near the walls than in the central region for that fluid. In this case, the meshing elements have irregular shapes. We used a density of $0.9982 \text{ g}\cdot\text{ml}^{-1}$ for all three fluids. For water, we used a constant viscosity of $0.001003 \text{ Pa}\cdot\text{s}$. For simulations of Carbopol and HEC, we used the rheological parameters measured above. In all cases, the boundary conditions for the computations consisted of a uniform inlet velocity, chosen to give the same volumetric flow rate (corrected for wall slip, as discussed below) as in the experiments, zero gauge pressure at the outlet and no slip at the walls. The inlet velocity v_{in} used in the simulations was calculated as

$$v_{in} = \frac{Q_{in}}{A} = \frac{Q_{sp} - v_{as}A}{A}, \quad (5.1)$$

where Q_{in} is the inlet flow rate used in the simulations, Q_{sp} is the experimental flow rate controlled by the syringe pump, and A is the cross-sectional area of the channel. v_{as} is the average slip velocity determined from the experiments, given by $v_{as} = \frac{\int_0^H v_s(h)dh}{H}$, where H is the height of the channel and $v_s(h)$ is the slip velocity at vertical position h , determined from the measured velocity profiles. The numerical calculation was pressure-based and steady. A steady state solution was obtained when the difference in the velocity values in three directions between iterations was smaller than $1 \times 10^{-15} \text{ m/s}$.

5.3 Results

5.3.1 Water

The velocity field of water flowing through the microchannels was measured to confirm the performance of the experimental system with a simple, Newtonian fluid, and to validate the Fluent computations. Fig. 5.6 shows velocity profiles determined from PIV measurements at the mid-height of the largest and smallest microchannels, Channels 1 and 5. The velocities

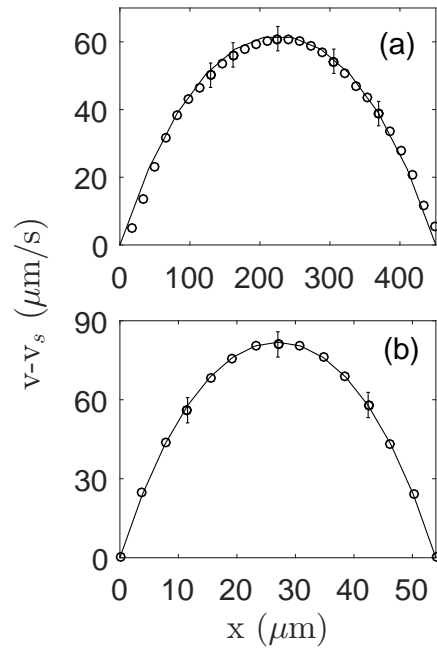


Figure 5.6: The velocity profiles in water at the mid-plane of Channels 1 and 5. The velocities have been corrected for the slip velocity measured at the channel walls. x is the horizontal position along the width of the channel. Circles: experimental measurements. Lines: simulations. (a) Channel 1, $Q_{in} = 23$ $\mu\text{l/hr}$. (b) Channel 5, $Q_{in} = 0.4$ $\mu\text{l/hr}$.

have been corrected for the slip velocity measured at the channel walls. The viscosity of water is known, and the dimensions of the channels and the inlet velocity are measured or derived from experimental measurements, respectively, so the simulations involve no free parameters. Q_{in} was 23 $\mu\text{l/hr}$ for Channel 1 and 0.4 $\mu\text{l/hr}$ for Channel 5. In both cases, the velocity profiles are parabolic in shape and are identical to the Fluent predictions. The agreement between experiment and simulation is also excellent for the other channels and for all flow rates studied. This confirms that our microchannels and experimental system perform as expected with a simple Newtonian fluid, for which no confinement effects are expected in channels of this size [20].

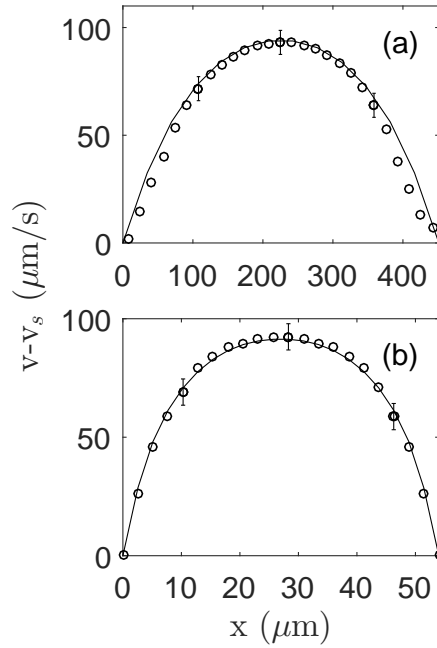


Figure 5.7: The velocity profiles in the HEC solution at the mid-plane of Channels 1 and 5. The velocities have been corrected for the slip velocity measured at the channel walls. Circles: experimental measurements. Lines: simulations. (a) Channel 1, $Q_{in} = 42 \mu\text{l/hr}$. (b) Channel 5, $Q_{in} = 0.4 \mu\text{l/hr}$.

5.3.2 HEC

We measured the velocity profiles in the HEC solution at the mid-plane of Channels 1 and 5. The results are shown in Fig. 5.7, along with the results of the Fluent simulations. As above, there were no free parameters in the simulations. The inlet flow rate Q_{in} was $42 \mu\text{l/hr}$ for Channel 1 and $0.4 \mu\text{l/hr}$ for Channel 5. Because HEC is shear thinning and the viscosity is higher in the middle where the shear rate is lower, the measured velocity profiles are flatter than parabolic in both channels, as Fig. 5.7 shows. This effect is more pronounced in the smaller channel, Fig. 5.7(b). The experimental results overlap with the simulations based on the bulk rheology, indicating that the rheology of the HEC solution does not change when the size of the flow geometry is decreased to the $50 \mu\text{m}$ scale. The fact that we observe no confinement effects on this homogeneous polymer solution in these experiments is not surprising, since the characteristic length scale of the microstructure (i.e., the radius of gyration of the polymer) is several hundred nanometers, substantially smaller than the dimensions of our channels [21].

5.3.3 Carbopol

Fig. 5.8(a) shows velocity profiles measured in Carbopol in the largest microchannel, Channel 1, for inlet flow rates of 55 and 70 $\mu\text{l/hr}$. Simulated profiles are also shown. The rheology of the Carbopol was calculated using the HB model with parameter values as measured above. As in the simulations for water and HEC, there were no free parameters. As seen in Fig. 5.8(a), the velocity profiles show a plug in the center of the channel. Within the plug, the Carbopol is unyielded, since the shear stress is smaller than the yield stress. The simulations agree very well with the measured velocity profiles, indicating that the bulk rheology provides an excellent description of the flow of Carbopol in this channel. The same level of agreement between the experiments and the simulations is also found for Channel 2 (data not shown).

In smaller channels, however, the measured velocity profiles differ from those predicted based on the bulk rheological properties. Results for Channel 3 are shown in Fig. 5.8(b). The measured velocity profiles still have a flat, plug-like region in the center of the channel. In this case, however, simulations based on the bulk rheology differ dramatically from the experimental results. As seen in Fig. 5.8(b), the measured plug-like region is much narrower, and has a significantly higher velocity than predicted by the simulations.

We attempted to obtain a better match between the measured and simulated velocity profiles by varying the parameters τ_0 , n , and k in the Herschel-Bulkley simulations and fitting the results to the data by eye. We were unable to describe the experimental data adequately for any choice of parameters involving a non-zero yield stress. Rather, we found that the data could be described by a power-law model with no yield stress, i.e., $\tau = k\dot{\gamma}^n$. The shape of the simulated profile was insensitive to the value of k , which was therefore fixed at the value found from fits of the bulk rheological data to the HB model. The power-law index n was then varied to produce a reasonable fit to the data. Results are shown as dashed lines in Fig. 5.8(b) and describe the data well. The fitting parameters are summarized in Table 5.2. Similar results are obtained in smaller channels. In Channel 3, the value of n determined from fits of the power law model to the data appears to be independent of flow rate. As the channels become

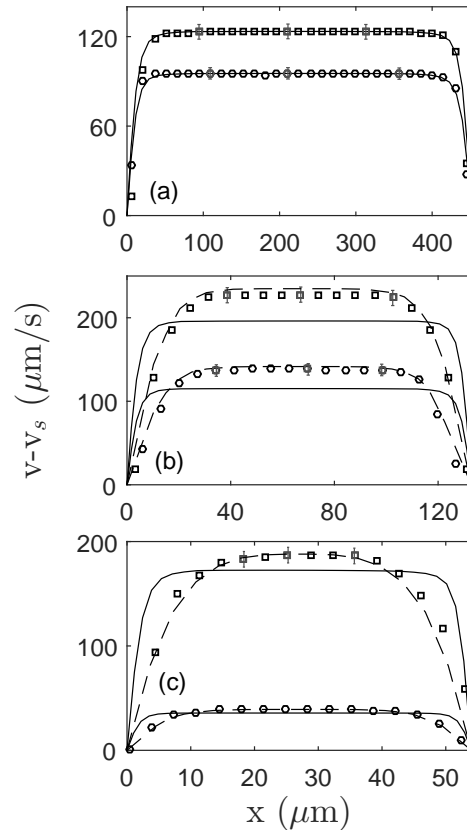


Figure 5.8: The velocity profiles in Carbopol at the mid-plane of Channels 1, 3, 5. The velocities have been corrected for the slip velocity measured at the channel walls. Symbols: experimental measurements. Solid lines: simulations using the HB model with the measured yield stress. Dashed lines: fits of the data to a power-law model, with zero yield stress. (a) Channel 1. Circles: $Q_{in} = 55 \mu\text{l/hr}$. Squares: $Q_{in} = 70 \mu\text{l/hr}$. (b) Channel 3. Circles: $Q_{in} = 6 \mu\text{l/hr}$. Squares: $Q_{in} = 10 \mu\text{l/hr}$. (c) Channel 5. Circles: $Q_{in} = 0.3 \mu\text{l/hr}$; for this data set the uncertainty in $v - v_s$ is approximately the size of the symbols. Squares: $Q_{in} = 1.4 \mu\text{l/hr}$.

Table 5.2: Parameters of the power-law model used to fit velocity profiles in the smaller channels.

channel number	3		4		5	
flow rate ($\mu\text{l/hr}$)	6.0 ± 0.1	10.0 ± 0.1	5.0 ± 0.1	7.0 ± 0.1	0.3 ± 0.1	1.4 ± 0.1
n	0.30 ± 0.01	0.32 ± 0.01	0.51 ± 0.01	0.70 ± 0.001	0.32 ± 0.01	0.42 ± 0.01
k (Pa s^n)	4.4	4.4	4.4	4.4	4.4	4.4

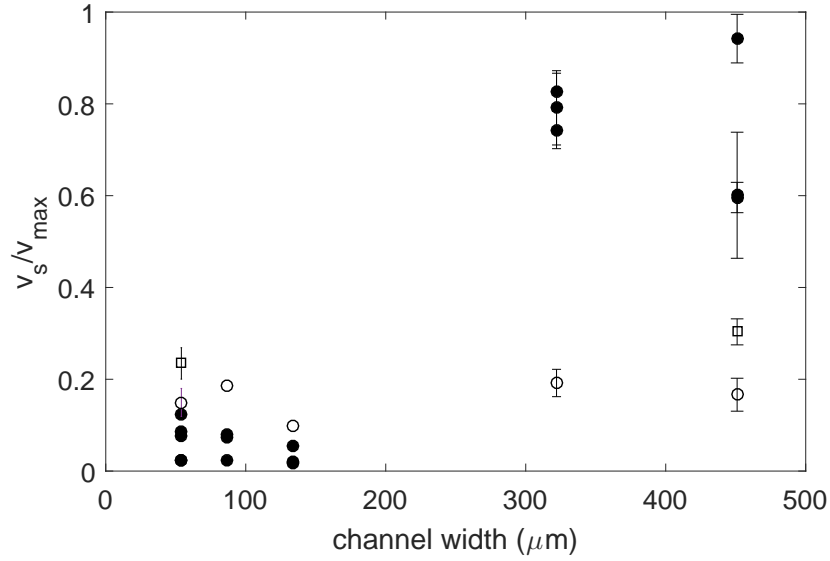


Figure 5.9: v_s/v_{max} , the ratio of the slip velocity to the maximum velocity at the mid-plane of the channel plotted as a function of the width of the channel. Filled circles: Carbopol. Unfilled circles: water. Unfilled squares: HEC. The uncertainties for the data without errorbars shown are approximately the size of the symbols.

smaller, however, n increases as the flow rate increases, as seen in Table 5.2. Velocity profiles in Channel 5, the smallest channel studied, are shown in Fig. 5.8(c). In this case, plug-like region in the center of the channel is even smaller, and the measured and fitted velocity profiles show distinct curvature in the center of the channel.

Fig. 5.9 shows v_s/v_{max} , the ratio of the slip velocity to the maximum velocity at the mid-plane of the channel. For water and HEC, v_s/v_{max} did not change significantly when the size of the channel decreased. For Carbopol, in contrast, v_s/v_{max} was significantly higher in the two larger channels, for which the velocity profiles showed no confinement effects, than in the

smaller channels in which confinement effects were observed. It is interesting that this change appears to take place rather suddenly as the channel size is decreased.

5.4 Discussion and conclusion

We studied the flow of water, HEC and Carbopol solutions in approximately square microchannels with different dimensions. The flow behaviour of water and HEC did not change as the channel got smaller. No confinement effects were observed for these fluids because they are homogeneous on the length scale of the channels used in our experiments.

The flow behavior of Carbopol, however, depends on the dimensions of the channels. In the two largest channels, no effects of confinement were observed and the measured velocity profiles agreed well with predictions based on the bulk-scale rheology of Carbopol. In channels smaller than $150\ \mu\text{m}$ in size, however, the measured velocity profiles deviated substantially from the bulk-scale predictions and could not be fitted by a model with a yield stress. Our results thus indicate that the yield stress of Carbopol vanishes when it is confined in two dimensions on a scale of approximately $150\ \mu\text{m}$ or smaller.

Previous work has studied the confined flow of emulsions [12, 2] and Carbopol solutions [13, 8] in wider systems, i.e., in large-aspect-ratio microfluidic channels with confinement in only one direction. Goyon et al. measured the velocity profiles in an emulsion containing oil droplets with a size of $6\ \mu\text{m}$. They fitted their measured velocity profiles to the HB model, and found that the yield stress decreased in smooth channels with widths of $112\ \mu\text{m}$ and smaller, but increased in rough channels as the channel width was decreased below $250\ \mu\text{m}$ [12, 2]. Géraud et al. studied Carbopol in a two-dimensional microchannel with a width of $116\ \mu\text{m}$ [13, 8]. They observed that the width of the plug region in their measured velocity profiles was narrower than predicted based on the bulk-scale rheology, in agreement with our observations. Jofore et al. measured the flow curve of Carbopol using a microgap rheometer, and found that the yield stress increased for gaps $100\ \mu\text{m}$ and smaller with rough boundary conditions [5].

Similarly, Yan et al. observed an increase in Carbopol's yield stress for gaps smaller than $250 \mu\text{m}$ with rough boundary conditions [10].

In general, we would expect confinement effects to become noticeable when the dimensions of the measuring geometry become comparable to the characteristic size scale of the microstructure. The size of individual Carbopol particles was measured to be on the order of two to four microns [8], roughly a factor of 40 smaller than the size of the largest channel in which we observe significant confinement effects. On the other hand, Jofore et al. measured swollen particle sizes of up to $40 \mu\text{m}$ [5], while Lee et al. found a length scale larger than $50 \mu\text{m}$ [6]. These larger scales, which may be characteristic of aggregates of several particles [5] rather than individual particles, are roughly a factor of three smaller than Channel 3. This suggests that the material rheology, and in particular the yield stress, is determined by structure on the larger measured length scales, rather than on the scale of a single particle.

Goyon et al. used a nonlocal fluidity model to explain the effects of confinement on the rheology of the emulsions studied in their experiments [12, 2]. Analysis of their data in terms of this model gave a cooperativity length ξ of $20 \mu\text{m}$, indicating correlations in the local dynamics on a scale of several times the size of a single emulsion droplet. Géraud et al. analysed their data on the confined flow of Carbopol using the same nonlocal fluidity model and found $\xi \sim 13 \mu\text{m}$, again a few times larger than the size of a single microgel particle [13, 8]. This cooperativity length is roughly a factor of 10 smaller than the scale at which confinement effects become significant on our experiments and so is also consistent with our results. We were unable to apply the same model to our data because of mathematical difficulties related to the square cross-section of our channels, and because we did not measure the shear stress in our experiments.

Clasen et al. [3] and Jofore et al. [5] emphasized the importance of wall slip in confined flows. Jofore et al. observed that with smooth boundary conditions for Carbopol at a higher concentration the slip velocity decreased when the separation between two parallel plates of the microgap rheometer decreased below the single particle size [5]. Both Jofore et al. and Clasen

et al. observed that the critical shear stress at the transition from wall slip to yielding increased as the gap decreased. Clasen et al. explained this phenomenon by compression and trapping of particles under strong confinement, leading to a frictional interaction that gave a higher resistance to slip [3]. We also observed wall slip in our measured velocity profiles, although to facilitate comparison with the numerical simulations we have subtracted the slip velocity from the velocity fields presented in Fig. 5.8. We found that for water and HEC, v_s/v_{max} , the ratio of the slip velocity to the maximum velocity, did not change significantly when the size of the channel decreased. Similarly, their rheological properties did not change in smaller channels. For Carbopol, however, v_s/v_{max} was significantly smaller in the smaller channels in which the effects of confinement on the rheology were observed, and this change appeared to occur quite suddenly as a function of channel size. This suggests that the confinement simultaneously affects not only the rheology of Carbopol, but also the slip on the walls. Our slip velocities were measured at the sides of the microchannels, which had a roughness of approximately $5 \mu\text{m}$. This is fairly smooth on the scale of the $50 \mu\text{m}$ objects, but rough on the scale of the individual microgel particles.

Our results show that the rheological properties and wall slip of our Carbopol solution are substantially modified when it is confined in two dimensions and flowing in the third. In particular, we observe that, under sufficient confinement, the yield stress of our Carbopol vanishes and the material behaves as a power-law fluid. This phenomenon may be due to spatial correlations in the dynamics, as suggested by the nonlocal fluidity model of [12, 2, 13, 8]. It may also be due to a straightforward reorganization of the microstructure imposed by the confinement. The yield stress in bulk Carbopol results from three-dimensional jamming of highly swollen, entangled microgel particles [16] or aggregates of entangled particles [5]. Let us posit that the relevant jammed structural elements are the $50 \mu\text{m}$ -scale objects measured by [5] and [6]. When confined to a region just a few times this size, the structure of a jammed three-dimensional network of these objects will be substantially modified. Specifically, we would expect the structural elements to form a quasi-one-dimensional arrangement along the

length of the channel. Such an arrangement would lack the constraints of the bulk network and, in particular, is likely to flow much more easily in response to an imposed shear stress.

In conclusion, we have studied the flow under confinement of Carbopol 940, a yield-stress fluid. In channels with sides larger than $300\ \mu\text{m}$, the measured velocity fields agreed well with predictions based on the bulk rheology. For channels smaller than $150\ \mu\text{m}$, however, confinement significantly modified the fluid rheology. We found that the velocity field could be described assuming a power-law rheology, with no yield stress. We suggest that rearrangement of the jammed microgel network due to confinement causes the yield stress to vanish.

It would be useful to directly visualize the microstructure of the Carbopol under confinement, perhaps using microscopic techniques developed in [8, 5, 17], in an effort to better understand its relationship to the observed changes in rheology. It would also be very interesting to establish a direct relationship between the microstructure and the cooperativity length discussed in [12, 2, 13, 8]. It also would be useful to measure the shear stress in our microchannel experiments, i.e., by measuring the pressure drop across the length of the microfluidic channel. This would enable more detailed analysis of our data in terms of the fluidity model of [12, 2, 13, 8], and extraction of the flow curve from the velocity field data. Finally, since Carbopol particles are known to be quite polydisperse, it would be interesting to explore similar phenomena in more well characterized microgel systems, such as PNIPAM [22].

Bibliography

- [1] R. Besseling, L. Isa, P. Ballesta, G. Petekidis, M. E. Cates, and W. C. K. Poon. Shear banding and flow-concentration coupling in colloidal glasses. *Physical Review Letters*, 105:268301, 2010.
- [2] J. Goyon, A. Colin, and L. Bocquet. How does a soft glassy material flow: finite size effects, non local rheology, and flow cooperativity. *Soft Matter*, 6:2668–2678, 2010.
- [3] C. Clasen and G. H. McKinley. Gap-dependent microrheometry of complex liquids. *Journal of Non-Newtonian Fluid Mechanics*, 124:1–10, 2004.
- [4] K. Kamrin and G. Koval. Nonlocal constitutive relation for steady granular flow. *Physical Review Letters*, 108:178301, 2012.
- [5] B. D. Jofore, P. Erni, G. Vleminckx, P. Moldenaers, and C. Clasen. Rheology of microgels in single particle confinement. *Rheologica Acta*, 54:581–600, 2015.
- [6] D. Lee, I. A. Gutowski, A. E. Bailey, L. Rubatat, J. R. de Bruyn, and B. J. Frisken. Investigating the microstructure of a yield-stress fluid by light scattering. *Physical Review E*, 83:031401, 2011.
- [7] J. Y. Kim, J. Y. Song, E. J. Lee, and S. K. Park. Rheological properties and microstructures of Carbopol gel network system. *Colloid and Polymer Science*, 281:614–623, 2003.
- [8] B. Géraud, L. Jørgensen, C. Ybert, H. Delanoë-Ayari, and C. Barentin. Structural and cooperative length scales in polymer gels. *European Physical Journal E–Soft Matter*, 40:5, 2017.
- [9] G. P. Roberts and H. A. Barnes. New measurements of the flow-curves for Carbopol dispersions without slip artefacts. *Rheologica Acta*, 40:499–503, 2001.

- [10] Y. Yan, Z. Zhang, D. Cheneler, J. R. Stokes, and M. J. Adams. The influence of flow confinement on the rheological properties of complex fluids. *Rheologica Acta*, 49:255–266, 2010.
- [11] G. A. Davies and J. R. Stokes. Thin film and high shear rheology of multiphase complex fluids. *Journal of Non-Newtonian Fluid Mechanics*, 148:73–87, 2008.
- [12] J. Goyon, A. Colin, G. Ovarlez, A. Ajdari, and L. Bocquet. Spatial cooperativity in soft glassy flows. *Nature*, 454:84, 2008.
- [13] B. Géraud, L. Bocquet, and C. Barentin. Confined flows of a polymer microgel. *European Physical Journal E–Soft Matter*, 36:30, 2013.
- [14] D. Lorusso, H. N. Nikolov, J. S. Milner, N. M. Ochotny, S. M. Sims, S. J. Dixon, and D. W. Holdsworth. Practical fabrication of microfluidic platforms for live-cell microscopy. *Biomedical Microdevices*, 18:78, 2016.
- [15] Lubrizol. <http://www.lubrizol.com/personalcare/products/carbopol/981.html>, 2013.
- [16] F. K. Oppong and J. R. de Bruyn. Microrheology and jamming in a yield-stress fluid. *Rheologica Acta*, 50:317–326, 2011.
- [17] I. A. Gutowski, D. Lee, J. R. de Bruyn, and B. J. Frisken. Scaling and mesostructure of Carbopol dispersions. *Rheologica Acta*, 51:441–450, 2012.
- [18] K. Sveen. An introduction to matpiv v. 1.6.1. <http://www.mn.uio.no/math/english/people/aca/jks/matpiv/>, 2004.
- [19] FLUENT Manual. Ansys fluent 12.0 users guide. <http://users.ugent.be/~mvbelleg/flug-12-0.pdf/>, 2012.
- [20] U. Raviv, P. Laurat, and J. Klein. Fluidity of water confined to subnanometre films. *Nature*, 413:51, 2001.

- [21] F. K. Oppong. *Rheology, microrheology and structure of soft materials*. PhD thesis, The University of Western Ontario, 2009.
- [22] B. H. Tan, R. H. Pelton, and K. C. Tam. Microstructure and rheological properties of thermo-responsive poly (n-isopropylacrylamide) microgels. *Polymer*, 51:3238–3243, 2010.

Chapter 6

General Discussion and Conclusions

In the three experiments reported in this thesis, we used not only rotational shear rheometry but also particle image velocimetry (PIV) to study the rheological properties of complex fluids. Rotational shear rheometry measures the bulk rheology of fluids, but cannot probe the internal motion of the fluids in detail. PIV can capture the instantaneous velocity field in the fluid to provide more details of the fluid dynamics. In PIV, particles are seeded in the fluid. The method assumes that the particles are passive, neutrally buoyant, and do not affect the flow and that the motion of the particles accurately follows the fluid flow. In the experiments on tissue phantom materials described in Chap. 3, we used PIV to observe convective flow in a HEC solution subjected to a temperature gradient and calculated the contribution of this flow to the total heat transfer. In Chap. 4, we studied the yielding process in Carbopol using spatio-temporal velocity profiles obtained by PIV. In the work in Chap. 5, we used micro-PIV to visualize the velocity field in Carbopol flowing through microchannels. The advantages of PIV are that it captures the flow in the whole field; it can be used to measure flow on a range of time and size scales; it is conceptually simple, relatively inexpensive, and accurate. However, PIV also has some drawbacks: the fluid has to be seeded with tracer particles, which may change the rheological properties of the fluid; different particles can be illuminated differently, giving them different intensities in the recorded images; two cameras are needed for

three-dimensional velocimetry, which increases the cost; and it cannot be used for fluids that are not transparent [1]. Other methods have also been used to determine the velocity field in complex fluids. Ultrasonic speckle velocimetry (USV) was used to obtain velocity profiles in [2, 3]. USV is based on the interaction between a high-frequency ultrasonic pulse and particles seeded in the fluids [4]. Successive ultrasonic pulses are sent into the fluid, the particles scatter the pulses, and the backscattered pressure signal is recorded as a function of time. The received signals reflect the spatial distribution of scatterers along the acoustic beam [2]. Velocity profiles can be determined from this spatio-temporal signal. USV can capture velocity profiles in non-transparent fluids. The technique still requires the fluid to be seeded with particles to scatter the ultrasound pulses, however, potentially changing the rheological properties of the fluid. As used in [2, 3], it is also limited to the two-dimensional case. Magnetic resonance velocimetry (MRV) is also used to obtain velocity profiles in fluids. This technique is based on detecting the nuclear magnetic resonance (NMR) of hydrogen and can be carried out in conventional MRI systems used for clinical imaging [5]. MRV does not require the fluid to be seeded with particles and does not require optical access or transparency, can be used in complex geometries, and has no limitations with regard to the three-dimensional case. MRV has been used to measure velocity fields in polymer materials, including polymer melts and solutions [6]. MRV also has drawbacks, however. In most cases, it is limited to measurements of steady flows. Time resolved measurements are possible but difficult. An example of time-resolved MRV is described in [7]. It is also much more expensive and technically difficult to use than other velocimetry techniques.

This thesis has described three experiments on different aspects of the dynamics of complex fluids. This work provides us with a better understanding of the relation between the flow behavior and the thermal properties, the transient fluid mechanics involved when a complex fluid goes from rest to fully developed steady-state flow, and changes in fluid behaviour that result when a complex fluid is confined to small geometries with sizes comparable to the length scale of the fluid's microstructure. This work also has implications for the use of complex

fluids in applications. The work described in Chap. 3 has provided a better understanding of the properties and behaviour of the polymer materials used as tissue phantoms in testing the behavior of medical devices in MRI systems [8]. The results of Chap. 4 are relevant to the fluid mechanics involved in the activation of transport of waxy crude oil in pipelines [9], and our work on confinement may be applicable to the interesting flow behavior of blood in capillary vessels in which red blood cells are strongly confined [10].

We investigated the rheological and thermal properties of a HEC solution that is commonly used as a tissue phantom for testing the behaviour of medical devices in MRI system. We performed experiments and simulations which mimicked the heating conditions that can occur in MRI device tests. We observed convective flow in the HEC solution which contributed roughly the same to the heat transport as thermal conduction. Our results suggest that tests of medical devices in MRI systems using HEC as a tissue phantom may underestimate the increase of the local temperature that would occur in real tissue, and that the effects of convective heat transport must be accounted for in modeling and analyzing such tests. It would be interesting to examine the behavior of other polymer materials that are used as tissue phantoms in MR device testing, such as saline solutions of polyacrylic acid (PAA) [11, 12, 13]. It would also be worth examining materials with a yield stress, including Carbopol, which was used as a tissue phantom in MRI systems in [14]. Because Carbopol has a yield stress, there will be a threshold for the onset of flow in a horizontal temperature gradient, in contrast to the situation for HEC. This may make Carbopol more suitable as a tissue phantom than other materials.

The startup flow of Carbopol in a pipe was investigated. In the experiments, Carbopol was displaced from below by a Newtonian liquid injected from the bottom of the pipe. Both rough and smooth boundary conditions were studied. In the rough-walled pipe, the yielding of Carbopol involved several steps: elastic deformation, the onset of wall slip, yielding at the wall, and finally a steady-state plug flow that is well-described by the predictions of the HB model. In contrast, in the smooth-walled pipe, the wall shear stress never exceeded the yield stress, and the motion of Carbopol was due only to wall slip. We also demonstrated the impor-

tance of elasticity during the yielding process, particularly for faster displacement rates. The experimentally observed behaviour was successfully predicted numerically using an elastoviscoplastic model [15]. This study was motivated by the startup of waxy crude oil in pipes. Our work helps us better understand the transient fluid mechanics in this startup process, in particular the elastic deformation that takes place at early times and the transient flow behavior at intermediate times. In future studies, it would be interesting to replace the simple yield-stress fluid, Carbopol, with a thixotropic yield-stress fluid, for example, a Laponite clay suspension, to better mimic the rheology of waxy crude oil. Laponite is transparent, so its flow can be visualized using PIV. Thixotropy causes a time and flow–history dependence of the yield stress, viscosity and elastic modulus, so the aging of the Laponite will affect the start-up behaviour. It would also be interesting to study the startup flow of Carbopol confined to microchannels, to investigate how confinement changes the startup process.

We studied the flow of Carbopol confined to square microchannels with sides ranging from 500 down to 50 μm . We demonstrated that for the channels with sides 150 μm or smaller Carbopol did not have a yield stress. This might be related to spatial correlations in the dynamics [16, 17], or to modification of the three-dimensional jammed microgel network due to confinement. The fact that we observe confinement effects in channels as large as 150 μm suggests that the yield stress in Carbopol is determined by microstructural elements roughly 50 μm in size [18]. These objects, which may be aggregates of individual microgel particles, are significantly larger than the size of a single microgel particle. Previous work has studied the flow of Carbopol confined to large-aspect-ratio microfluidic channels with confinement in only one direction [19, 20]. These workers analysed their data using a nonlocal fluidity model and found a cooperativity length on the order of 13 μm , on which the fluid dynamics is spatially correlated, leading to fluidization at stresses smaller than the bulk yield stress. In our work, we used square microchannels with confinement in two dimensions, and observed that the yield stress vanished. In a future study, it would be worthwhile to study the flow of Carbopol in circular cross-section microchannels, the fabrication of which has been reported in [21]. That

geometry would make the analysis using the nonlocal fluidity model accessible. It would be interesting to compare the cooperativity length scale determined in the circular cross-section channels with confinement in all directions to that in large-aspect-ratio rectangular channels with confinement in only one direction.

Bibliography

- [1] M. Raffel, C. E. Willert, S. Wereley, and J. Kompenhans. *Particle image velocimetry: a practical guide*. Springer, 2013.
- [2] S. Manneville, L. Bécu, and A. Colin. High-frequency ultrasonic speckle velocimetry in sheared complex fluids. *European Physical Journal-Applied Physics*, 28:361–373, 2004.
- [3] T. Divoux, D. Tamarii, C. Barentin, S. Teitel, and S. Manneville. Yielding dynamics of a Herschel–Bulkley fluid: A critical-like fluidization behaviour. *Soft Matter*, 8:4151–4164, 2012.
- [4] L. Sandrin, S. Manneville, and M. Fink. Ultrafast two-dimensional ultrasonic speckle velocimetry: A tool in flow imaging. *Applied Physics Letters*, 78:1155–1157, 2001.
- [5] C. J. Elkins and M. T. Alley. Magnetic resonance velocimetry: applications of magnetic resonance imaging in the measurement of fluid motion. *Experiments in Fluids*, 43:823–858, 2007.
- [6] P. T. Callaghan. Rheo-NMR: nuclear magnetic resonance and the rheology of complex fluids. *Reports on Progress in Physics*, 62:599, 1999.
- [7] A. B. Tayler, M. Benning, A. J. Sederman, D. J. Holland, and L. F. Gladden. Ultrafast magnetic-resonance-imaging velocimetry of liquid-liquid systems: Overcoming chemical-shift artifacts using compressed sensing. *Physical Review E*, 89:063009, 2014.
- [8] G. Hartsgrove, A. Kraszewski, and A. Surowiec. Simulated biological materials for electromagnetic radiation absorption studies. *Bioelectromagnetics*, 8:29–36, 1987.
- [9] H. P. Rønningsen. Rheological behaviour of gelled, waxy north sea crude oils. *Journal of Petroleum Science and Engineering*, 7:177–213, 1992.
- [10] D. A. Fedosov, M. Peltomäki, and G. Gompper. Deformation and dynamics of red blood cells in flow through cylindrical microchannels. *Soft Matter*, 10:4258–4267, 2014.

- [11] A. R. Rezai, D. Finelli, J. A. Nyenhuis, G. Hrdlicka, J. Tkach, A. Sharan, P. Ruggieri, P. H. Stypulkowski, and F. G. Shellock. Neurostimulation systems for deep brain stimulation: in vitro evaluation of magnetic resonance imaging–related heating at 1.5 Tesla. *Journal of Magnetic Resonance Imaging*, 15:241–250, 2002.
- [12] S. M. Park, J. A. Nyenhuis, C. D. Smith, E. J. Lim, K. S. Foster, K. B. Baker, G. Hrdlicka, A. R. Rezai, P. Ruggieri, and A. Sharan. Gelled versus nongelled phantom material for measurement of MRI-induced temperature increases with bioimplants. *IEEE Transactions on Magnetics*, 39:3367–3371, 2003.
- [13] K. R. Gorny, M. F. Presti, S. J. Goerss, S. C. Hwang, D-P. Jang, I. Kim, H-K. Min, Y. Shu, C. P. Favazza, and K. H. Lee. Measurements of RF heating during 3.0-T MRI of a pig implanted with deep brain stimulator. *Magnetic Resonance Imaging*, 31:783–788, 2013.
- [14] A. Hellerbach, V. Schuster, A. Jansen, and J. Sommer. MRI phantoms—are there alternatives to agar? *Plos One*, 8:0070343, 2013.
- [15] P. R. de Souza Mendes and R. L. Thompson. A unified approach to model elastoviscoplastic thixotropic yield-stress materials and apparent yield-stress fluids. *Rheologica Acta*, 52:673–694, 2013.
- [16] J. Goyon, A. Colin, G. Ovarlez, A. Ajdari, and L. Bocquet. Spatial cooperativity in soft glassy flows. *Nature*, 454:84, 2008.
- [17] J. Goyon, A. Colin, and L. Bocquet. How does a soft glassy material flow: finite size effects, non local rheology, and flow cooperativity. *Soft Matter*, 6:2668–2678, 2010.
- [18] D. Lee, I. A. Gutowski, A. E. Bailey, L. Rubatat, J. R. de Bruyn, and B. J. Frisken. Investigating the microstructure of a yield-stress fluid by light scattering. *Physical Review E*, 83:031401, 2011.

- [19] B. Géraud, L. Bocquet, and C. Barentin. Confined flows of a polymer microgel. *European Physical Journal E–Soft Matter*, 36:30, 2013.
- [20] B. Géraud, L. Jørgensen, C. Ybert, H. Delanoë-Ayari, and C. Barentin. Structural and cooperative length scales in polymer gels. *European Physical Journal E–Soft Matter*, 40:5, 2017.
- [21] L. K. Fiddes, N. Raz, S. Sriganapalan, E. Tumarkan, C. A. Simmons, A. R. Wheeler, and E. Kumacheva. A circular cross-section pdms microfluidics system for replication of cardiovascular flow conditions. *Biomaterials*, 31:3459–3464, 2010.

Curriculum Vitae

Name: Yang Liu

Post-Secondary Education and Degrees: Hubei University
Wuhan, Hubei, China
2008 - 2012 B.Sc.

University of Western Ontario
London, ON
2012 - 2017 Ph.D.

Honours and Awards: Western Graduate Research Scholarship 2012–2017
Western Graduate Teaching and Research Assistanship 2012–2017

Related Work Experience: Teaching Assistant
Department of Physics and Astronomy
The University of Western Ontario
2012–2017

Conference presentations Yang Liu, John R. de Bruyn,
Yielding transition of Carbopol gel in a vertical pipe,
American Physical Society Division of Fluid Dynamics, Portland,
Oregon, US, 20-22 November, 2016.

John R. de Bruyn, Yang Liu,
Start-up flow in a model yield-stress fluid,
CAP Congress, Kingston, Ontario, Canada, May 29-June 2, 2017.

John R. de Bruyn, Yang Liu, Daniel Lorusso, David Holdworth,
and Tamie L. Poepping,
Confinement effects on the rheology of Carbopol in microchannels,
Viscoplastic Fluids: From Theory to Applications,
Rotorua, New Zealand, Oct 30-Nov 3, 2017.

Publications:

Y. Liu, C. C. Hopkins, W. B. Handler, B. A. Chronik, J. R. de Bruyn, Rheology and heat transport properties of a hydroxyethyl cellulose-based MRI tissue phantom. *Biomedical Physics & Engineering Express*, 3:045008, 2016.

Y. Liu, J. R. de Bruyn, Start-up flow of a yield-stress fluid in a vertical pipe. *Journal of Non-Newtonian Fluid Mechanics*, Submitted in Sep 2017.